Systematic Optimization Technique for MESFET Modeling

Yaser A. Khalaf

Dissertation submitted to the Faculty of the
Virginia Polytechnic Institute and State University
in partial fulfillment of the requirements for the degree of

Doctor of Philosophy

in

Electrical Engineering

Approved:

____
Sedki. M. Riad, Chairman

____
Ioannis M. Besieris

____
Wayne A. Scales

____
Samir M. El-Ghazaly

____
Aicha A. Elshabini

July 2000
Blacksburg, Virginia

Systematic Optimization Technique for MESFET Modeling

by

Yaser A. Khalaf

Chairman: Dr. Sedki. M. Riad

Time Domain & RF Measurement Laboratory

The Bradley Department of Electrical and Computer Engineering

(Abstract)

Accurate small and large-signal models of *metal-semiconductor field effect transistor* (MESFET) devices are essential in all modern microwave and millimeter wave applications. Those models are used for robust designs and fabrication development. The sophistication of modern communication systems urged the need of *monolithic microwave integrated circuits* (MMICs), which consists of many MESFETs on the same chip. As the chip density increases, the need of accurate MESFET models becomes more pronounced.

In this study, a new technique has been developed to extract a 15-element small signal model of MESFET devices. This technique implies the use of three sets of S-parameter measurements at different bias conditions. The technique consists of two major steps; in the first step, some of the bias-independent extrinsic parameters are estimated in preparation for the second step. In the second step, all other parameters should be extracted at the bias point of interest. This technique shows reliable results. Unlike other optimization techniques, our proposed technique shows insensitivity to the unavoidable measurement errors over any frequency range. It shows a unique solution for all parameter values. This technique has been tested on S-parameters of a hypothetical-device model and compared with other optimization-based extraction techniques. Moreover, it has been also applied to GaAsTEK 0.8x300 μm^2 MESFETs to extract the

model parameters at different bias voltages. The study reveals accurate and consistent results among the similar devices on the same wafer.

Some thermal characteristics of the small-signal parameters are discussed. The parameters are extracted from measurements at three temperatures for two similar devices on the same wafer. The thermal results of the two devices demonstrate consistent results, which assure the preciseness, and robustness of our proposed technique.

In addition, the relation between the small-signal model parameters and the large-signal model parameters is also presented. The parameters of an empirical model for the drain-source current are extracted from the dc measurements along with the small-signal transconductance and output conductance. The large-signal model results for a GaAsTEK 0.8x300 μm^2 MESFET are introduced.

Acknowledgment

All praise is due to our God (ALLAH) who has been bestowing me with his great bounties and enabled me to complete my dissertation.

I would like to thank Dr. Sedki M. Riad for his support, guidance and invaluable advices. I would like to offer my gratitude to the members of my advisory committee, Dr. Ioannis M. Besieris, Dr. Wayne A. Scales, Dr. Samir M. El-Ghazaly, and Dr. Aicha A. Elshabini, for their help and comments.

I appreciate GaAsTEK, ITT industries, especially Dr. Thomas A. Winslow for supplying me with all the measurements in this dissertation.

My deep gratitude is due to my parents for their continuous guidance, encouragement, support, and prayers during my life. I would like also to extend my gratitude to my brothers for their help and cooperation. Thanks are due to my wife for her patience, help, and being away from her family for several years during my study.

Finally, I would like to thank my friends, and colleagues who presented me an advice or assistance during my work.

Contents

Abstract i

Acknowledgement iii

Contents iv

List of Figures vii

List of Tables ix

1 Introduction 1

1.1 Why GaAs MESFET Modeling 3

1.2 Dissertation Organization 7

2 MESFET Physics and Modeling 17

2.1 Physical Structure 8

2.2 Principles of the GaAs MESFET Operation 10

2.3 MESFET Models 13

2.3.1 Parasitic Inductances 15

2.3.2 Parasitic Resistances 16

2.3.3 Pad Capacitances 16

2.3.4 Intrinsic Capacitances 17

2.3.5 Charging Resistance R_i 19

2.3.6 Transconductance 20

2.3.7 Transit Time 20

2.3.8 Output Resistance 21

2.4 Literature Review 22

3 Extraction of Model Parameters 31

3.1 Model Formulation at Normal Bias Conditions 31

3.1.1 Determination of the Intrinsic Y-Parameters 32

3.1.2 Intrinsic Parameters in Terms of Intrinsic Y-Parameters 36

3.2 A Simplified Model of the MESFET at Pinch-off Voltage 38

3.2.1 Determination of Pad Capacitances 39

3.2.2 Lin's Method for Determining the Parasitic Elements and Pad Capacitances 41

3.2.3 A Modified Method for Determining the Pad Capacitances and Gate Parasitic Elements 45

3.3 Determination of Parasitic Inductances from Cold-Measurements 51

3.4 Extraction of MESFET Model Parameters at Normal Bias Conditions 56

3.4.1 Direct Measurements Based Techniques 56

3.4.2 Shirakawa's Optimization Technique 58

3.4.3 Ooi's Method 60

3.4.4 Bidirectional Search Optimization Method 61

3.5 A Novel Systematic Parameter-Extraction Technique 64

3.5.1 The Iterative Scheme for Estimation of L_d, L_s, C_{pg}, C_{pd}, and R_g 64

3.5.2 Estimation of the Unknown Parameters at Normal Bias Conditions 66

3.6 Extraction of Large-Signal Model Parameters 70

3.7 Nonlinear Optimization 73

3.7.1 Gauss-Newton Method 77

3.7.2 Levenberg-Marquardt Method 80

3.7.3 The First Derivative Calculation 81

3.7.4 Random Optimization Technique 82

4 Results and Analyses 83

4.1 S-Parameter Measurements Data and Error Sources 83

4.2 Shirakawa's Method 87

4.3 Modeling-Optimization Problem and Solution 91

4.4 Ooi's Method 98

4.5 Lin's Method 99

4.6 Results of the Novel Systematic Parameter-Extraction Technique 101

4.6.1 Cold-Measurement Results 101
4.6.2 Pinched-off Device Measurement Results 103
4.6.3 Iterative Scheme for Parasitics 112
4.6.4 Model Parameters at Normal Bias Conditions 116
4.7 Large-Signal Model Parameters 132

5 Conclusion 137

Appendices 140

A. Intrinsic Small-Signal Model 140
A.1 Derivation of Intrinsic Y-Parameters 140
A.2 Derivation of Intrinsic Parameters 141
B. Impedance (Admittance) Curve Fitting 146
B.1 Curve Fitting of a Series RLC Impedance 146
B.2 Curve Fitting of a Series RC Admittance 149
B.3 Curve Fitting of a Parallel GC Impedance 150
B.4 Curve Fitting of the Complex Transconductance 151
B.5 Linear Curve Fitting of an Inductive Impedance 152
C. Z-Parameters of the Transmission Line Under the Gate 154

References 160

Vita 163

List of Figures

2.1 Cross section of a GaAs MESFET device 8

2.2 Actual GaAs MESFET layouts 9

2.3 GaAs MESFET operation under different V_{ds} biasing with V_{gs}<0 11

2.4 I-V Characteristic curves for a MESFET device for different values of V_{gs} 13

2.5 MESFET models showing physical origin of elements 14

2.6 Depletion region shapes for different applied bias voltages 18

3.1 16-element small-signal MESFET model 32

3.2 Extraction of intrinsic Y-parameters from measured S-parameters 33

3.3 A simplified model of a MESFET at pinch-off voltage with V_{ds}=0 38

3.4 A reduced model at gate voltage equal to or lower than the pinch-off voltage 39

3.5 The pinch-off model in a T-topology 42

3.6 A MESFET model for V_{ds}=0 and V_{gs} fairly above pinch off voltage 52

3.7 Gate junction forward-biased in different configurations 57

3.8 A MESFET model showing the internal and external optimization parameters and branch admittances 62

3.9 Flow chart of the iterative scheme to estimate L_d, L_s, C_{pg}, C_{pd}, and R_g 65

3.10 Flow Chart for Gauss-Newton optimization method 79

4.1 S-parameters of the hypothetical model for ideal and noisy data 86

4.2 Measured S-parameters of GaAsTEK 0.8x300 μm^2 MESFET at V_{gs}=-1.2v and V_{ds}=3v 88

4.3 Objective function as well as its elementary components versus R_g plotted around the optimum component of Rg=6.5 Ω 90

4.4 The real and imaginary parts of Yint versus frequency (0.2-12.2 GHz) for both ideal and noisy data at the optimum solution 93

4.5 Histogram of all intrinsic elements calculated at the optimum point 95

4.6 Imaginary parts of cold-measurement Z-parameters for 0.8x300 μm^2 MESFET 102

4.7 Lin's Objective function versus C_{pg} and C_{pd} of the hypothetical model of Table 4.9 105

4.8 Objective function versus C_{pd} for the ideal and noisy data 107

4.9 Objective function versus C_{pd} showing good minima agreement between ideal and noisy data 108

4.10 Capacitances of the simplified pinch-off model for GaAsTEK 0.8x300 μm^2 109

4.11 Parasitic parameters versus temperature for two devices. 02-00 and 02-02 115

4.12 Measured and calculated S-parameters of the device (02-00) at V_{gs}=-1.2v and V_{ds}=4v showing good agreement 118

4.13 The different parameters of the model versus V_{gs} and V_{ds}.for the device (02-00) 123

4.14 Small-Signal model parameters versus temperature at V_{gs}=-1.2V and V_{ds}=3V for the devices (02-00) and (02-02) 130

4.15 Measured and Calculated I_{ds}, g_m, and R_{ds} versus V_{ds} for device (02-00) at different V_{gs} values 134

4.16 Effect of weighting factor combinations on different parameters versus V_{ds} at V_{gs}=0 135

A.1 Intrinsic model for MESFET devices 140

C.1 The RC transmission line under different excitation topologies 154

C.2 A simplified representation of a uniform transmission line 157

List of Tables

4.1. MESFET model parameters for a hypothetical device 84

4.2 Shirakawa's solution for noisy data with zero initial conditions 88

4.3 Complete solution set using noisy data 91

4.4 The solution when R_g=6.5ohms 97

4.5 The solution when R_i=0.5ohms 97

4.6 The solution set using Ooi's method with noisy data 99

4.7 Lin's method solution for the noisy data 100

4.8 L_s, L_d and L_g extracted at different frequency ranges 102

4.9 Hypothetical model-parameters at pinch-off voltage 104

4.10 The solution set of Lin's method for noisy data 106

4.11 The pinch-off parameters where L_s and L_d are known 108

4.12a C_{pg}, C_f, and C_{pds} of the hypothetical noisy data 110

4.12b Pinch-off full-model parameters of the hypothetical noisy data 110

4.13 Solution of the hypothetical data over the frequency band (0.2-12.2 GHz) 110

4.14 Solution of the hypothetical data over the frequency band (3.8-12.2 GHz) 111

4.15 Solution of final proposed method over the frequency band (0.2-12.2 GHz) 111

4.16 Solution of final proposed method over the frequency band (6.2-12.2 GHz) 112

4.17 L_d, L_s, C_{pg}, C_{pd}, and R_g of the GaAsTEK 0.8x300 μm^2 MESFET devices at 25°C 113

4.18 Model parameters at V_{gs}=-1.2v and V_{ds}=3v for different devices at 25°C 126

Chapter 1

Introduction

Modeling means a representation of a system, process, or device to make a description or analogy. Simulation means an imitative representation of the functioning of the modeled target by means of the functioning of another (model). My dissertation is concerned with the modeling of the *metal-semiconductor field effect transistor* (MESFET). The MESFET is usually used in the microwave range. The modeling can be divided into two categories based on the way of representation: analytical modeling and equivalent circuit modeling. The former one is formed by mathematical equations which represent or describe electron/hole transportation in the device. This model should be solved numerically or analytically. However, this model is solved numerically in most cases because of the complexity and nonlinearity of the equations. Typically, many approximations are required to obtain a useful analytical model. This is not the scope of this dissertation; and hence, we will not go into the detail of this modeling approach.

My dissertation is mainly concerned with the second type of modeling, equivalent circuit modeling. In this modeling scheme, a circuit is proposed based on the expected physical behavior of the device. This circuit consists of lumped elements: (e.g. resistances, capacitors, inductors, sources), and distributed elements such as transmission lines if needed. Our basic task is to calculate those elements (parameters) from device measurements.

In a signal-level categorization, more than one model may be used to represent the same device depending on the level of the excitation of signal. Typically, two models are used for a device: small-signal model and large-signal model. A small-signal model represents the behavior of the device under low level of input excitation. This model is useful in small-signal amplifier designs. In contrast, a large-signal model represents the behavior of the device under large level of input excitation. This model is usually used in the design of such circuit having large voltages propagating through it such as: power

amplifiers and oscillators. The large-signal model is vital for calculations of nonlinear information: harmonic content, intermodulation distortion, saturation…etc.

Usually, the small-signal model is the corner stone of the large-signal model. If an accurate large-signal model is required, an accurate small-signal model should be devised first. In order to extract a large-signal model, small-signal model parameters should be extracted at different bias points through out the region of interest. Those parameters should fit bias dependent equations to represent the dependence of the device on the bias point.

The main focus of my research is devoted to extract an accurate small-signal model from Scattering-parameter measurements (S-parameters). Many extraction techniques are discussed in detail. Pros and cons of each technique along with range of validity are disputed. A robust technique is concluded and used to extract an accurate small-signal model over any frequency range from S-parameter measurements whose accuracy is reasonable.

The small-signal parameters, extracted at different bias points, are used to derive a large-signal model for the drain-source current. Some thermal results are also used to shed some light on the effect of temperature variations on the model parameters.

It is worthy to note that the modeling techniques presented in this dissertation can be applied to *high electron mobility transistors* (HEMTs) just as well as they are applicable to MESFETs. The fact is that although the two devices are physically and structurally different, they have the same equivalent circuit model with different parameter values. HEMT devices operate over larger frequency ranges than those of MESFET devices; and thus the model parameter values reflect this distinction.

1.1 Why GaAs MESFET Modeling:

GaAs MESFET has found many applications in the microwave and millimeter-wave for the past three decades. Having accurate models for GaAs MESFET devices would facilitate the use of circuit design and analysis tool to allow better use and evaluation of these devices. Most of the currently available models in computer-aided design (CAD) packages are circuit models. Efforts are exerted to develop black box models and fast physical models. Nevertheless, the circuit models are expected to stay for some time because of their computational efficiency and availability in the commercial CAD packages. New models can also be developed into CAD tools easily, or the built-in models can be upgraded with a little effort. Some CAD packages are available in the market such as: PSPICE, Agilent EEsof Series IV and Advanced Design System (ADS).

It is obvious that the accuracy of the model determines the accuracy of the design analysis. An accurate model is essential for quick design and fabrication process development. The inaccuracy in the model results in many trials before you get a working design or a successful process. Moreover, modern communication systems require more sophisticated monolithic microwave integrated circuits (MMICs) with smaller and smaller sizes. The miniaturization of MMICs and increasing the chip density emphasized the need of accurate models to minimize the number of design and fabrication cycles.

The small-signal model is the corner stone of the large-signal model. The more accurate the small-signal model is, the more accurate the large-signal model is. The small-signal model provides a useful tool for the device performance analysis: gain, noise…etc. It also provides valuable insight into the operation of the device in a circuit.

On the other hand, the large-signal model should take into account as much physical phenomena as possible [1]. Accurate large-signal models take into account phenomena as: trap effects, low frequency dispersion and heating effects. Heating effects means that the model should be a function of temperature, thermal model,. As a step towards a large-signal thermal model, a small-signal thermal model is essential whose parameters are

functions of bias voltages and temperature. The large-signal model plays an important role in describing the nonlinear behavior of the device. Nonlinear behavior includes many parameters such as: harmonic content, intermodulation distortion, saturation…etc.

When we talk about the modeling of GaAs MESFETs, we also have to talk about the uses and applications of GaAs MESFET itself. The MESFET has been used in the microwave industry for many years. The use of MESFET found many applications in the military, commercial, research fields for its low noise performance in the microwave range. The MESFET has been used since the beginning of the 1970's when it showed promising properties of low noise amplification. The demand for the lowest possible noise figure at higher frequencies has encouraged research on the physics of the device and has had a great impact on its technology. Fabrication of MESFETs is also compatible with the industry of monolithic circuitry. This advantage reinforced the development and interest of the MESFET technology; it also ensures that MESFET devices will continue to serve the communication industry for some time. The HEMT has emerged to overcome the performance limits of the MESFET. However, the manufacturing technology of the HEMT is not as mature as that of the MESFET at this time. The MESFET is used as the active device for low noise and power amplifiers as well as for transfer switches, attenuators, oscillators and mixers. In the following paragraphs, a brief overview of these various uses of MESFET devices will be presented.

MESFETs as LNAs: GaAs MESFET small-signal low-noise amplifiers (LNAs) are widely used in various communication applications. These circuits are designed to operate as linear gain blocks, with specific requirements determined by their location within the system. The noise added by these amplifiers can be kept low, thus yielding improved signal-to-noise ratio performance. Amplifier applications range from a few hundreds of MHz to 40 GHz, and some laboratory results indicate its usefulness at 60 GHz. Applications of MESFET amplifiers include medium–band and broadband bandpass amplifiers, ultrabroadband lowpass amplifiers, very low noise medium-bandwidth amplifiers and ultralow noise cryogenically cooled amplifiers [2].

MESFETs as Power Amplifiers: Semiconductor power amplifiers are typically used in communication systems to provide sufficient signal power to allow transmission from one site to another. The popularity of mobile and hand-held communication devices has pushed the development of compact and efficient power amplifiers. Additionally, the size, weight, and power constraints on satellite communication systems require such amplifiers at high frequencies. Power amplifiers are usually designed for maximum efficiency, in contrary to LNAs which are usually designed for maximum linearity and minimum noise. Output power and gain are also important parameters in the design of power amplifiers. A MESFET power amplifier can provide power as high as 17 W [2].

MESFETs as Oscillators: Oscillators are used in many systems, along with the mixers, to perform frequency conversion of desired signals. MESFET-based oscillators have been popular because of their dc-to-RF conversion efficiencies. In addition, the three terminal devices allow greater design flexibility to meet specific performance requirements.

MESFETs as Mixers: A mixer is a three-port device that functions to convert an input RF signal in conjunction with a LO signal to an intermediate signal termed IF on which further precise signal processing is performed [2]. Ideally, a mixer performs this frequency conversion with perfect fidelity and thus generates no intermodulation distortion (IMD). Other desirable characteristics include high isolation between three ports and a low noise figure along with minimal loss or preferably gain while performing frequency conversion. Traditionally, mixers have been designed based on the nonlinear voltage-current response of Schottky diodes in order to perform frequency conversion. All diode-based mixers suffer from two problems: conversion loss and the need of large local oscillator power to drive the diodes to achieve efficient frequency conversion.

More recently, MESFETs are being used as the nonlinear element in mixers; primarily for reasons of compatibility with MMIC processing and to achieve conversion gain. Frequency conversion of the RF signal to an IF results in a larger amplitude signal. This conversion gain, rather than loss, cancelled the requirement of a LNA preceding the

mixer in some applications. This may also result in a net decrease in dc power, which is particularly important for portable and space-based equipment.

MESFETs as Attenuators: A Variable attenuator is a two-port device that allows adjustment of the signal amplitude by application of an external voltage or current. The attenuation is proportional to voltage or current. If it is directly proportional, the attenuator is termed linearized. The attenuator should perform this task with low harmonic distortion, minimal insertion loss, and low VSWR at its ports. Attenuators commonly employed in feedback networks, communication systems, and in temperature compensation networks to maintain constant signal amplitude.

A variable attenuator basically consists of a set of variable resistors connected in “pi” or “tee” topologies. Traditionally, PIN diodes are used as the variable resistors whose resistance is proportional to the applied dc current. Although PIN diodes exhibit low parasitic capacitance and in turn they are insensitive to changes in frequency, they require considerable dc bias current to obtain low resistances and also require external bias circuitry. In contrast, MESFETs are being used to realize the variable resistive element in attenuator avoiding the disadvantages of PIN diodes. In this case, the MESFET is unbiased ($V_{ds} = 0$, $I_{ds} = 0$), and the drain-source resistance is varied with an applied gate potential. Unlike a PIN-based attenuator, MESFET-based attenuators are voltage controlled and require very little dc power.

As we have seen, MESFETs are employed in a wide range of applications. The availability of accurate small- and large-signal models is extremely important to evaluate the design of MESFET circuits more accurately at lower cost. A small-signal model is typically needed for designing of (LNAs) while MESFET large-signal models are needed in the design of power amplifiers, oscillators, mixers, and attenuators.

1.2 Dissertation Organization:

Chapter 2 provides a brief discussion of the physical structure of MESFET devices. The physical operation is also explained qualitatively along with some features of the I-V characteristic curves of MESFET devices. This chapter also discusses large- and small-signal models, in addition the physical origin of each element is clarified. Each element of the small-signal model is discussed to explore the physical meaning of each element along with the factors which affect its value. The previous work done in the modeling field will be also explored.

Various optimization-based extraction techniques for small-signal models are explained in detail in chapter 3. Strengths and weaknesses of each technique are presented. Different small-signal models for different schemes are described. Models at different bias conditions as well as their implications are explained as well. Pinched-off device models are derived and discussed, based on different proposed extraction schemes. A Cold-measurement model is presented; its simplicity is explored for the extraction of some parameters. Our new technique is explained showing its strengths versus other techniques. The extraction of a drain-source current model from the small-signal parameters is also demonstrated. Some least-squares nonlinear optimization techniques along with a simple random optimization technique are mathematically described.

Chapter 4 shows results of the different optimization techniques described in chapter 3. The reliability of each technique is provided and problems are attacked. The optimization extraction problems are interpreted and solutions are proposed. Comparison between different techniques is also supplied. The implication of the small-signal parameters on the large-signal model is also discussed. Some thermal analysis for the small-signal model is presented.

Finally, some conclusions are derived in chapter 5. Possible future work is also introduced.

Chapter 2
MESFET Physics and Modeling

Understanding the physical structure and operation of a semiconductor device is a crucial aspect in the device modeling process. A device model basically reflects how we understand the physics and physical operation of this device. The method of characterization of this device depends on its physics. This chapter will discuss some physical aspects of a MESFET device. A small-signal model will be proposed and discussed in terms of physical reflections.

2.1 Physical Structure:

A MESFET device is a three-terminal device like any transistor [3], [4]. Since it is a FET transistor, it has three electrodes: drain, source, and gate as shown in Figure 2.1. For microwave and millimeter wave frequencies, the MESFET devices are fabricated using GaAs material. GaAs has attractive features at high frequencies since the carrier mobility is much larger than that of silicon. In addition, electron saturation velocity for GaAs is higher than that for silicon which results in increased operating frequency range.

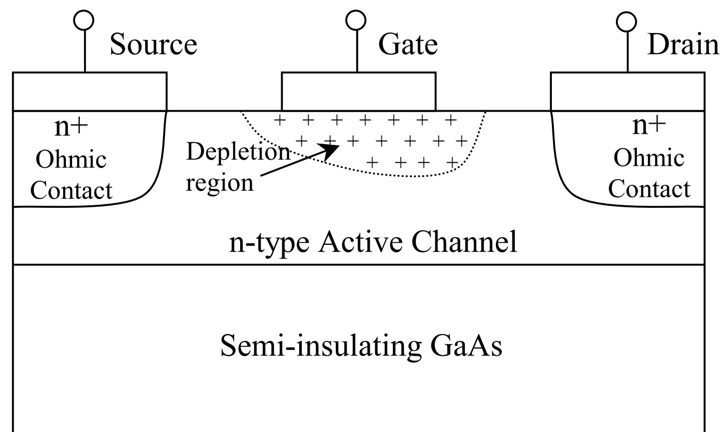

Figure 2.1 Cross section of a GaAs MESFET device.

A thin layer of n-type GaAs is deposited on top of a semi-insulating GaAs substrate. The back face of the substrate is covered with a metal Au/Ge alloy [5], which is usually connected to the source terminal during measurements. Both drain and source are connected to the n-type layer through n+ ohmic contacts. The metal of the source and drain electrodes can be made of Au/Ge alloy, which is coated with Ti, Pt, and Au layers, respectively. The gate is a thin layer of metal, usually aluminum coated with Au, deposited on top of the n-type layer between drain and source. The metal semiconductor junction of the gate represents a Schottky barrier junction. This junction is used to control the height of the active channel layer beneath the gate by applying a bias voltage to the gate. The area just beneath the gate is charge depleted as per the applied bias.

The most important dimensions of a MESFET device are the gate length "L" and width "W". Those dimensions usually characterize the device. For example, a device can be referred as 0.3x300 μm^2 when the gate length is equal to 0.3 μm and the gate width is equal to 300 μm. A typical value of gate length ranges from 0.1 to 1 μm. The gate length determines the maximum frequency of operation. As the gate length decreases, the maximum frequency increases [3]. On the other hand, the gate width determines the performance of the device such as the maximum current capability.

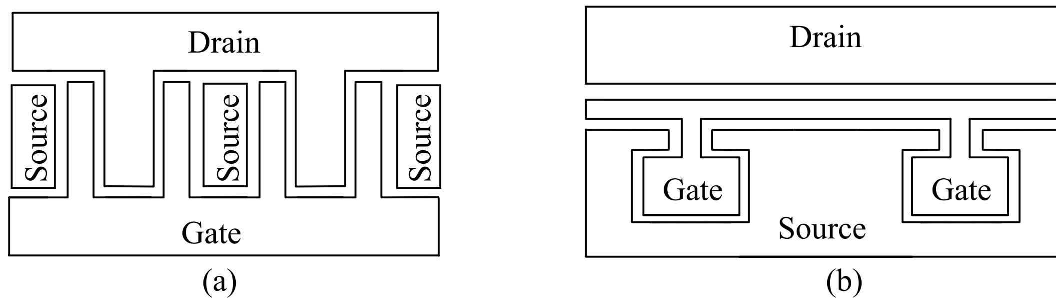

Figure 2.2. Actual GaAs MESFET layouts: (a) interdigitated-gate, (b) π-gate.

The actual layout of a MESFET device is more complex than that shown in Figure 2.1. Figure 2.2 shows two different examples of actual layouts: interdigitated-gate and π-gate layout. Those layouts are usually used to increase the gate width while decreasing the parasitic gate resistance. The patterns shown in Figure 2.2 can be repeated to achieve the

required gate width. This layout implies crossover areas between metalization traces, which should be filled with either silicon dioxide or air [5].

2.2 Principles of the GaAs MESFET Operation:

A MESFET device is biased by applying two voltages: V_{gs} between gate and source and V_{ds} between drain and source [1]. These voltages control the channel current between the drain and source by varying the height of the gate-depletion region and the longitudinal electric field. The operation can be explained qualitatively without going into deep physical analysis. Three cases can be recognized for the I_{ds}-V_{ds} characteristic curve of the MESFET, if V_{gs} is larger than the pinch-off voltage,: low V_{ds} voltage where I_{ds} is linearly proportional to V_{ds}, high V_{ds} where the current is almost constant, and moderate V_{ds} where I_{ds} has nonlinear relationship of V_{ds}.

Imagine first that $V_{gs}=0$ and V_{ds} is raised from zero to some low value as shown in Figure 2.3(a). When $V_{gs}=0$, the depletion region under the Schottky-barrier gate is relatively narrow, and as V_{ds} is raised, a longitudinal electric field and current are established in the channel. Because of V_{ds}, the voltage across the depletion region is greater at the drain end than at the source end, so the depletion region becomes wider at the drain end.

The narrowing of the channel and the increased V_{ds} increase the electric field near the drain, causing the electrons to move faster. Although the channel depth, and in turn channel's conductive cross section, is reduced, the net effect is increased current. When V_{ds} is low, the current is approximately proportional to V_{ds}. However, if the gate reverse bias is increased while the drain bias is held constant, the depletion region widens and the conductive channel becomes narrower, reducing the current. When $V_{gs}=V_p$, the pinch-off voltage, the channel is fully depleted and the drain current is zero, regardless of the value of V_{ds}. Thus, both V_{gs} and V_{ds} can be used to control the drain current. When the MESFET is operated under such bias voltages, where both V_{gs} and V_{ds} have a strong

effect on the drain current, it is said to be in its linear or voltage controlled resistor region.

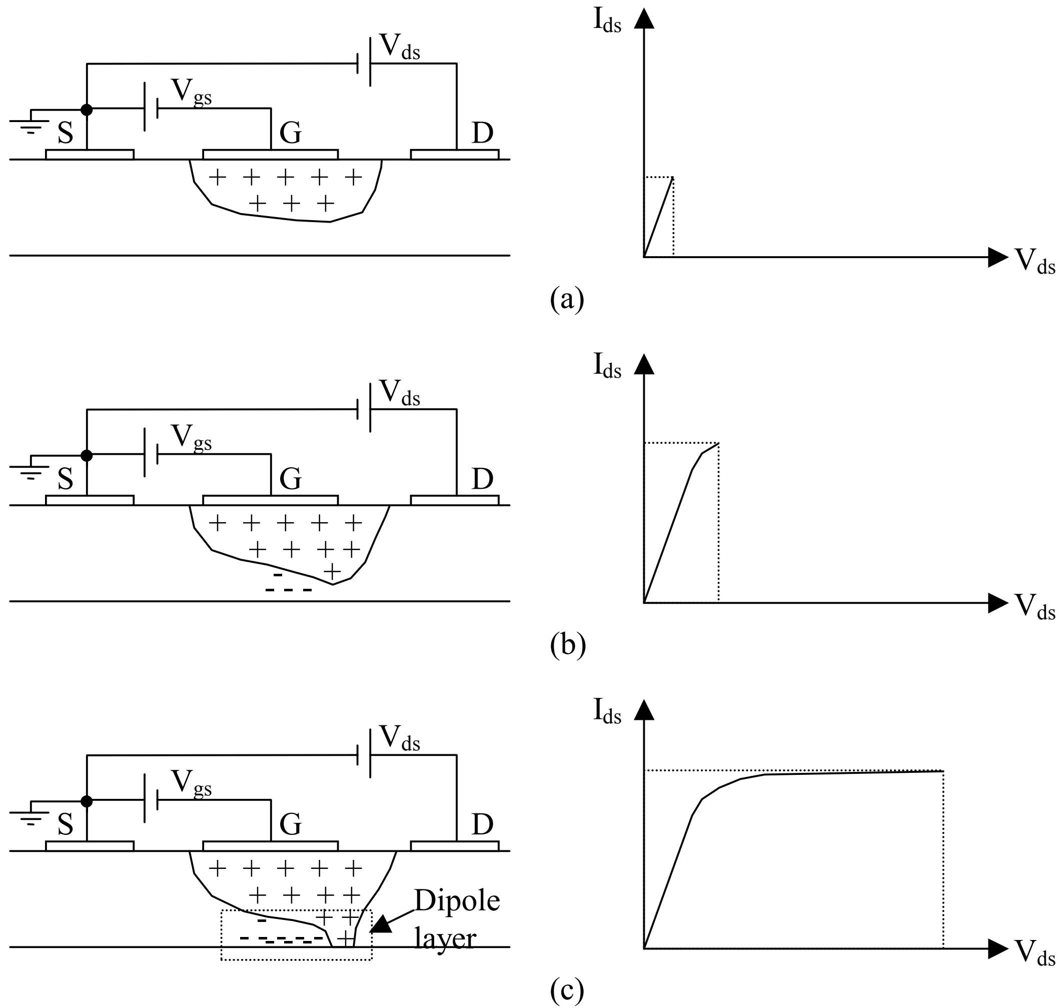

Figure 2.3 GaAs MESFET operation under different V_{ds} biasing with $V_{gs} \leq 0$: (a) Linear region (V_{ds} is very low), (b) V_{ds} at the onset of saturation, (c) V_{ds} is big.

If V_{ds} is raised further, as shown in Figure 2.3(b), while V_{gs} is larger than the pinch-off voltage, the channel current increases, the depletion region becomes deeper at the drain end, and the conductive channel becomes narrower. The current clearly must be constant throughout the channel. As a result, and as long as the conductive channel near the drain becomes narrower, the electrons must move faster. However, the electron velocity cannot

increase indefinitely; the average velocity of the electrons in GaAs cannot exceed a velocity called the saturated drift velocity, approximately 1.3×10^7 cm/s.

If V_{ds} is increased beyond the value that causes velocity saturation (usually only a few tenths of a volt), the electron concentration rather than velocity must increase in order to maintain current continuity. Accordingly, a region of electron accumulation forms near the end of the gate. Conversely, after the electrons transit the channel and move at saturated velocity into the wide area between the gate and drain, an electron depletion region is formed. The depletion region is positively charged because of the positive donor ions remaining in the crystal. As V_{ds} is increased further, as shown in Figure 2.3(c), progressively more of the voltage increase is dropped across this region to enforce the electrons to cross it and less is dropped across the unsaturated part of the channel. This region is called a dipole layer or charge domain. Eventually, a point is reached where further increase in V_{ds} is dropped entirely across the charge domain and does not substantially increase the drain current. At this point, the electrons move at saturated drift velocity over a large part of the channel length. When the MESFET is operated in this manner, which is the normal mode of operation for small-signal devices, it is said to be in its saturated region.

Accurate models may include the effect of the charge domain in some way. Therefore, some models include a capacitor between the drain and the gate-source equivalent circuit to account for the charge domain.

The I-V characteristic curves of a MESFET device are shown in Figure 2.4 for an ideal and actual MESFET. The curves are plotted for different values of V_{gs}. It is obvious that the actual I-V curve exhibits finite positive slope in the saturation region. Many reasons may be responsible for this phenomenon. One of the most dominant reasons in a short gate device is the carrier injection into the semi-insulating substrate. This finite slope is the source of the finite output conductance in a MESFET model.

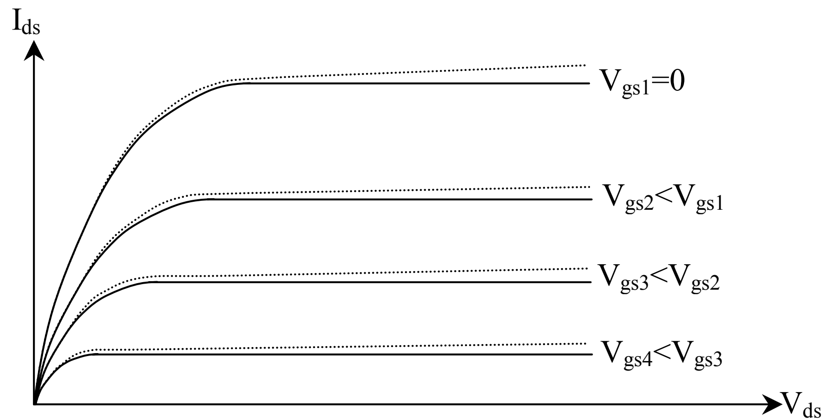

Figure 2.4 I-V Characteristic curves for a MESFET device for different values of V_{gs}; ideal current is drawn in solid curve while dashed curve indicates the actual current.

2.3 MESFET Models:

The large-signal model can be proposed based on the physical structure of the MESFET device. Most of the suggested models are based on the model shown in Figure 2.5 [2]. Both large and small-signal models are shown in the same figure. The small-signal model can be derived directly from the large-signal model. The relationship between the physical structure and model elements are also indicated. This model is a lumped-element model which is valid over a frequency range of several tens of GHz.

The physical meaning of each element is clearly interpreted. R_g is the ohmic resistance of the gate while R_s and R_d are the source and drain ohmic resistances, respectively. L_g is the inductance of the gate while L_s and L_d are the inductances of the source and the drain metalization, respectively. R_i is the resistance of the semiconductor region under the gate, between the source and the channel. C_{ds} the drain-source capacitance, which is dominated by geometric capacitance and is often treated as a constant. C_{gs} and C_{gd} are the channel capacitances which in general are nonlinear. I_{ds} is the controlled

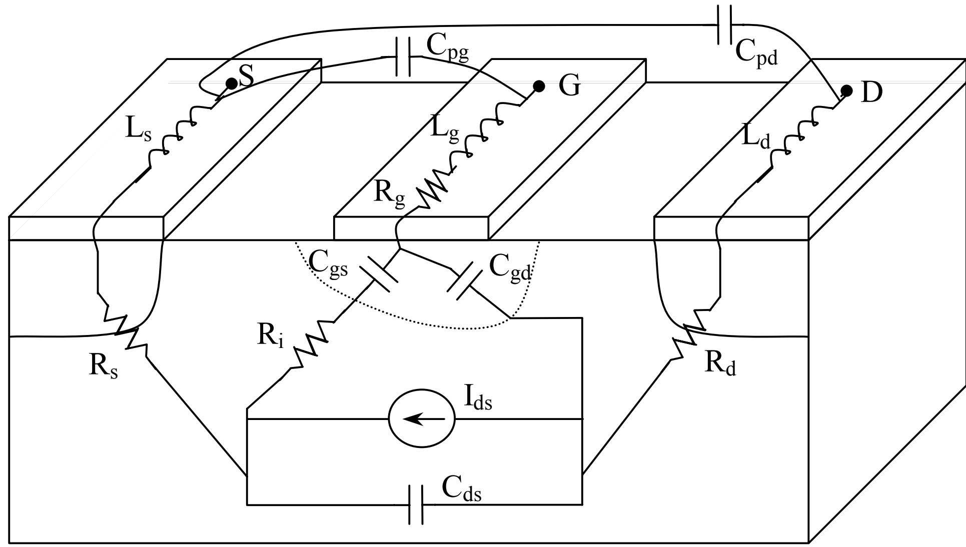

(a)

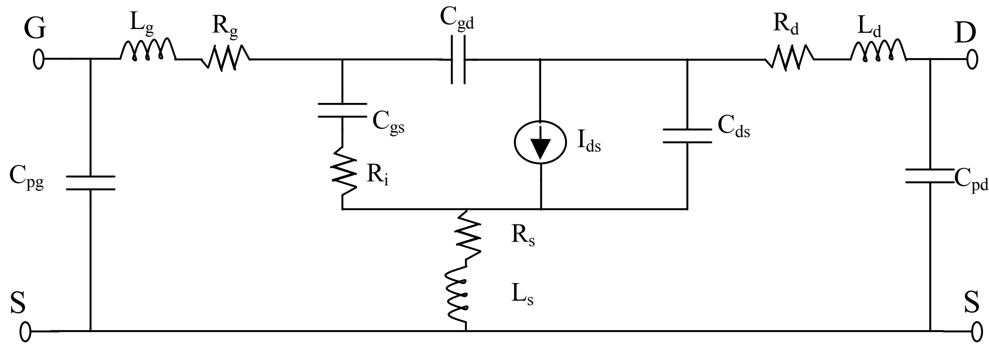

(b)

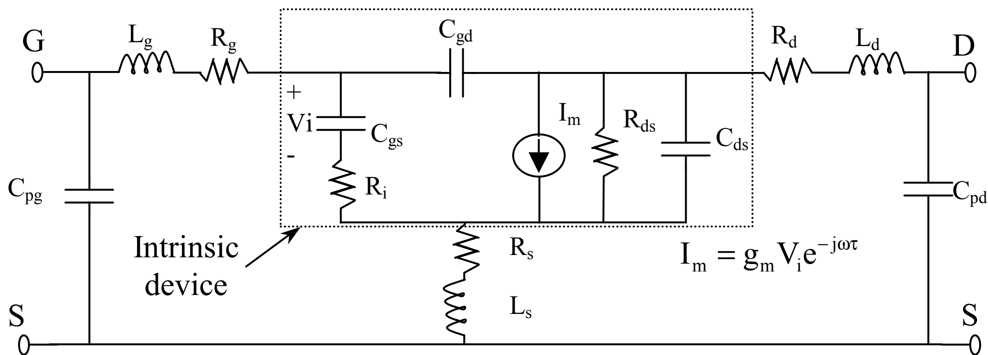

(c)

Figure 2.5 MESFET models showing physical origin of elements: (a) physical origin of each element, (b) large-signal model, (c) small-signal model.

drain-source current from which the transconductane g_m, transit time delay τ, and output resistance R_{ds} can be calculated. C_{pg} and C_{pd} are the pad capacitances of both gate and drain, respectively, on one side with respect to the source on the other side.

If voltages are expected to be great enough to forward–bias or reverse avalanche-breakdown the gate junction, one can include diodes in parallel with C_{gs} and C_{gd}. Such diodes are of limited practical value, however, because operation with gate-channel avalanche breakdown or high values of rectified gate current usually destroys the device. Some of the model elements are nonlinearly dependent on the internal voltages V_{gs} and V_{ds}. Others are linear, or can be approximated as linear elements. I_{ds}, C_{gs}, and C_{gd} are usually nonlinear elements for their strong dependence on V_{gs} and V_{ds}.

On the other hand, the circuit model can be divided into two parts: the extrinsic parameters and the intrinsic parameters. The intrinsic parameters characterize the active region under the gate and are functions of biasing conditions, whereas the extrinsic parameters depend, at least to a first approximation, only on the technological parameters. The intrinsic parameters include C_{gs}, R_i, C_{gd}, g_m, τ, R_{ds}, and C_{ds} whereas the extrinsic parameters include all other elements in the model C_{pg}, C_{pd}, R_g, R_d, R_s, L_g, L_d, and L_s. Some of the intrinsic elements can be assumed linear for their weak dependence on the internal voltages, those elements are R_i, τ, and C_{ds}. In contrast, some of the extrinsic elements may be nonlinear if their dependence on the internal voltages is significant. We will discuss the significance of each element of the small-signal model in the following subsections.

2.3.1 Parasitic Inductances:

The parasitic inductances are the inductances of the extrinsic part of circuit model which include L_g, L_d, and L_s. Those inductances arise primarily from metal contact pads deposited on the device surface. For short gate length devices, the gate inductance is usually the largest of the three, although this is a function of the particular layout employed. Typically, L_g and L_d are on the order of 5 to 10 pH. The source inductance is often small, about 1 pH. Note that these inductances exist for the bare die device, so, any other inductances such as parasitic bond wire inductances or parasitic package inductances must also be accounted for in the complete circuit model of the packaged

device. In many cases, bonding inductances are on the order of 0.1 to 0.3 nH and dominate the device parasitics.

2.3.2 Parasitic Resistances:

The parasitic resistances R_g, R_d, and R_s are also included in the extrinsic part of the circuit model. The resistances R_s and R_d are included to account for the contact resistance of the ohmic contacts between the metal electrodes and the n+-GaAs as well as any bulk resistance leading up to the active channel. The gate resistance R_g results from the metalization resistance of the gate Schottky contact. All three resistances are on the order of a few ohms. Although measurements of R_s and R_d indicate a slight bias dependence in these values, they are held constant in the large-signal models commonly available in the commercial simulators nowadays. However, accurate models should take into consideration their bias dependence, especially if their values are significantly depends on the bias voltages. All parasitic resistance values can be estimated either from forward DC conduction measurements or directly from S-parameters using an optimization technique. However, the latter technique is preferable for more accurate results because it calculates the resistance values from typical high frequency data at the bias point of concern.

2.3.3 Pad Capacitances:

These capacitances are also included in the extrinsic part of the circuit model. The pad capacitances come from the stray capacitance between the metal pads. The pad capacitance consists of crossover capacitance of the metal lines and the capacitance between the pad and the back face of the semi-insulating substrate, which is usually connected to the source terminal. However, the crossover capacitance is usually much smaller than the substrate capacitance [5]. Two pad capacitances are often included in the circuit model: C_{pg} gate pad capacitance and C_{pd} drain pad capacitance. C_{pg} is the capacitance between gate and source pads whereas C_{pd} is the capacitance between the drain and source pads. Although the pad capacitance between gate and drain pads can be

included in the circuit model, it is usually neglected for its small value compared to other capacitance values in the model. C_{pg} and C_{pd} are typically on the order of a few tens of fF. Nevertheless, they may be omitted from many models in the literature if their values are insignificant or if their effect can be accounted for throughout other capacitive elements in the circuit. On the other side, pad capacitances may be placed in two different positions in the model, either on the most outer terminals of the model as seen in Figure 2.5 or between the corresponding parasitic inductances and resistances. Pad capacitance values depend on the utilized layout. Pad capacitances can be estimated either from special structures without the active device or directly from S-parameter measurements using an optimization technique.

2.3.4 Intrinsic Capacitances:

Intrinsic capacitances are indicated in the model by C_{gs}, C_{gd}, and C_{ds}. C_{gs} and C_{gd} model the change in the depletion charge with respect to the gate-source and gate-drain voltages, respectively. Figure 2.6 shows the depletion region beneath the gate for a symmetric structure where the gate is located directly in the middle of the gap between the source and the drain terminals. Figure 2.6(a) represents the symmetric bias case in which $V_{gs}=V_{gd}$. Figure 2.6(b) represents the case in which the gate-drain reverse bias is greater than the gate-source reverse bias. This case represents the normal MESFET bias conditions in most applications. Figure 2.6 is only used to clarify the physics of both C_{gs} and C_{gd}. However, the discussion is also valid for any geometrical structure and bias conditions.

The distribution of the depletion charge is symmetric with respect to the drain and source in Figure 2.6(a). On the other hand, the depletion charge extends deeper at the drain end of the gate than at the source end of the gate, and it also extends closer to the drain than to the source. This charge redistribution in the depletion region with the bias voltage variation identifies the two depletion capacitances C_{gs} and C_{gd}. The charge of the depletion region is shared between C_{gs} and C_{gd}. Thus, they should be defined carefully as:

$$C_{gs} = \left.\frac{dQ_g}{dV_{gs}}\right|_{V_{gd}=\text{constant}} \tag{2.1a}$$

$$C_{gd} = \left.\frac{dQ_g}{dV_{gd}}\right|_{V_{gs}=\text{constant}} \tag{2.1b}$$

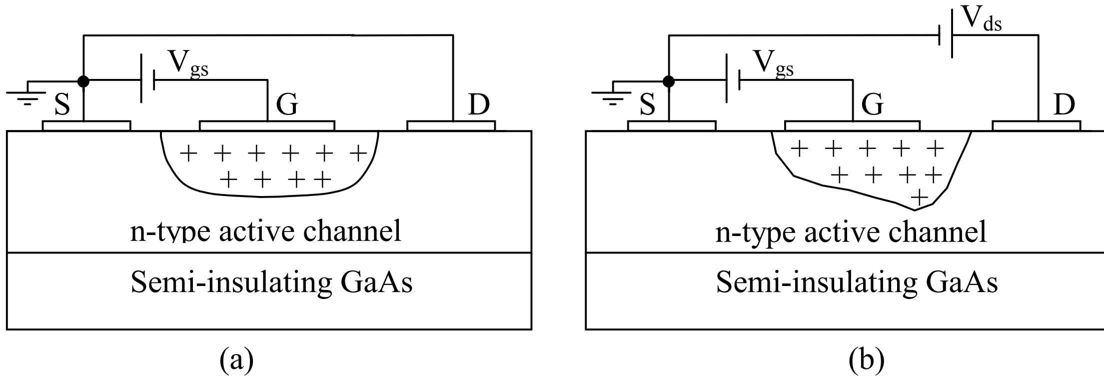

Figure 2.6 Depletion region shapes for different applied bias voltages: (a) gate-source voltage is equal to gate-drain voltage, (b) gate-drain reverse bias is greater than gate-source reverse bias.

Under normal operation conditions, V_{gs} and V_{ds} are the DC controlling bias voltages. For this reason, the gate to source capacitance is often defined as:

$$C_{gs} = \left.\frac{dQ_g}{dV_{gs}}\right|_{V_{ds}=\text{constant}} \tag{2.2}$$

Equations (2.1a) and (2.2) are not equivalent, but slightly different quantities. The distinction is usually minor, but can be significant if calculations are based on a physically based model in which the depletion charge is defined by a mathematical expression. When capacitance is determined by measurements or derived from empirical models, the capacitance definition given by equations (2.1a) and (2.2) are not applied. Instead, the capacitance values are defined in terms of an equivalent circuit, and so, the values are determined to accurately predict the device behavior. Thus, it does not matter

in our thesis which definition of C_{gs} should be taken because C_{gs} is calculated from S-parameter measurements. One might also have noticed that the voltages indicated in the capacitance definitions are the internal voltages, and not the external terminal voltages.

Under typical MESFET bias conditions, C_{gs} is larger than C_{gd} because it models the change in depletion charge resulting from fluctuations in the gate-source voltage while the gate-source reverse bias voltage is less than the gate-drain reverse bias voltage. It is well known from depletion capacitance analysis that the depletion capacitance decreases as the reverse junction voltage increases. For this reason and under normal bias conditions, the gate-drain capacitance C_{gd} is considerably smaller in magnitude than C_{gs}; nevertheless, C_{gd} is critical to obtaining accurate S-parameter predictions.

The drain-source Capacitance C_{ds} is included in the equivalent circuit to account for geometric capacitance effects between the source and drain electrodes. It is usually not considered to be bias dependent for the purposes of device modeling. Values for C_{gs} are typically on the order of 1 pF/mm gate width under normal MESFET bias conditions. The values of C_{gd} and C_{ds} are about one tenth of the value of C_{gs}. Moreover, because of symmetry, C_{gs} and C_{gd} are approximately equal for V_{ds}=0.

2.3.5 Charging Resistance R_i:

Although the charging resistance R_i represents the intrinsic resistance under the gate between the source and the channel, it is included primarily to improve the match to S_{11}. For many devices, however, the presence of R_g is sufficient to match the real part of S_{11}. So, R_i is difficult to extract and is of questionable physical significance. The difficult discrimination between R_i and R_g in the extraction process will be discussed in Chapter 3, also, some results will be introduced in Chapter 4.

2.3.6 Transconductance:

The intrinsic gain mechanism of the MESFET is provided by the transconductance. The transconductance g_m is a measure of the incremental change in the output current I_{ds} for a given change in the internal input voltage V_{gs}. The internal input voltage is the voltage across the gate source junction. In other words, the device transconductance is defined as the slope of the I_{ds}-V_{gs} characteristics with the drain-source voltage held constant. The mathematical statement of this definition can be expressed as:

$$g_m = \left.\frac{\partial I_{ds}}{\partial V_{gs}}\right|_{V_{ds}=\text{constant}} \tag{2.3}$$

The transconductance of the device is one of the most important indicators of the device quality for microwave and millimeter wave applications. When all other characteristics are equal, a device with high transconductance will provide greater gains and superior high frequency performance. The transconductance suffers from what is called low frequency dispersion. The low frequency dispersion is the phenomenon of a parameter variation at low frequencies. The low frequency dispersion takes place as a result of the deep levels in the device structure. So, it significantly depends on the semiconductor material quality and fabrication processes.

Therefore, the transconductance varies with frequency below a frequency of about 1 MHz. RF values of transconductance are typically 5 to 25% lower than DC values for a GaAs MESFET. Transconductance values vary directly with gate width and inversely with gate length.

2.3.7 Transit Time:

The transconductance cannot respond instantaneously to changes in the gate-source voltage. The delay inherent to this process is described by the transit time (transconductance delay) τ. Physically, the transconductance delay represents the time it

takes for the charge to redistribute itself after a fluctuation of the gate voltage. Typical values of τ are on the order of 1 pSec. From physical considerations, transit time is expected to decrease with decreasing gate length.

2.3.8 Output Resistance:

The output resistance R_{ds} is the incremental resistance between drain and source, and it is more convenient to be explained in terms of its reciprocal, the output conductance g_{ds}. The output conductance is a measure of the incremental change in output current I_{ds} with the output voltage V_{ds}. So, it can be defined as the slope of the I_{ds}-V_{ds} characteristics with the gate-source voltage held constant. Mathematically, the output conductance and resistance can be defined by:

$$g_{ds} = \frac{1}{R_{ds}} = \left.\frac{\partial I_{ds}}{\partial V_{ds}}\right|_{V_{gs}=\text{constant}} \tag{2.4}$$

The output conductance of the device is an important characteristic in analog applications. It plays a significant role in determining the maximum voltage gain attainable from a device and is extremely important for determining optimum output matching properties. In general, it is desirable to have a device with extremely high output resistance, or equivalently, low output conductance. Values of g_{ds} are on the order of 1 mS/mm gate width at typical MESFET amplifier biases. Also, as gate length is reduced, output conductance tends to increase. The low frequency dispersion is more significant in output conductance than in the transconductance. The RF output conductance can be more than 100% higher than the DC output conductance. The RF values for both transconductance and output conductance are of primary concern for small-signal modeling applications while both RF and DC values are important for accurate large-signal modeling.

2.4 Literature Review:

The basic equivalent circuit model shown in Figure 2.5(c) has been the key for many researches and it is commonly used in CADs. Some researchers modified it slightly to increase its accuracy or to ease its parameter-extraction process. In this section, we will review the previous work done to extract the parameters of this model.

Two main trends for parameter extraction process were typically followed by previous researchers. The first trend (e.g. [6], [7]) is to extract the extrinsic parameters C_{pg}, C_{pd}, R_g, R_d, R_s, L_g, L_d, and L_s, then the remaining (intrinsic) parameters are extracted analytically (or by optimization). The second trend (e.g. [8]) is to extract all the parameters using an optimization algorithm.

Minasian [9] proposed a simplified model working up to 10 GHz. In his model, he removed all the extrinsic parameters. The relation between his model and the more complex model was presented and the characteristics of both models were compared. The elements values were calculated analytically from the measurements and his simple model showed good agreement with the measured parameters up to 10 GHz for 1 µm gate length. However, the values of the model's elements did not represent their physical values because they had to compensate for the removed elements.

Fukui [10] described a technique to determine the basic properties of the active channel of a GaAs MESFET along with the parasitic resistances R_g, R_d, and R_s. His technique was based on the forward I-V characteristics of a gate junction while source and drain are connected together, source is alone, and drain is alone. His technique was employed by some authors after him to extract the complete model's parameters where parasitic resistances are known. Nevertheless, the values of R_d, and R_s are bias dependent. As a result, their values at reverse gate bias, where most of the applications are, are different from those extracted by Fukui method. Moreover, The DC value of the gate resistance obtained from the Fukui measurements is not directly applicable to the small-signal microwave equivalent circuit model because of the skin effect [11].

Other techniques were introduced to determine parasitic resistances from forward-bias gate-junction measurements. Kang et al. [12] presented a technique to determine parasitic resistances as well as the electron saturation velocity of ion-implanted GaAs FETs. Their technique is based on the "end" resistance measurements. The theory of this method is developed and used to determine the resistances. The "end" resistance measurement technique implies applying forward bias voltage across the gate junction so that the flowing gate current creates a voltage drop across the source series resistance. The drain contact is floating so that the drain section of the device acts as a "probe". The channel resistance should be taken into account for accurate determination.

Another technique was proposed by Yang et al. [13]. They described a method to measure the source and drain resistances without correcting for the channel resistance or the gate resistance. This method had advantages: both resistances were measured by direct measurements without the knowledge of the physical parameters of the device. However, it suffers from the common problem of the forward bias based techniques, that there is a discrepancy between forward bias and reverse bias estimations.

Lehovec [14] showed that a model of unbiased drain-source MESFET is fairly simpler than that of normal bias voltages. For zero drain-source voltage, the region under the gate can be described by a distributed uniform RC transmission line. He used this simple model to determine average mobility as well as impurity concentration for epitaxial semiconducting films on insulating substrates.

Diamond et al. [15] exploited the same concept of Lehovec [14] at zero drain-source voltage. They derived analytical expressions for Z-parameters of the model to determine the parasitic elements. The parasitic inductances were calculated by optimizing them over the frequency range of interest to best fit the imaginary parts of Z-parameters data at any gate bias voltage. The parasitic resistances were calculated from the real parts of Z-parameters under different gate bias voltages. Gate bias voltages should be chosen such that a channel opening is higher than 20%.

Curtice et al. [16] developed a procedure to extract a full model for a carrier-mounted GaAs MESFET. They used Fukui [10] method to determine parasitic resistances. They also used Diamond et al. [15] concept at cold S-parameter measurements with zero drain-to-source voltage to extract parasitic inductances L_g, L_d, and L_s, and parasitic capacitances C_{pg}, and C_{pd} by optimizing them to decrease the error between the measured S-parameters and calculated ones from the simple model. Intrinsic parameters were extracted by optimization for best fit with the experimental data. They showed that it is not possible to determine all the parasitics from cold measurements because the error function is less sensitive to changes in parasitic resistances.

Vaitkus [17] introduced a method to calculate the uncertainties of the values of a submicron-gate GaAs MESFET equivalent circuit elements extracted by an optimization technique to fit measured S-parameters. He showed that the levels of uncertainty are related to the bandwidth of the S-parameters and the number of elements of the equivalent circuit model, as well as the S-parameter measurement errors. He defined a new concept for the minimal equivalent circuit whose elements have the lowest uncertainty. He concluded that the number of elements should be reduced if the S-parameter measurement bandwidth decreases. Moreover, if a closer tie between the circuit and the physical model should be maintained without increasing the uncertainty of the circuit parameters, some elements should be determined by other means.

Kondoh [8] developed, for the first time, an optimization algorithm to extract the 13-element GaAs MESFET equivalent circuit model from measured S-parameters. The MESFET model was extracted by a least-squares fitting of measured S-parameters to those calculated from the equivalent circuit. This algorithm solves the problem iteratively. Each iteration cycle was divided to eight consecutive optimization steps in each which only a group of selected elements in the equivalent circuit was optimized to fit a specific S-parameter over a specific frequency range. This routine involved eight error functions to be minimized as opposed to a single error function which was employed by some previous authors [16]. This algorithm took into account the difference

in standard deviations of errors in individual measured S-parameters which resulted in more modeling accuracy. However, it suffers from a local-minimum problem that the solution may be trapped in a local minimum. The sequence of steps, in each iteration, as well as the assignment of the optimized elements to the corresponding S-parameters was concluded experimentally with no analytical evidence.

Patterson et al. [18] introduced a good analysis to calculate the sensitivity of an error function, used in optimization, to each component in the model. The degree of ill-conditioning in the small-signal MESFET circuit model was formally quantified using a systematically formulated sensitivity analysis procedure. The condition number, which usually used to measure the degree of the ill-conditioning, is typically very large since the error function most often used is sensitive to changes in some combinations of model parameters but extremely insensitive to changes in other combinations. Consequently, the authors reflected this sensitivity of each optimized component to its uncertainty. They also inferred that ill-conditioning results in slow convergence of the optimization problem. The authors used the principal component sensitivity analysis to estimate for the first time how reliable optimized component values are in the final solution. They presented an optimization technique in which component transformation and scaling are carried out. This technique improves the condition number drastically and in turn results in a faster convergence rate along with higher certainty in the optimized parameters.

Niekerk and Meyer [19] applied the principal component sensitivity analysis suggested by Patterson et al. [18] to the optimization concept proposed by Kondoh [8] to extract the 13-element GaAs FET model. They defined a separate error function for each model element, giving a set of 13 error functions in contrast to 8 in Kondoh's method. The optimization order of the error function is determined by the principal component sensitivity analysis. The model parameters are optimized in this specific order starting with the most sensitive and proceeding towards the least sensitive. This method reduces the uniqueness problem that exists between the parasitic gate resistance R_g and channel resistance R_i. The authors provided a systematic and rigorous evaluation of this method in [20]. They presented a study of the convergence performance and test results. They

showed that R_g has a large influence on the extraction accuracy and demonstrated the difficulty of determining this element from only one set of measured S-parameters.

Another extension to Kondoh's method was proposed by Leong et al. [21]. They defined 10 error functions instead of 8 error functions. The order of optimization is very similar to the order of Kondoh's method except R_g and R_i are optimized separately to reduce the uniqueness problem between them. Moreover, they found that improved values of R_g and R_i could be extracted using optimization of two separate groupings of Z-parameters. They presented an optimization algorithm which combines damped Gauss-Newton method with generalized simulated annealing method. This method avoids trapping in local minima.

Chen et al. [11] extended the work of Diamond [15] to extract the full model's elements. The parasitic elements as well as the parasitic capacitances were pre-extracted from three to five sets of zero drain-to-source bias S-parameters measured at different gate bias voltages. In the second step, the S-parameters are fitted to the equivalent circuit of a MESFET in the common source, common drain, and common drain configurations to avoid local minima. The bias-independent elements -parasitic capacitances, parasitic inductances, and gate resistance- extracted from cold measurements are only kept constant during the full-bias S-parameters fitting. Otherwise, all bias independent elements are extracted. The authors applied some physical constraints to reduce the number of variables. The constraints were doping profile dependent; they were only valid for flat and Gaussian doping profiles.

Dambrine et al. [6] proposed a systematic and fast method to determine the small-signal equivalent circuit of a MESFET. This method consisted of a direct determination of all parasitic elements as well as the pad capacitances. The parasitic elements were calculated first from S-parameters measured at zero drain-to-source bias voltage with the gate forward biased. The pad capacitances were determined from S-parameters measured at zero drain-to-source bias with a gate bias voltage lower than the pinch-off voltage. The knowledge of these parasitic element values allowed determining the intrinsic small-

signal parameters after a few simple matrix manipulations to remove the parasitics from the data. This method implied some approximations so that all parameters were extracted from data at a low frequency band. Moreover, The parasitic drain and source resistances were determined from forward gate-bias data.

Berroth and Bosch [7] extended the work of Dambrine et al. [6]. They extended the small-signal model; it includes the effects of the differential resistances of the gate-to-source and gate-to-drain diodes which are significant for positively biased gate. It also includes a resistance in series with the feedback capacitance (C_{gd}). This new resistance ensures a smooth transition from the symmetric zero drain-source bias model to operating points in the saturation region. They explained a method to extract the elements of the new extended model at all bias points without frequency limitations except for the differential diode resistances which should be calculated at frequencies as low as 50MHz. Direct computation from analytical expressions has been presented. Although this method shows good agreement between the model and measured S-parameters for some positively biased gate voltages, it did not consider the bias dependence of parasitic drain and source resistances which is significant for reverse-biased gate.

Vai et al. [22] applied a simulated annealing method to the modeling optimization problem to extract models of microwave semiconductor devices in general. The using of simulated annealing method avoids entrapment in local minima of the objective function. However, authors did not apply this method to a MESFET model and did not discuss the exclusive problem associated with it.

Sledzik and Wolff [23] presented a method for the derivation of FET small and large-signal models. S-parameter measurements at three different bias voltages were employed to extract the small-signal parameters. The parasitic inductances were calculated from the imaginary parts of S-parameters at zero drain-to-source bias and forward-biased gate. The difference between drain and source parasitic resistances was calculated at the same bias condition. The parasitic resistances were calculated from the real part of S-parameters at zero drain-to-source bias and pinched-off biased gate. The difference between the drain

and source resistances was used to avoid the measurement errors and to get frequency independent source resistance. The pad capacitances were determined for a special structure device which contained the transistor metalization only. The remaining intrinsic elements were calculated from S-parameters at normal bias voltages. S-parameters were converted to Y-parameters knowing the values of parasitics and analytical equation were used to calculate all intrinsic elements.

Kompa and Schlechtweg [24] proposed an optimization algorithm to extract the model parameters. They used a single error function of S-parameters. This algorithm was applied to all bias regions: saturation, pinch-off, non-saturation and gate forward. This method is highly sensitive to any measurement errors. As a result, the authors used a highly accurate calibration method (THLR) over a wide frequency bandwidth up to 40 GHz. This accuracy may not be obtainable at any laboratory.

Kompa and Lin [25] presented a fully analytical model element extraction from "hot" S-parameter measurements. This method requires highly accurate measurement and broadband characterization techniques. The authors presented more investigation in [26]. The proposed algorithm was tested. They tried to improve the sensitivity problem that large variations of parasitic resistances do not lead to significant differences in the main intrinsic elements: C_{gs}, C_{gd}, g_{ds}, and g_m. They should that predetermination of one parasitic resistance improves the stability of extracted values and consistency of the model. They chose R_g to be predetermined because it is bias-independent.

Kompa and Novotny [27] proposed another FET model parameter extraction procedure. They showed that in order to extract a unique set of elements from hot S-parameters, the gate resistance R_g should be derived from cold S-parameters measured at gate voltages lower than the pinch-off voltage. Hence, a single error function for S-parameters was used in an optimization process to optimize all other elements.

Lin and Kompa [28] introduced a new concept for an optimization procedure applied to the FET model parameter extraction. In this technique, the elements are divided into

two sets of optimization variables. The objective function is minimized by a bidirectional search technique. The extrinsic elements comprise the first set of optimization parameters whereas the intrinsic elements comprise the second set. In each iteration, the extrinsic parameters are updated; then, the Y-parameters of the intrinsic plane are calculated which are employed to calculate the intrinsic elements by simple weighted polynomial curve fitting. An improved simplex method was used. Although this technique shows good results to avoid the local minima problem and to desensitize the extracted values to the measurement error, it depends on the starting values. Therefore, the starting values should be generated from the model at pinch-off bias. This ensures that the minimum is as close to the starting point as possible. The authors suggested the use of l_1-norm for the external objective function as it showed faster convergence.

Shirakawa et al. [29] proposed a technique to determine a HEMT equivalent circuit. Intrinsic elements are written in terms of extrinsic elements using a conventional analytical parameter transformation technique. The authors used the variance of the intrinsic elements as an optimization criterion for the first time. The extrinsic elements are the optimization parameters which are iteratively determined to minimize the variance of the intrinsic elements over a wide frequency band up to 62.5 GHz. Another optimization criterion for the discrepancy between the measured and the calculated S-parameters were considered. This method will be discussed in details along with its application to MESFET models in the next chapters.

Ooi et al. [30] applied Shirakawa's method [29] to MESFET. The intrinsic elements and one of the extrinsic elements are described as functions of the remaining extrinsic parameters. The optimization search space was reduced from 6 parameters to 5 parameters. They presented a comparison in terms of both accuracy and speed between the proposed method and some other methods on a 400 µm gate-width MESFET over 0.5-26.5 GHz frequency band. Both Shirakawa's method and Ooi's method suffers from uniqueness problem between the resistive elements of the model over limited frequency bands in the presence of the unavoidable measurement errors. This issue will be discussed in detail in the following chapters.

Martino et al. [31] modified Shirakawa's method to extract the small-signal model. They changed the error criterion to include data over a certain number of bias points. Moreover, they used simulated annealing method in conjunction with a gradient procedure to optimize the extrinsic parameters. All extrinsic parameters are assumed to be bias-independent elements.

As we have seen from the above survey, no clear technique was proposed to extract MESFET model elements accurately and consistently. Each proposed technique has some advantages and disadvantages. In the following chapters, we will deal with some techniques in details showing advantages and disadvantages of each one. Some solutions to these problems will be proposed.

Chapter 3
Extraction of Model Parameters

Several methods can be used to extract the MESFET model parameters depending on the model used and the method of characterization. In this chapter, we will discuss the parameter extraction techniques which employ only S-parameter measurements in optimization algorithms. Therefore, the formulation of the problem or the parameter relationships will be derived. The use of these relationships in an optimization technique will be addressed. We will also mention the method used to solve the optimization problem.

3.1 Model Formulation at Normal Bias Conditions:

Figure 3.1 shows the most common MESFET model at normal bias conditions, i.e. the device is biased in the saturation region. Some of those elements can be neglected in the analysis later on. The model can be divided into two sections: the extrinsic element section and the intrinsic element section. The extrinsic section includes all extrinsic elements: C_{pg}, C_{pd}, R_g, R_d, R_s, L_g, L_d, and L_s. The intrinsic section includes all the intrinsic elements: C_{gs}, R_i, C_{gd}, R_{gd}, g_m, τ, R_{ds}, and C_{ds}. The resistance R_{gd} has been added to ensure smooth transition from the symmetric cold model (V_{ds}=0) to operating points in the saturation region [7]. Although this element has little effect on the performance of the model and many authors neglect it, it was included here to present full analytical expressions.

The main concept of the extraction process, which is employed by many researchers, is to remove the extrinsic element section from the measurements to end up with Y-parameters of the intrinsic section. The Y-parameters are the most convenient parameters since the intrinsic section exhibits PI topology. The simple analytical expressions of the Y-parameters can be used to calculate the intrinsic elements.

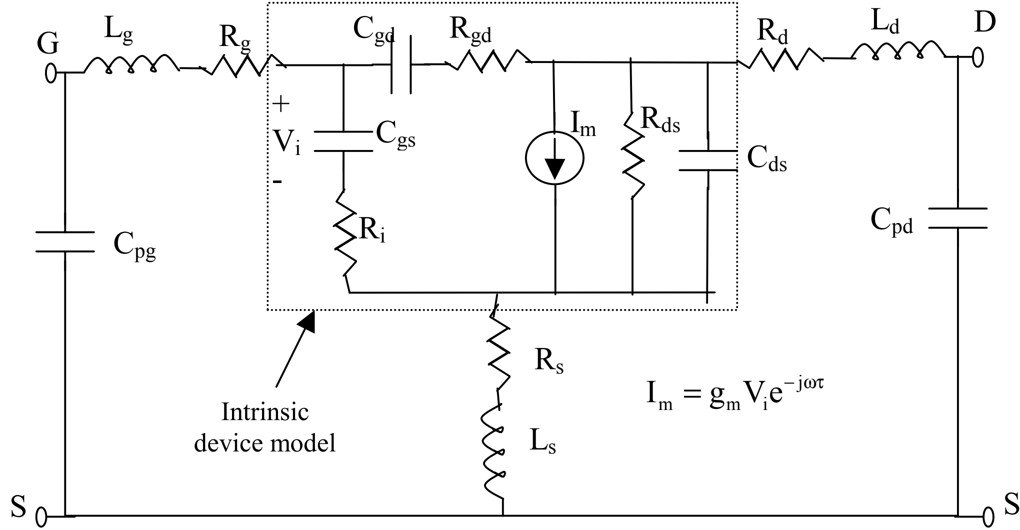

Figure 3.1 16-element small-signal MESFET model.

3.1.1 Determination of the Intrinsic Y-Parameters:

The process is depicted in Figure 3.2. We always start with the measured S-parameters of the device. S-parameters at the angular frequency (ω) are stored in the S-matrix. The S-matrix is converted to the Y-parameters matrix Y_t .

The relationship between Y-parameters and S-parameters can be written as [32]:

$$Y_{t11} = Y_o \frac{(1 - S_{11})(1 + S_{22}) + S_{12}S_{21}}{\Delta} \tag{3.1a}$$

$$Y_{t12} = Y_o \frac{-2S_{12}}{\Delta} \tag{3.1b}$$

$$Y_{t21} = Y_o \frac{-2S_{21}}{\Delta} \tag{3.1c}$$

$$Y_{t22} = Y_o \frac{(1 + S_{11})(1 - S_{22}) + S_{12}S_{21}}{\Delta} \tag{3.1d}$$

where

$$\Delta = (1 + S_{11})(1 + S_{22}) - S_{12}S_{21}$$

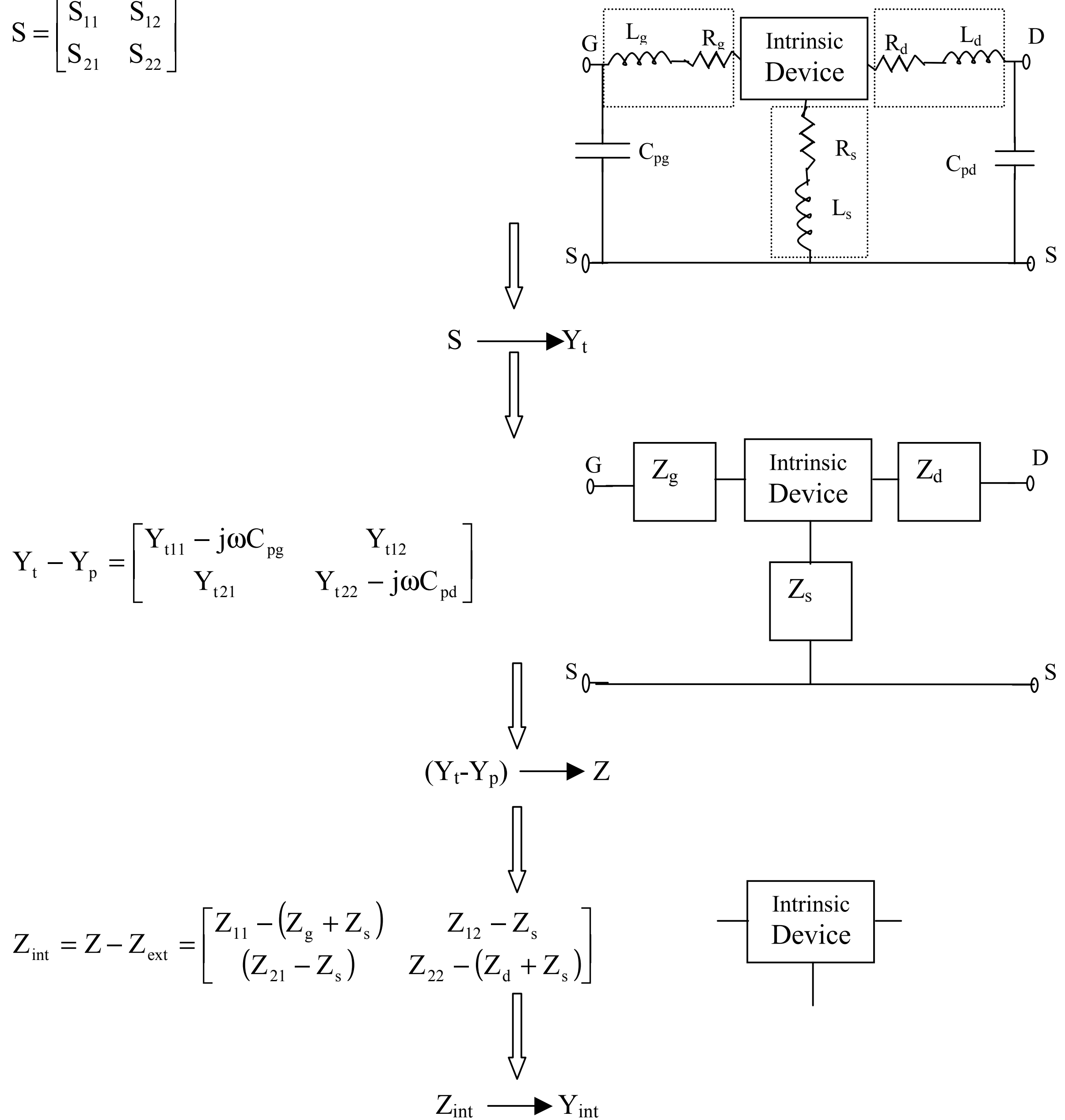

Figure 3.2 Extraction of intrinsic Y-parameters from measured S-parameters.

and $\quad Y_o = \dfrac{1}{Z_o}$

where Yo and Zo are the characteristic admittance and characteristic impedance of the measuring system, respectively. Zo is usually equal to 50 Ω. After converting S to Y_t,

the pad capacitances are subtracted from Y_t since the pad capacitances C_{pg} and C_{pd} are connected in parallel. The pad capacitances matrix Y_p can be expressed as:

$$Y_p = \begin{bmatrix} j\omega C_{pg} & 0 \\ 0 & j\omega C_{pd} \end{bmatrix} \quad (3.2)$$

The resulted Y-parameters matrix (Y_t-Y_p) is then converted into Z-parameters matrix where the Z-matrix is the inverse of the Y-matrix:

$$Z = \left(Y_t - Y_p\right)^{-1} \quad (3.3)$$

Since the parasitic resistances and inductances are connected in series with the intrinsic device, the parasitic elements matrix Z_{ext} is subtracted from Z resulting in the intrinsic Z-parameters matrix Z_{int}. Z_{ext} is the Z-parameters of the parasitic elements, which can be expressed as:

$$Z_{ext} = \begin{bmatrix} Z_g + Z_s & Z_s \\ Z_s & Z_d + Z_s \end{bmatrix} = \begin{bmatrix} \left(R_g + R_s\right) + j\omega\left(L_g + L_s\right) & R_s + j\omega L_s \\ R_s + j\omega L_s & \left(R_d + R_s\right) + j\omega\left(L_d + L_s\right) \end{bmatrix} \quad (3.4)$$

The last step in calculating Y-parameters of the intrinsic device Y_{int} is to convert Z_{int} to Y_{int}:

$$Y_{int} = Z_{int}^{-1} \quad (3.5)$$

In the mentioned process, we assumed that all the parasitic elements and pad capacitances are known either from another mathematical processes at different bias points or as optimized parameters. Equation 3.5 provides the de-embedded Y-parameters from the measured S-parameters. Y_{int} can be written in a matrix form as:

$$Y_{int} = \begin{bmatrix} Y_{i11} & Y_{i12} \\ Y_{i21} & Y_{i22} \end{bmatrix} = \begin{bmatrix} Re(Y_{i11}) + j\,Im(Y_{i11}) & Re(Y_{i12}) + j\,Im(Y_{i12}) \\ Re(Y_{i21}) + j\,Im(Y_{i21}) & Re(Y_{i22}) + j\,Im(Y_{i22}) \end{bmatrix} \tag{3.6}$$

Equation (3.6) shows the elements of Y_{int} while they are decomposed into real and imaginary parts. Real parts are denoted by "Re" whereas imaginary parts are denoted by "Im".

On the other hand, the analytical form of the Y-Parameters matrix Y_{int} can be easily derived from the intrinsic device model shown in Figure 3.1:

$$Y_{int} = \begin{bmatrix} \dfrac{\omega^2 R_i C_{gs}^2}{|D_1|^2} + \dfrac{\omega^2 R_{gd} C_{gd}^2}{|D_2|^2} + j\omega\left(\dfrac{C_{gs}}{|D_1|^2} + \dfrac{C_{gd}}{|D_2|^2}\right) & -\dfrac{\omega^2 R_{gd} C_{gd}^2}{|D_2|^2} - j\omega\dfrac{C_{gd}}{|D_2|^2} \\ \dfrac{g_m e^{-j\omega\tau}}{D_1} - j\dfrac{\omega C_{gd}}{D_2} & g_{ds} + \dfrac{\omega^2 R_{gd} C_{gd}^2}{|D_2|^2} + j\omega\left(C_{ds} + \dfrac{C_{gd}}{|D_2|^2}\right) \end{bmatrix} \tag{3.7}$$

where,

$$D_1 = 1 + j\omega R_i C_{gs}$$

$$D_2 = 1 + j\omega R_{gd} C_{gd}$$

For more details on the derivation of Y_{int}, the reader is encouraged to refer to Appendix A. Equation (3.7) can be further simplified if R_{gd} is assumed to be equal to zero. This assumption has been used by many authors and it makes sense because R_{gd} has been added for the purpose of symmetry with R_i. R_i itself has no specific physical meaning and it is added in the model to account for the real part of Y_{int11}. The simplified form of equation (3.7), while R_{gd}=0, can be written as:

$$Y_{int} = \begin{bmatrix} \frac{\omega^2 R_i C_{gs}^2}{|D_1|^2} + j\omega\left(\frac{C_{gs}}{|D_1|^2} + C_{gd}\right) & -j\omega C_{gd} \\ \frac{g_m e^{-j\omega\tau}}{D_1} - j\omega C_{gd} & g_{ds} + j\omega(C_{ds} + C_{gd}) \end{bmatrix} \quad (3.8)$$

where

$$D_1 = 1 + j\omega R_i C_{gs}$$

Equation (3.8) is most commonly used more than equation (3.7). In the next section, we will derive the intrinsic elements in terms of intrinsic Y-parameters by using both equations (3.7) and (3.8).

3.1.2 Intrinsic Parameters in Terms of Intrinsic Y-Parameters:

All intrinsic parameters can be extracted at each frequency point in terms of Y_{int} data mentioned in equation (3.6). Equating equation (3.6) with equation (3.7) and solving for the intrinsic parameters, refer to Appendix A for more details, the intrinsic parameters can be stated as:

$$C_{gs} = \frac{(1 + d_1^2)}{\omega}(Im(Y_{i11}) + Im(Y_{i12})) \quad (3.9a)$$

$$R_i = \frac{d_1}{(1 + d_1^2)(Im(Y_{i11}) + Im(Y_{i12}))} \quad (3.9b)$$

$$C_{gd} = -\frac{Im(Y_{i12})}{\omega}(1 + d_2^2) \quad (3.9c)$$

$$R_{gd} = -\frac{d_2}{(1 + d_2^2)Im(Y_{i12})} \quad (3.9d)$$

$$g_m = |G| \quad (3.9e)$$

$$\tau = -\frac{1}{\omega}\angle(G) \quad (3.9f)$$

$$g_{ds} = Re(Y_{i22}) + Re(Y_{i12}) \quad (3.9g)$$

$$C_{ds} = \frac{Im(Y_{i22}) + Im(Y_{i12})}{\omega} \tag{3.9h}$$

where

$$d_1 = \frac{Re(Y_{i11}) + Re(Y_{i12})}{Im(Y_{i11}) + Im(Y_{i12})}$$

$$d_2 = \frac{Re(Y_{i12})}{Im(Y_{i12})}$$

$$G = g_m e^{-j\omega\tau} = \left(Y_{i21} - Y_{i12}\right)\left(1 + jd_1\right)$$

$$= \sqrt{\left(\left(Re(Y_{i21}) - Re(Y_{i12})\right)^2 + \left(Im(Y_{i21}) - Im(Y_{i12})\right)^2\right)\left(1 + d_1^2\right)}$$

$$\angle \tan^{-1}\left(\frac{d\left(Re(Y_{i21}) - Re(Y_{i12})\right) + \left(Im(Y_{i21}) - Im(Y_{i12})\right)}{\left(Re(Y_{i21}) - Re(Y_{i12})\right) - d\left(Im(Y_{i21}) - Im(Y_{i12})\right)}\right)$$

Similarly, equation (3.6) can be equated with equation (3.8) and solved together for the intrinsic parameters. Alternatively, this solution can be derived from equation (3.9) by substituting $Re(Y_{i12})=0$; this is obvious from equation (3.8) that $Re(Y_{i12})$ must be equal to zero if R_{gd} is equal to zero. The new solution in this case can be written as:

$$C_{gs} = \frac{\left(1 + d^2\right)}{\omega}\left(Im(Y_{i11}) + Im(Y_{i12})\right) \tag{3.10a}$$

$$R_i = \frac{d}{\left(1 + d^2\right)\left(Im(Y_{i11}) + Im(Y_{i12})\right)} \tag{3.10b}$$

$$C_{gd} = -\frac{Im(Y_{i12})}{\omega} \tag{3.10c}$$

$$g_m = \left|G\right| \tag{3.10d}$$

$$\tau = -\frac{1}{\omega}\angle\left(G\right) \tag{3.10e}$$

$$g_{ds} = Re(Y_{i22}) \tag{3.10f}$$

$$C_{ds} = \frac{Im(Y_{i22}) + Im(Y_{i12})}{\omega} \tag{3.10g}$$

where

$$d = \frac{\mathrm{Re}(Y_{i11})}{\mathrm{Im}(Y_{i11}) + \mathrm{Im}(Y_{i12})}$$

$$G = g_m e^{-j\omega\tau} = (Y_{i21} - Y_{i12})(1 + jd)$$

$$= \sqrt{\left((\mathrm{Re}(Y_{i21}))^2 + (\mathrm{Im}(Y_{i21}) - \mathrm{Im}(Y_{i12}))^2\right)(1 + d^2)} \angle \tan^{-1}\left(\frac{d\,\mathrm{Re}(Y_{i21}) + (\mathrm{Im}(Y_{i21}) - \mathrm{Im}(Y_{i12}))}{\mathrm{Re}(Y_{i21}) - d(\mathrm{Im}(Y_{i21}) - \mathrm{Im}(Y_{i12}))}\right)$$

Equations (3.10) will be used later on in the optimization process to extract the values of the intrinsic parameters at normal bias conditions.

3.2 A Simplified Model of the MESFET at Pinch-off Voltage:

In this section, we will provide a much simpler analysis of a GaAs MESFET model at a gate-source bias voltage less than or equal to the pinch-off voltage of the device with zero drain-source bias voltage. The model itself is much simpler and seems to be highly symmetric; consequently, the associated analysis is much easier. At pinch-off voltages, the channel is closed and therefore it exhibits high resistance between the drain and the source. As a result, the dominant component between the drain and the source is C_{ds}. There is no current flowing from drain to source and g_m should be equal to zero. At pinch-off voltages, both gate-source and gate-drain junctions are deeply reverse biased; in turn C_{gs} and C_{gd} would be too small. Therefore, both R_i and R_{gd} can be neglected. Figure 3.3 shows the simplified model of a GaAs MESFET at pinch-off voltage with V_{ds}=0.

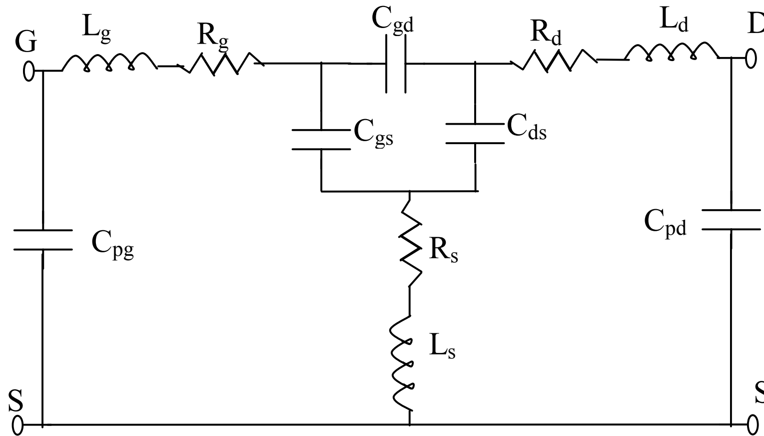

Figure 3.3 A simplified model of a MESFET at pinch-off voltage with V_{ds}=0.

Moreover, as V_{ds}=0, the device structure is symmetric and therefore C_{gs} should be equal to C_{gd}. This assumption will be used later on to calculate some extrinsic elements. This simple model of the MESFET device at pinch-off voltage is usually used to calculate the pad capacitances C_{pg} and C_{pd} as well as the gate resistance R_g, and parasitic inductances L_d, and L_s. Two approaches should be discussed at this point. The first approach is concerned with the determination of the pad capacitances only whereas the second approach is concerned with the determination of the pad capacitances in addition to the gate parasitic elements.

3.2.1 Determination of Pad Capacitances:

At zero drain-source bias, and for a gate voltage lower than the pinch-off voltage, the intrinsic capacitance under the gate cancels out. Hence, the gate-source and gate-drain capacitances are dominated by the fringing capacitances attributed to the extension of the depleted layer at each side of the gate [6]. As a result, both capacitances should be equal:

$$C_{gs} = C_{gd} = C_f \tag{3.11}$$

where C_f is an arbitrary parameter representing the fringing capacitances. Moreover, all parasitic resistances and capacitances have no influence on the imaginary part of the Y-parameters up to a few gigahertz (e.g. 5GHz) since all the capacitances of the model are too small. As a result, one can remove the parasitic resistances and inductances from the model as a rational approximation. The reduced model in this case is shown in Figure 3.4.

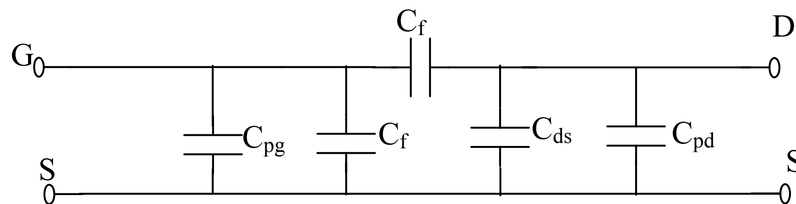

Figure 3.4 A reduced model at gate voltage equal to or lower than the pinch-off voltage.

The analytical equations of the Y-parameters are very easy to be determined from the equivalent circuit in Figure 3.4:

$$Y = \begin{bmatrix} j\omega(C_{pg} + 2C_f) & -j\omega C_f \\ -j\omega C_f & j\omega(C_f + C_{ds} + C_{pd}) \end{bmatrix} \quad (3.12)$$

It is obvious that all imaginary parts of Y-parameters are linearly proportional to the frequency. This fact has been confirmed in the next chapter to assure the validity of the aforementioned approximation. One may also notice that we have three independent equations with three unknowns: C_{pg}, C_f and sum of (C_{ds} and C_{pd}). Unfortunately, this approach is not able to distinguish between C_{ds} and C_{pd}. Dambrine et al. [6] neglected C_{ds} although our results show significant values for C_{ds} at this gate bias voltage. The algorithm to calculate C_{pg}, C_f and (C_{ds}+C_{pd}) can be described as follows:

1- Measured S-parameters should be converted to Y-parameters using equations (3.1).

2- The imaginary parts of Y-parameters are linearly fitted to a first order polynomial of ω -see Appendix B for more information about curve fitting-. The Imaginary parts of Y-parameters can be written in terms of the fitting coefficients as:

$$\mathrm{Im}(Y_{11}) = a_{11}\omega \quad (3.13a)$$

$$\mathrm{Im}(Y_{12}) = a_{12}\omega \quad (3.13b)$$

$$\mathrm{Im}(Y_{21}) = a_{21}\omega \quad (3.13c)$$

$$\mathrm{Im}(Y_{22}) = a_{22}\omega \quad (3.13d)$$

3- C_f can be calculated from either $\mathrm{Im}(Y_{12})$ or $\mathrm{Im}(Y_{21})$, however, we will assume its value as the average of both of them so that all parts are taken into consideration for reasonable balance between the different parameters:

$$C_b = -\frac{a_{12} + a_{21}}{2} \quad (3.14a)$$

$$C_{pg} = a_{11} - 2C_b \quad (3.14b)$$

$$C_{ds} + C_{pd} = a_{22} - C_b \quad (3.14c)$$

3.2.2 Lin's Method for Determining the Parasitic Elements and Pad Capacitances:

A method was first proposed by Lin et. al. [28] to calculate the parasitic resistances and inductances in addition to the pad capacitances from the measured data at pinch-off voltage (V_{ds}=0 and V_{gs}<-$|V_p|$). The method was mainly devised to determine initial values for the parasitics to be used in an optimization procedure at the original bias point of interest. However, it provides reasonable values for all parasitics provided that the frequency band is wide (e.g. 1 GHz- 40 GHz). The effect of the frequency band of measurements on the solution will be discussed in the next chapter. If the frequency band is rather smaller, we will propose a modified method explained in the next section.

The method uses C_{pg} and C_{pd} as optimization variables while other parameters in the model should be calculated by curve fitting at each optimization step. The intrinsic model consisting of the capacitors C_{gs}, C_{gd}, and C_{ds} are arranged in a π-topology as shown in Figure 3.3. The π-topology is transformed into a T-topology because the T-topology is more convenient in the optimization procedure and curve fitting process than π-topology. The new model after transformation is shown in Figure 3.5. The relationships between the π-topology elements and the T-topology elements can be written as:

$$C_g = C_{gd} + C_{gs} + \frac{C_{gd} C_{gs}}{C_{ds}} \quad (3.15a)$$

$$C_d = C_{gd} + C_{ds} + \frac{C_{gd} C_{ds}}{C_{gs}} \quad (3.15b)$$

$$C_s = C_{gs} + C_{ds} + \frac{C_{gs}C_{ds}}{C_{gd}} \tag{3.15c}$$

As shown in Figure3.5, the circuit is composed of two sub-circuits: the internal circuit consisting of Z_{gp}, Z_{dp}, and Z_{sp} connected in a T-Structure and the external circuit consisting of the parasitic capacitances C_{pg} and C_{pd}. The optimization procedure can be described as follows:

1- Measured S-parameters should be converted to Y-parameters using equations (3.1). Y-parameters are identified by the matrix Y_t.

2- Zero initial values for C_{pg} and C_{pd} should be assumed. Any set of initial values can be assumed, since the objective function does not exhibit any local minimum, as it will be shown in the next chapter.

3- The internal circuit Y-parameters should be de-embedded from Y_t by subtracting the Y-parameters of the pad capacitances:

$$Y_{internal} = Y_t - Y_p = Y_t - \begin{bmatrix} j\omega C_{pg} & 0 \\ 0 & j\omega C_{pd} \end{bmatrix} \tag{3.16}$$

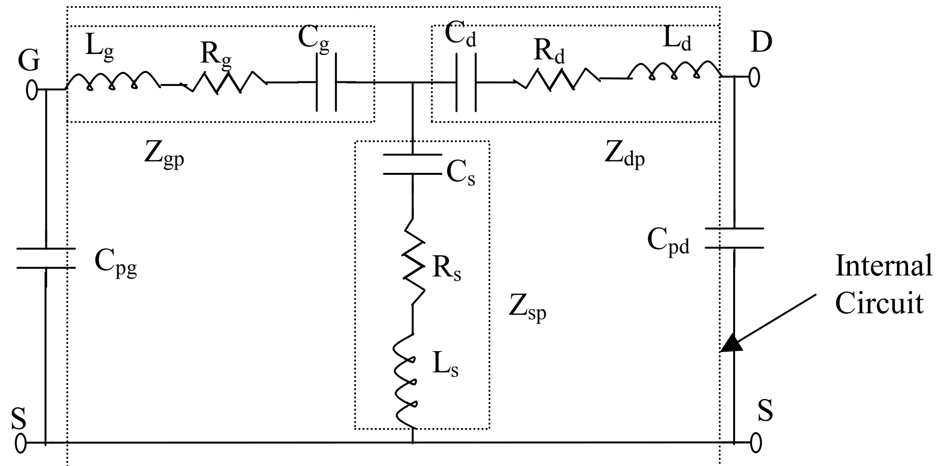

Figure 3.5 The pinch-off model in a T-topology

4- The internal circuit Y-parameters $Y_{internal}$ should be converted to the corresponding Z-parameters $Z_{internal}$:

$$Z_{internal} = Y_{internal}^{-1} \tag{3.17}$$

5- While $Z_{internal}$ in equation (3.17) is the internal Z-parameters extracted from the measured data, the analytical form of $Z_{internal}$ can be determined from Figure 3.5:

$$Z_{internal} = \begin{bmatrix} Z_{gp} + Z_{sp} & Z_{sp} \\ Z_{sp} & Z_{dp} + Z_{sp} \end{bmatrix} \tag{3.18}$$

where,

$$Z_{gp} = R_g + j(\omega L_g - \omega C_g)$$

$$Z_{dp} = R_d + j(\omega L_d - \omega C_d)$$

$$Z_{sp} = R_s + j(\omega L_s - \omega C_s)$$

6- From $Z_{internal}$ data, equation (3.17), and analytical form of $Z_{internal}$, equation (3.18), all branch impedances Z_{gp}, Z_{dp} and Z_{sp} can be determined:

$$Z_{sp} = \frac{Z_{internal12} + Z_{internal21}}{2} \tag{3.19a}$$

$$Z_{gp} = Z_{internal11} - Z_{sp} \tag{3.19b}$$

$$Z_{dp} = Z_{internal22} - Z_{sp} \tag{3.19c}$$

7- All resistances, inductances, and capacitances can be calculated by applying a frequency-weighted curve-fitting procedure [28], mentioned in Appendix B. The resistance, inductance, and capacitance values can be summarized as:

$$R_j = Z_o \frac{x_2}{x_1} \tag{3.20a}$$

$$L_j = \frac{Z_o}{\omega_o}\frac{x_3}{x_1} \tag{3.20b}$$

$$C_j = \frac{x_1}{\omega_o Z_o} \tag{3.20c}$$

where x_1, x_2, and x_3 are intermediate variables defined in Appendix B, j is equal to (g, d, or s), and ω_o is a normalization angular frequency which is equal to the maximum angular frequency.

8- Knowing all circuit elements, the S-parameters of the model S_c should be computed. Computation of S_c goes through backward steps to the above steps: internal Z-parameters should be calculated using equation (3.18), and then it is transformed into internal Y-parameters. Internal Y-parameters is then added to Y_p to form the computed overall Y-parameters Y_{tc}. Y_{tc} should then be converted to S_c:

$$S_{c11} = \frac{(Y_o - Y_{tc11})(Y_o + Y_{tc22}) + Y_{t12}Y_{t21}}{\Delta Y} \tag{3.21a}$$

$$S_{c12} = \frac{-2Y_{t12}Y_o}{\Delta Y} \tag{3.21b}$$

$$S_{c21} = \frac{-2Y_{t21}Y_o}{\Delta Y} \tag{3.21c}$$

$$S_{c22} = \frac{(Y_o + Y_{tc11})(Y_o - Y_{tc22}) + Y_{t12}Y_{t21}}{\Delta Y} \tag{3.21d}$$

where,

$$\Delta Y = (Y_o + Y_{tc11})(Y_o + Y_{tc22}) - Y_{t12}Y_{t21}$$

9- The objective function (the error function) should be estimated to find its minimum. If the values of C_{pg} and C_{pd} do not result in the minimum of the objective function, the values of C_{pg} and C_{pd} should be updated using an optimization algorithm and steps 3 through 9 should be repeated. Otherwise, the values of C_{pg} and C_{pd} are the optimum

values. Lin et al. [28] adopted simplex optimization method. Moreover, the objective function is an important issue which should be investigated carefully. The proposed objective function is l_2-norm of the difference between the measured and the calculated S-parameters. The objective function ε can be written in the following form:

$$\varepsilon = \sum_{p=1}^{2}\sum_{q=1}^{2}\sum_{i=1}^{N}\left(\frac{\left|S_{pq}(\omega_i) - S_{cpq}(\omega_i)\right|}{\left|S_{pq}\right|_{max}}\right)^2 \tag{3.22}$$

where N is the number of measurements at different frequency points, $\left|S_{pq}\right|_{max}$ is largest magnitude of the measured S-parameter S_{pq} over the frequency band, S_{pq} and S_{cpq} are the measured and calculated S-parameters, respectively.

Lin et al. proved that their method worked over wide frequency bands (1 GHz-40 GHz). It is important to work over such wide frequency band so that all resistance and inductance values become reasonable with respect to the capacitance values in the model. Our Intensive computer work has been done which proved that this method was not suitable in its original form to extract accurate results over smaller frequency bands (0.2-12.2 GHz). The results are shown in the next chapter. In the next section, we will propose a modified method to overcome this limitation.

3.2.3 A Modified Method for Determining the Pad Capacitances and Gate Parasitic Elements:

We have modified Lin's method to determine accurate values for the gate parasitic elements and the pad capacitances. These elements are bias-independent elements which will be used in next algorithms towards the extraction of the full-model parameters. What urged us to look for an alternative method is the essence need to estimate accurate values for the pad capacitances and the gate resistance R_g so that all other parameters in Figure

3.1 can be determined. The importance of estimating the pad capacitances and the gate resistance will be discussed in section 4.3.

The intensive computer work proved that Lin's method failed over limited frequency bands because the capacitive impedances were much larger than the inductive impedances where both of them were added up to form the imaginary parts of the branch impedances. As a result, the unavoidable measurement errors made the discrimination between the capacitive values and inductive values almost impossible unless the measurement data was noiseless. Consequently, we found out that one inductance value at least must be determined before running the optimizer. The inductance values are determined using the measured data at V_{ds}=0 and V_{gs}=0. The measurements under zero drain-source voltage are called "Cold Measurements". It will be explained in detail in the next section.

Our proposed method has two attractive features: it works over any frequency band and it is significantly insensitive to measurement noise. It is different from Lin's method in two main regards: Ld and Ls are assumed to be fixed at their estimated values from the cold-measurements and both C_{gs} and C_{gd} are assumed to be equal. The second assumption, that C_{gs} is equal to C_{gd}, is based on the same justification described in section 3.2.1 and formulated in equation (3.11). The algorithm, and consequently, the objective function are also modified to speed up the convergence. The algorithm is more consistent with the algorithm described in section 3.5.2 to estimate the parameters of the normal bias model.

Our modified method implies the use of C_{pg}, C_{pd}, and L_g as optimization parameters. Since L_d and L_s are known, the unknown internal parameters are reduced to R_g, R_d, R_s, C_g, C_d, and C_s. We can explain our method through out the next steps:

1- Both inductances L_d, and L_s should be determined from cold-measurements. Measured S-parameters should also be converted into Y-parameters (Y_t) using equations (3.1).

2- Zero initial values might be assigned to the optimization variables C_{pg}, C_{pd}, and L_g. One might notice that the initial values might be different because this procedure has to be incorporated into an iterative scheme with cold-measurements extraction procedure. This scheme will be described in detail in section 3.5.1 to take into account the effect of pad capacitances on the cold-measurements extraction process.

3- The pad capacitance matrix Y_p is subtracted from Y_t to give the internal Y-parameters matrix $Y_{internal}$ using equation (3.16).

4- The Z-parameters ($Z_{internal}$) of the internal circuit is calculated using equation (3.17) from which all the branch impedances can be calculated as shown in equations (3.19a) through (3.19c).

5- We are ready now to calculate all unknown internal circuit elements R_g, R_d, R_s, C_g, C_d, and C_s. The relationships between the internal circuit elements and the branch impedances are shown in equation (3.18) and will be rewritten here for convenience:

$$Z_{gp} = R_g + j(\omega L_g - \omega C_g) \tag{3.23a}$$

$$Z_{dp} = R_d + j(\omega L_d - \omega C_d) \tag{3.23b}$$

$$Z_{sp} = R_s + j(\omega L_s - \omega C_s) \tag{3.23c}$$

Handling the real and imaginary parts of the branch impedances and rearranging them in the equations (3.23a) through (3.23c), the elements R_g, R_d, R_s, C_g, C_d, and C_s can be estimated as:

$$R_g(\omega_i, C_{pg}, C_{pd}, L_g) = \mathrm{Re}(Z_{gp}) \tag{3.24a}$$

$$R_d(\omega_i, C_{pg}, C_{pd}, L_g) = \mathrm{Re}(Z_{dp}) \tag{3.24b}$$

$$R_s(\omega_i, C_{pg}, C_{pd}, L_g) = \mathrm{Re}(Z_{sp}) \tag{3.24c}$$

$$C_g(\omega_i, C_{pg}, C_{pd}, L_g) = \frac{1}{\omega_i(\omega_i L_g - \mathrm{Im}(Z_{gp}))} \tag{3.24d}$$

$$C_d(\omega_i, C_{pg}, C_{pd}, L_g) = \frac{1}{\omega_i(\omega_i L_d - \mathrm{Im}(Z_{dp}))} \tag{3.24e}$$

$$C_s(\omega_i, C_{pg}, C_{pd}, L_g) = \frac{1}{\omega_i(\omega_i L_s - \mathrm{Im}(Z_{sp}))} \tag{3.24f}$$

All elements of equations (3.24a) through (3.24f) are functions of the frequency and optimization parameters. The elements should be calculated at every frequency point "i".

6- The elements of equations (3.24) should be independent on the frequency. In other words, these elements should exhibit flat functions of frequency. The variances of the dominant elements are chosen to express one criterion of the objective function. These variances should be as small as possible. The dominant elements of pinch-off circuit model are the capacitive elements. We exclude the resistive elements' variances from the objective function because the resistances of the circuit model are much less than the capacitive reactances. Computational investigation proves that including variances of the resistive elements might lead to wrong and nonsense parameters. Values of the resistances are calculated as averages of the values of equations (3.24a) through (3.24c) over the upper half of the frequency range.

In order to ease the objective function formulation, we need to define the capacitive elements as:

$$C_g(\omega_i, C_{pg}, C_{pd}, L_g) = fp_{1i}(\omega_i, C_{pg}, C_{pd}, L_g) \tag{3.25a}$$

$$C_d(\omega_i, C_{pg}, C_{pd}, L_g) = fp_{2i}(\omega_i, C_{pg}, C_{pd}, L_g) \tag{3.25b}$$

$$C_s(\omega_i, C_{pg}, C_{pd}, L_g) = fp_{3i}(\omega_i, C_{pg}, C_{pd}, L_g) \tag{3.25c}$$

Where "i" is the frequency point, which varies from 0 to N-1. The variance error criterion can be written as:

$$\varepsilon_1^k\left(C_{pg}, C_{pd}, L_g\right) = W\frac{1}{N}\sum_{i=N/2}^{i=N-1}\left|\rho_k\left(fp_{ki} - \overline{fp}_k\right)\right|^2 \tag{3.26}$$

where,

$$\bar{fp}_k = \frac{2}{N}\sum_{i=N/2}^{i=N-1} fp_{ki}$$

$\bar{fp}_k$ is the mean value of fp_k and k varies from 1 to 3. W is a weighting factor which is fixed at 100. ρ_k is a normalizing factor designated to maintain all errors at different k's within the same order of magnitudes regardless of the element value. It also increases the error if fp_{ki} gets a negative value. ρ_k can be described as follows:

Assuming: $\max fp_k = \max_i(fp_{ki})$ where i varies from N/2 to N-1

and $\min fp_k = \min_i(fp_{ki})$, where i varies from N/2 to N-1

If $\max fp_k >= |\min fp_k|$, then $\rho_k = \dfrac{1}{\max fp_k}$

Else if $\min fp_k >= -1$, then $\rho_k = \dfrac{1}{|\min fp_k|}$

Otherwise $\rho_k = 1$. (3.27)

One might have noticed that all calculations are done over the upper half of the frequency range only. The reason is, although the resistance between the drain and the source R_{ds} is very big at pinch-off bias voltage, this value may be comparable to the capacitive reactance of C_{ds} at low frequency points. Moreover, if the bias point is not fairly below the pinch-off voltage, which is our case as shown in the next chapter, then there is some possibility to have significant value for R_{ds}. Hence, it is recommended to avoid the low frequency points to assure good matching between the physical device and the model shown in Figure 3.3.

The second error criterion of the objective function is the l_2-norm of the discrepancy between the measured and the calculated S-parameters, which is very similar to Lin's objective function, equation (3.22). This error criterion is important to guarantee good matching between the measured and the calculated S-parameters. The S-parameters

can be computed in backward as explained in step #8 of Lin's method in section 3.2.2. The S-parameters error criterion can be stated as:

$$\varepsilon_2\left(C_{pg}, C_{pd}, L_g\right) = \sum_{p=1}^{2}\sum_{q=1}^{2}\sum_{i=N/2}^{N-1} W_{pq}\left(\frac{\left|S_{pq}(\omega_i) - S_{cpq}(\omega_i)\right|}{G_{pq}}\right)^2 \tag{3.28}$$

where,

$G_{11} = G_{22} = \max_i(|S_{11}(\omega_i)|)$ where i varies from N/2 to N

$G_{21} = G_{12} = \max_i(|S_{21}(\omega_i)|)$ where i varies from N/2 to N

The weighing factor W_{pq} is fixed at 0.5. The upper half of the frequency range is only used for the aforementioned reason. The normalization factor G_{pq} for the reflection parameters S_{11} and S_{22} is equal to the largest magnitude of the measured S-parameter S_{11} over the upper half of the frequency band. G_{pq} for the transmission parameters S_{21} and S_{12} is equal to the largest magnitude of the measured S-parameter S_{21} over the upper half of the frequency band. The normalization factor of S_{22} is equated to the normalization factor of S_{11} since the measurements, as will be shown in the next chapter, show that S_{22} is noisier than S_{11} at most bias points. In addition, the magnitude of S_{22} is usually smaller than the magnitude of S_{11}. For these reasons, G_{22} is set to be equal to G_{11} to inhibit the effect of the noise of S_{22} on the optimization process. Similarly, G_{12} is set to be equal to G_{21}.

The objective function is composed of ε_1 and ε_2 as follows:

$$\varepsilon\left(C_{pg}, C_{pd}, L_g\right) = \sum_k \varepsilon_1^k + \varepsilon_2 \tag{3.29}$$

7- The objective function of equation (3.29) is estimated to locate the minimum point of this function. An optimization algorithm should be employed. Levenberg-Marquardt optimization algorithm, which is described in section 3.7.2, is proven to work well.

This method has shown good results with acceptable accuracy for all pad capacitances and gate parasitic elements. It will be used in our full-proposed procedure mentioned in section 3.5 to calculate all parameters of the model at normal bias points.

3.3 Determination of Parasitic Inductances from Cold-Measurements:

As we have seen in the previous section, we have to determine inductance values to be able to calculate the gate parasitic elements and pad capacitances. The inductance values can be extracted from what are called S-parameter Cold-Measurements. As you can guess from its names, S-parameters should be measured while the dissipated power is almost zero at V_{ds}=0. Diamond et al. [15] proposed a method to extract parasitic inductances and resistances under zero drain-source voltage. Although their method may be applicable for the determination of both parasitic resistances and inductances, we will apply this method to determine parasitic inductances only. The reason is that the determination of parasitic resistances requires more measurements under different V_{gs} values and it is applicable only for a flat doping profile. Figure 3.6 shows a MESFET model under zero drain-source voltage while the gate-source voltage is fairly above the pinch-off voltage of the device.

Under this bias condition, the region under the gate can be represented by a distributed, uniform, RC transmission line. The total capacitance of the depletion layer under the gate is C_c while the total channel resistance is R_c. C_{gs} and C_{gd} represent the fringing capacitance due to the extension of the depleted layer between the gate and source at one side, and the gate and drain at the other side. C_{ds} is the inter-electrode capacitance between the drain and source. Both pad capacitances C_{pg} and C_{pd} can be neglected as first order approximation because the intrinsic capacitive impedance is not as big as that of pinch-off gate bias. Therefore, C_{pd} and C_{pg} should be much less than all intrinsic capacitances C_{gs}, C_{gd} C_{ds} and C_c. Nevertheless, C_{pg} and C_{pd} can be included; and their values can be calculated by applying the procedure mentioned in section 3.2.3. In this case, the process discussed in this section to calculate inductance values may be combined in an iterative process with the procedure mentioned in section 3.2.3, this iterative scheme will be used in section 3.5.1. Thus, parasitics and pad capacitances can be calculated simultaneously.

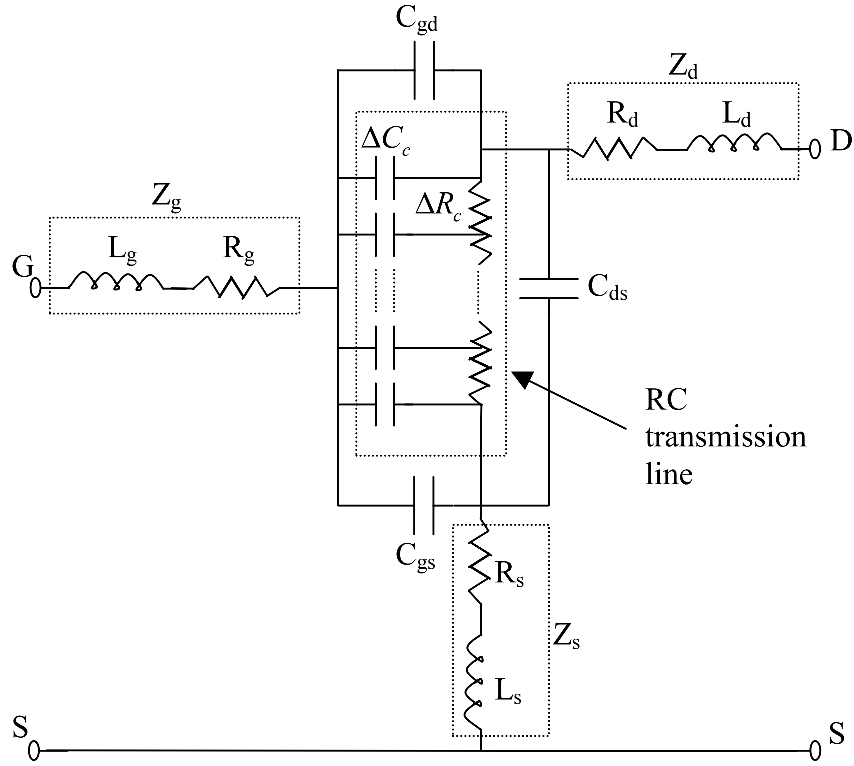

Figure 3.6 A MESFET model for V_{ds}=0 and V_{gs} fairly above pinch off voltage.

However, we prefer to neglect pad capacitances throughout our procedure in this section to ease it. Moreover, we will see that this approximation has no effect on the frequency dependence of Z-parameters specially Z_{12}, Z_{21}, and Z_{22}. We start our analysis with Z-parameters of the region under the gate; refer to Appendix C for derivation. Z-parameters can be calculated from a conventional transmission line Z-parameters with some mathematical manipulation. Z-parameters of this region can be written as:

$$Z_c = \begin{bmatrix} \dfrac{\gamma L}{j\omega C_c \tanh(\gamma L)} & \dfrac{\gamma L(\cosh(\gamma L)-1)}{j\omega C_c \sinh(\gamma L)} \\ \dfrac{\gamma L(\cosh(\gamma L)-1)}{j\omega C_c \sinh(\gamma L)} & \dfrac{2\gamma L(\cosh(\gamma L)-1)}{j\omega C_c \sinh(\gamma L)} \end{bmatrix} \tag{3.30}$$

where γ is the propagation constant of the RC transmission line and L is the gate length,

$$\gamma L = \sqrt{j\omega C_c R_c} \tag{3.31}$$

Equation 3.30 can be simplified if the electrical length of the transmission line is short,

$$\left|(\gamma L)^2\right| = \omega C_c R_c << 1 \tag{3.32}$$

This assumption can be satisfied under two conditions: a channel opening higher than 20% of the total channel height and low frequency band. The former condition is important so that R_c is reasonably small. This condition is already satisfied because gate is always biased, through out our research, at V_{gs}=0. The latter condition is met for frequencies up to about 10 GHz. Therefore, a sub-frequency band of the measurements should be exploited so that the maximum frequency of the sub-band is 10 GHz. If the assumption (3.32) is valid, equation (3.30) can be reduced to:

$$Z_c = \begin{bmatrix} \frac{1}{3}R_c - j\frac{1}{\omega C_c} & \frac{1}{2}R_c \\ \frac{1}{2}R_c & R_c \end{bmatrix} \tag{3.33}$$

C_{gs}, C_{gd}, and C_{ds} can be added to Z_c to determine the intrinsic Z-parameters (Z_{int}). Another assumption should be met to simplify the expressions:

$$\omega R_c C_x << 1 \tag{3.34}$$

where (x= C_{gs}, C_{gd}, or C_{ds}). The condition (3.34) is implicitly met if the condition (3.32) is satisfied since C_c should be larger than C_x. Z_{int} can be approximated as:

$$Z_{int} = \begin{bmatrix} \frac{1}{3}\frac{C_c^2 + 3C_{gd}^2 + 3C_{gd}C_c}{\left(C_c + C_{gs} + C_{gd}\right)^2} R_c - j\frac{1}{\omega\left(C_c + C_{gs} + C_{gd}\right)} & \frac{1}{2}\frac{C_c + 2C_{gd}}{C_c + C_{gs} + C_{gd}} R_c \\ \frac{1}{2}\frac{C_c + 2C_{gd}}{C_c + C_{gs} + C_{gd}} R_c & R_c \end{bmatrix} \quad (3.35)$$

The simplified equation (3.35) has been confirmed using the symbolic analysis toolbox of MATLAB. The parameters of Z_{int} in equation (3.35) have been approximated with respect to Z_{ext} of equation (3.4) to be added to estimate the overall Z-parameters as:

$$Z = \begin{bmatrix} R_g + R_s + \frac{1}{3}\frac{C_c + 3C_{ds} + 3C_{gd}}{C_c + C_{gs} + C_{gd}} R_c + j\left(\omega\left(L_g + L_s\right) - \frac{1}{\omega\left(C_c + C_{gs} + C_{gd}\right)}\right) & R_s + \frac{1}{2}\frac{C_c + 2C_{gd}}{C_c + C_{gs} + C_{gd}} R_c + j\omega L_s \\ R_s + \frac{1}{2}\frac{C_c + 2C_{gd}}{C_c + C_{gs} + C_{gd}} R_c + j\omega L_s & R_d + R_s + R_c + j\omega\left(L_d + L_s\right) \end{bmatrix}$$

(3.36)

The real parts of Z can be used to calculate R_c where a relationship between R_c as a function of V_{gs} should be assumed. In this case, the real parts of Z should be drawn as a function of V_{gs} from which R_c can be calculated. Moreover, all intrinsic resistances can be also calculated using the real parts of Z. We will not go deeply discussing how these resistances can be calculated since this issue is out of our focus. We will focus into calculation of the intrinsic inductances.

Looking at the imaginary parts of the Z elements, we can easily notice that all inductances L_g, L_d, and L_s can be calculated from the imaginary parts. $Im(Z_{12})$, $Im(Z_{21})$, and $Im(Z_{22})$ are linearly proportional with ω. $Im(Z_{11})$ is simply the imaginary part of an impedance of a series LC resonance circuit. Thus, all inductances can be calculated by fitting such relations to imaginary parts of Z-parameters data. Again, we always start with S-parameter measurements. Consequently, the first step is to convert S-parameters into Z-parameters [32]:

$$Z_{11} = Z_o \frac{(1+S_{11})(1-S_{22})+S_{12}S_{21}}{\Delta} \tag{3.37a}$$

$$Z_{12} = Z_o \frac{2S_{12}}{\Delta} \tag{3.37b}$$

$$Z_{21} = Z_o \frac{2S_{21}}{\Delta} \tag{3.37c}$$

$$Z_{22} = Z_o \frac{(1-S_{11})(1+S_{22})+S_{12}S_{21}}{\Delta} \tag{3.37d}$$

where,

$$\Delta = (1-S_{11})(1-S_{22})-S_{12}S_{21}$$

The next step is to fit the imaginary parts of equation (3.36) to the imaginary parts of the Z-parameters data from equation (3.37). The curve-fitting relationships can be written as, see Appendix B,

$$\mathrm{Im}(Z_{11}) = b_{11}\omega - \frac{1}{b'_{11}\omega} \tag{3.38a}$$

$$\mathrm{Im}(Z_{12}) = b_{12}\omega \tag{3.38b}$$

$$\mathrm{Im}(Z_{21}) = b_{21}\omega \tag{3.38c}$$

$$\mathrm{Im}(Z_{22}) = b_{22}\omega \tag{3.38d}$$

where b's are the fitting coefficients. The curve fitting process may be carried out over frequency band (3-8GHz) so that the condition (3.32) is met. In addition, the lower frequency limit is set at 3 GHz so that the inductance impedances become significant with respect to the capacitive impedances, which in turn lessen the noise of the measured data. From equations (3.38), all L's can be determined as follows:

$$L_s = \frac{b_{12}+b_{21}}{2} \tag{3.39a}$$

$$L_d = b_{22} - L_s \tag{3.39b}$$

$$L_g = b_{11} \tag{3.39c}$$

The values of L_s and L_d are highly accurate because the nature of the data from which they are calculated is simple, straight line. On the other hand, the value of L_g is less accurate because, although the lower frequency is set at as big as 3 GHz, the data from which it is calculated is a combination of a capacitance impedance and L_g impedance. The capacitance impedance is usually much larger than the L_g impedance.

For this reason, it is recommended to calculate L_g at pinch-off voltage as it was explained in section 3.2.3.

3.4 Extraction of MESFET Model Parameters at Normal Bias Conditions:

In sections 3.1 through 3.3, we discussed the essential elementary processes for extracting the elements of the equivalent circuit model of a MESFET device. It is time now to put those processes together to show complete techniques for extracting MESFET-model parameters. Many techniques were proposed to accomplish this purpose. They are different in accuracy, required measurements, and time to extract. Direct measurements based techniques were pioneer techniques. In the past two decades, some optimization techniques were evolved. We will discuss some of these techniques in detail in this section.

3.4.1 Direct Measurements Based Techniques:

The extrinsic elements can be determined from DC forward biased gate measurements. Fukui [10] suggested this method which has been used later on by many authors. The gate junction is forward biased in three different configurations. In the first configuration, the source is connected to ground while the drain is open. In the second configuration, the drain is connected to ground while the source is open. In the third configuration, both drain and source are connected together to ground. Figure 3.7 depicts those different configurations.

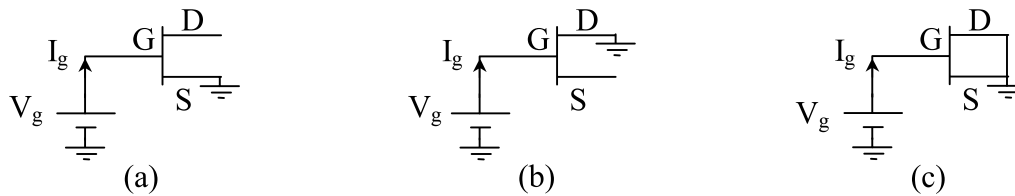

Figure 3.7 Gate junction forward-biased in different configurations: (a) source is connected to ground while drain is open, (b) drain is connected to ground while source is open, (c) both drain and source are connected to ground.

The gate junction is forward biased in order to excite the forward characteristics of the gate junction diode. In each configuration, one can infer an equation which governs the relationship between parasitic resistances in the circuit. Solving them together, all parasitic resistances can be determined.

Inductances can be calculated using the technique described in section 3.3 or simply by optimizing the circuit in Figure 3.6 where R's are known [16]. At this point, all extrinsic parasitics have been determined. The estimation of the pad capacitances requires a special structure on the same wafer of the device [23]. This structure is just a dummy structure which only contains the transistor-metalization for the gate, drain, and source pads on semi-insulating substrate. The pad capacitances are then determined analytically from measured S-parameters of this structure.

The next step is to calculate all the intrinsic parameters using the technique described in section 3.1 where all extrinsic parameters are well known.

Although this technique is fast and reliable, the associated accuracy with elements such as extrinsic parasitic resistances is not high. It is well known that R_s and R_d are bias dependent. Therefore, they have to be estimated at the normal bias condition, not forward biased gate condition. Moreover, the value of R_g derived from DC measurements is not equal to that derived at microwave frequencies because of the skin effect [11]. The accuracy degradation of those extrinsic resistive elements directly degrades the accuracy of the other resistive elements in the model (R_i and g_{ds}).

3.4.2 Shirakawa's Optimization Technique:

Shirakawa et al. [29] proposed an approach to extract a HEMT equivalent circuit from one set of S-parameter measurements at the bias point of interest. Although the used model in this approach is the same as that of a MESFET, a precaution should be taken into account regarding the measurement frequency bandwidth. They proved the validity of their approach using measurements up to 62.5 GHz which is not possible for any MESFET device.

The model used throughout this approach is shown in Figure 3.1 with R_{gd}=0 and both pad capacitances C_{pg} and C_{pd} are neglected. However, They kept the significance of R_{gd} during the solution by using equations (3.9) with only d_2=0. The procedure can be explained over the next steps:

1- Initial values for the extrinsic parameters R_g, R_d, R_s, L_g, L_d and L_s should be set. They claim that the initial values have little effect on the final results. Consequently, zero initial values can be assumed.
2- The intrinsic parameters C_{gs}, R_i, C_{gd}, g_m, τ, g_{ds}, and C_{ds} should be calculated following the same procedure discussed in section 3.1. The final solution is the same as equations (3.9) with R_{gd}=0 and d_2=0. For simplicity through the next steps, we can assume all intrinsic parameters are equal to functions f_1 through f_7 which should be functions of ω_i and all extrinsic parameters. The intrinsic parameters can be written at each frequency point "i" as:

$$C_{gs}(\omega_i, R_g, R_d, R_s, L_g, L_d, L_s) = f_{1i}(\omega_i, R_g, R_d, R_s, L_g, L_d, L_s) \quad (3.40a)$$

$$R_i(\omega_i, R_g, R_d, R_s, L_g, L_d, L_s) = f_{2i}(\omega_i, R_g, R_d, R_s, L_g, L_d, L_s) \quad (3.40b)$$

$$C_{gd}(\omega_i, R_g, R_d, R_s, L_g, L_d, L_s) = f_{3i}(\omega_i, R_g, R_d, R_s, L_g, L_d, L_s) \quad (3.40c)$$

$$g_m(\omega_i, R_g, R_d, R_s, L_g, L_d, L_s) = f_{4i}(\omega_i, R_g, R_d, R_s, L_g, L_d, L_s) \quad (3.40d)$$

$$\tau(\omega_i, R_g, R_d, R_s, L_g, L_d, L_s) = f_{5i}(\omega_i, R_g, R_d, R_s, L_g, L_d, L_s) \quad (3.40e)$$

$$g_{ds}(\omega_i, R_g, R_d, R_s, L_g, L_d, L_s) = f_{6i}(\omega_i, R_g, R_d, R_s, L_g, L_d, L_s) \tag{3.40f}$$

$$C_{ds}(\omega_i, R_g, R_d, R_s, L_g, L_d, L_s) = f_{7i}(\omega_i, R_g, R_d, R_s, L_g, L_d, L_s) \tag{3.40g}$$

3- The objective is to find a set of reasonable values for the extrinsic parameters so that the intrinsic parameter values are independent of frequency. In other words, they have the same values at all frequency points i's. Thus, criteria should be formulated to describe this objective. The variances are chosen as criteria so that variances should be as minimum as possible:

$$\varepsilon_1^k\left(R_g, R_d, R_s, L_g, L_d, L_s\right) = \frac{1}{N-1}\sum_{i=0}^{i=N-1}\left|f_{ki} - \bar{f}_k\right|^2 \tag{3.41}$$

where,

$$\bar{f}_k = \frac{1}{N}\sum_{i=0}^{i=N-1} f_{ki}$$

$\bar{f}_k$ is the mean value of f_k and k varies from 1 to 7. Another criterion is added for stable calculations. This criterion is intended to minimize the error between the measured and calculated S-parameters. The mean values of the intrinsic parameters are used to calculate S-parameters. The criterion is:

$$\varepsilon_2\left(R_g, R_d, R_s, L_g, L_d, L_s\right) = \sum_{p=1}^{2}\sum_{q=1}^{2}\sum_{i=1}^{N} W_{pq}\left|S_{pq}(\omega_i) - S_{cpq}(\omega_i, R_g, R_d, R_s, L_g, L_d, L_s)\right|^2 \tag{3.42}$$

where S_{pq} and S_{cpq} are the measured and calculated S-parameters, respectively. W_{pq} are weighting factors fixed at 0.5. Equations (3.41) and (3.42) constitute the extended error vector which fully represent the objective function of the optimization problem.

$$\varepsilon = \begin{pmatrix} \varepsilon_1^k \\ \varepsilon_2 \end{pmatrix} \tag{3.43}$$

4- The error ε is compared with certain error tolerance ε_o. If ε is not less than ε_o, the values of the extrinsic elements should be modified using Levenberg-Marquardt's method. Then, steps 2 through 4 should be repeated until ε is less than ε_o.

Although this method eliminates the need of extra measurements, it is proven for HEMT modeling over wide frequency band. Moreover, this method is very sensitive to any little measurement error. Therefore, broadband and ideal measurements are essential for reliable and accurate results. My results, in the next chapter, show that it is not applicable for extracting MESFET's parameters over a frequency band as small as (0.2-12.2 GHz) in the presence of measurement errors.

3.4.3 Ooi's Method:

Ooi et al. [30] extended Shirakawa's method to work with MESFET modeling. They almost followed Shirakawa's method algorithm. However, the main difference was that they wrote the gate resistance R_g as a function of the remaining extrinsic parameters. This alteration reduced the number of the optimization parameters which in turn resulted in a faster algorithm. R_g was added as an eighth function to the intrinsic parameter functions, equation (3.40).

From equation (3.8), one can recognize that the real part of Y_{int12} is equal to zero if R_{gd}=0. In Ooi's method the same assumptions of Shirakawa's method should be assumed that pad capacitances are neglected and R_{gd}=0. Then, one can follow the same approach explained in Figure 3.2 to derive the real part of Y_{int12} as a function of real and imaginary parts of Z-parameters as well as the extrinsic parameters. Z-parameters can be calculated from the measured S-parameters directly where pad capacitances are equal to zero. Equating real part of Y_{int12} to zero and solving for R_g, R_g can be expressed as a function of other extrinsic parameters which can be added as an eighth function to equation (3.40):

$$R_g(\omega_i, R_d, R_s, L_g, L_d, L_s) = f_{8i}(\omega_i, R_d, R_s, L_g, L_d, L_s) \quad (3.44)$$

We may have noticed that R_g should be omitted from equation (3.40) as an independent parameter. The first error criterion ε_1^k has been changed a little bit than that mentioned in equation (3.41):

$$\varepsilon_1^k\left(R_d, R_s, L_g, L_d, L_s\right) = \frac{1}{N-1}\sum_{i=0}^{i=N-1}\left|\rho_k\left(f_{ki} - \bar{f}_k\right)\right|^2 \quad (3.45)$$

where,

$$\bar{f}_k = \frac{1}{N}\sum_{i=0}^{i=N-1} f_{ki}$$

where k varies from 1 to 8. ρ_k is a normalizing factor which confines f_{ki} between one and zero. The normalizing factor seems to be vital because it brings all functions to the same order of magnitudes, then, all variances have the same weight in the objective function. Ooi's method follows exactly the same optimization algorithm to update the optimization parameters.

Ooi's method has been shown that it works successfully on MESFET device measurements over frequency band (0.5-26.5GHz). My results in the next chapter, similar to Shirakawa's method, show that this method does not lead to accurate results if the measured S-parameters are perturbed with a little bit of noise.

3.4.4 Bidirectional Search Optimization Method:

Lin and Kompa [28] proposed a new optimization concept to extract MESFET model elements. They used a bidirectional optimization technique. In this method, the model parameters are divided into two optimization parameter groups. The extrinsic elements along with pad capacitances comprise the external optimization parameters whereas the

intrinsic parameters comprise the internal optimization parameters. Figure 3.8 depicts this idea.

The optimization is carried out in two opposite directions. From outside to inside, the external optimization parameters determine the intrinsic Y-parameters from measured S-parameters. From inside to outside, the internal optimization parameters fit the branch admittances by frequency-weighted curve fitting, Appendix B,. The branch admittances are directly calculated from the intrinsic Y-parameters "Y_{int}".

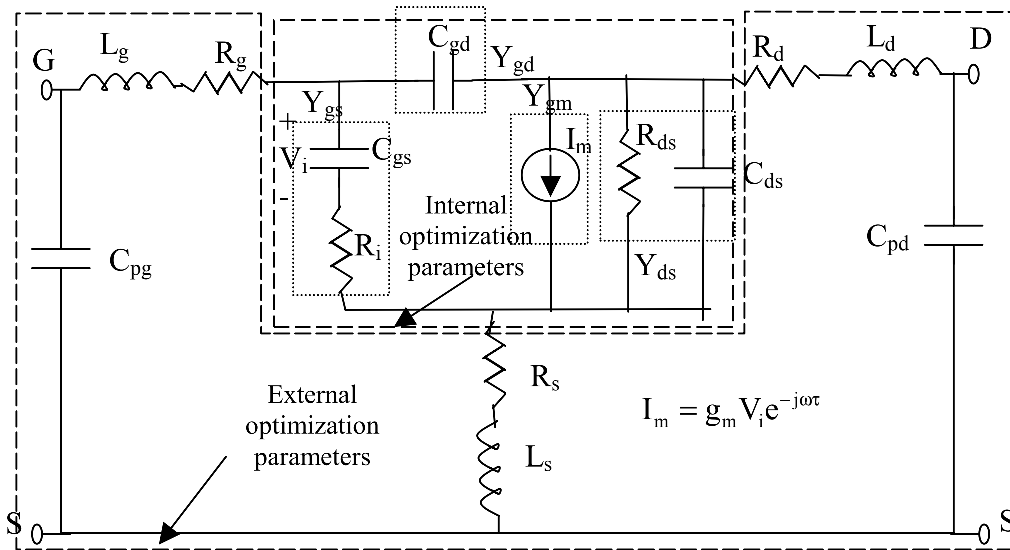

Figure 3.8 A MESFET model showing the internal and external optimization parameters and branch admittances.

This method is not as sensitive to the measurement errors as other optimization methods we discussed so far. Nevertheless, it requires initial values as close as possible to the expected solution; otherwise, the solution may get trapped in a local minimum far away from the expected one. For this reason, the initial values are calculated from pinch-off measurements as discussed in section 3.2.2. l_1-norm objective function is used for the external optimization because the convergence is faster, according to the authors' statement. The l_1-norm objective function is suitable with non-gradient optimization algorithms. So, modified simplex algorithm is used with this method. On the other hand,

l_2-norm is used with the internal curve fitting. The procedure of this method can be summarized as:

1- Initial values for the external optimization parameters should be calculated from S-parameter measurements at voltage less than or equal to pinch-off voltage (section 3.2.2).
2- The intrinsic Y-parameters "Y_{int}" should be determined as shown in section 3.1.1, equation (3.5). Then, all branch admittances Y_{gs}, Y_{gd}, Y_{gm}, and Y_{ds} can be calculated.
3- The internal optimization parameters are used to best fit the corresponding branch admittances, as shown in Appendix B. R_i and C_{gs} are used to fit Y_{gs}. C_{gd} can be calculated from Y_{gd}. g_m and τ are used to fit Y_{gm}. R_{ds} and C_{ds} are used to fit Y_{ds}.
4- S-parameters should be calculated in a reverse order to Figure 3.2 from inside to outside. The objective function is the l_1-norm discrepancy between the measured and the calculated S-parameters:

$$\varepsilon = \frac{1}{4N}\sum_{p=1}^{2}\sum_{q=1}^{2}\sum_{i=1}^{N}\frac{\left|\mathrm{Re}\left(\Delta S_{pq}(\omega_i,\vec{x})\right)\right| + \left|\mathrm{Im}\left(\Delta S_{pq}(\omega_i,\vec{x})\right)\right|}{\left|S_{pq}\right|_{max}} \tag{3.46}$$

where,

$$\Delta S_{pq}(\omega_i,\vec{x}) = S_{pq}(\omega_i) - S_{cpq}(\omega_i,\vec{x})$$

$\vec{x}$ represents the vector of model parameters: internal and external.

5- ε in equation (3.46) should be optimized to find the minimum error. The suggested optimization algorithm is the improved Simplex [28]. If ε is not the minimum, the external optimization variables should be updated and steps 2 through 5 should be repeated.

The curve fitting introduced in this method desensitizes the method to the measurement errors. However, it is important for this method to work over relatively broadband measurements (1-40 GHz) for accurate results. It also needs initial values as

close as possible to the expected minimum. Our results, in the next chapter, show many local minimums for the suggested objective function.

3.5 A Novel Systematic Parameter-Extraction Technique:

We have proposed a new systematic technique to extract MESFET model parameters. Our technique exploits the advantages of all previous techniques to end up with a robust and reliable method. Our method can work over any frequency bandwidth for the measured S-parameters, which may have certain unavoidable measurement errors. This method consists of two major steps:

1- The parasitic inductances (L_d and L_s) and the pad capacitances (C_{pg} and C_{pd}) as well as the gate resistance R_g should be iteratively estimated from Cold-Measurements at V_{ds}=0 and V_{gs}=0 and S-parameter measurements at gate voltage less than or equal to pinch-off voltage. This step will be discussed in detail after a while.

2- Knowing L_d, L_s, C_{pg}, C_{pd}, and R_g, all other parameters can be calculated from S-parameter measurements at normal bias conditions. In this step, an optimization technique should be employed to optimize the extrinsic elements, other than the known extrinsic parameters priory calculated, to best fit the measured S-parameters and to best describe the frequency independence of some intrinsic elements.

These two steps will be discussed in much detail in the following subsections.

3.5.1 The Iterative Scheme for Estimation of L_d, L_s, C_{pg}, C_{pd}, and R_g:

This is the first phase of our proposed technique in which L_d, L_s, C_{pg}, C_{pd}, and R_g should be estimated. It comprises the execution of two optimization procedures iteratively until consistent values for L_d, L_s, C_{pg}, C_{pd}, and R_g are achieved. The first optimization procedure is designated to estimate L_d, and L_s using cold-measurements, which is described in section 3.3. The second optimization procedure is implemented to

extract C_{pg}, C_{pd}, and R_g from S-parameter measurements at gate voltage less than or equal to pinch-off voltage as described in section 3.2.3. The flow chart of this iterative scheme is shown in Figure 3.9.

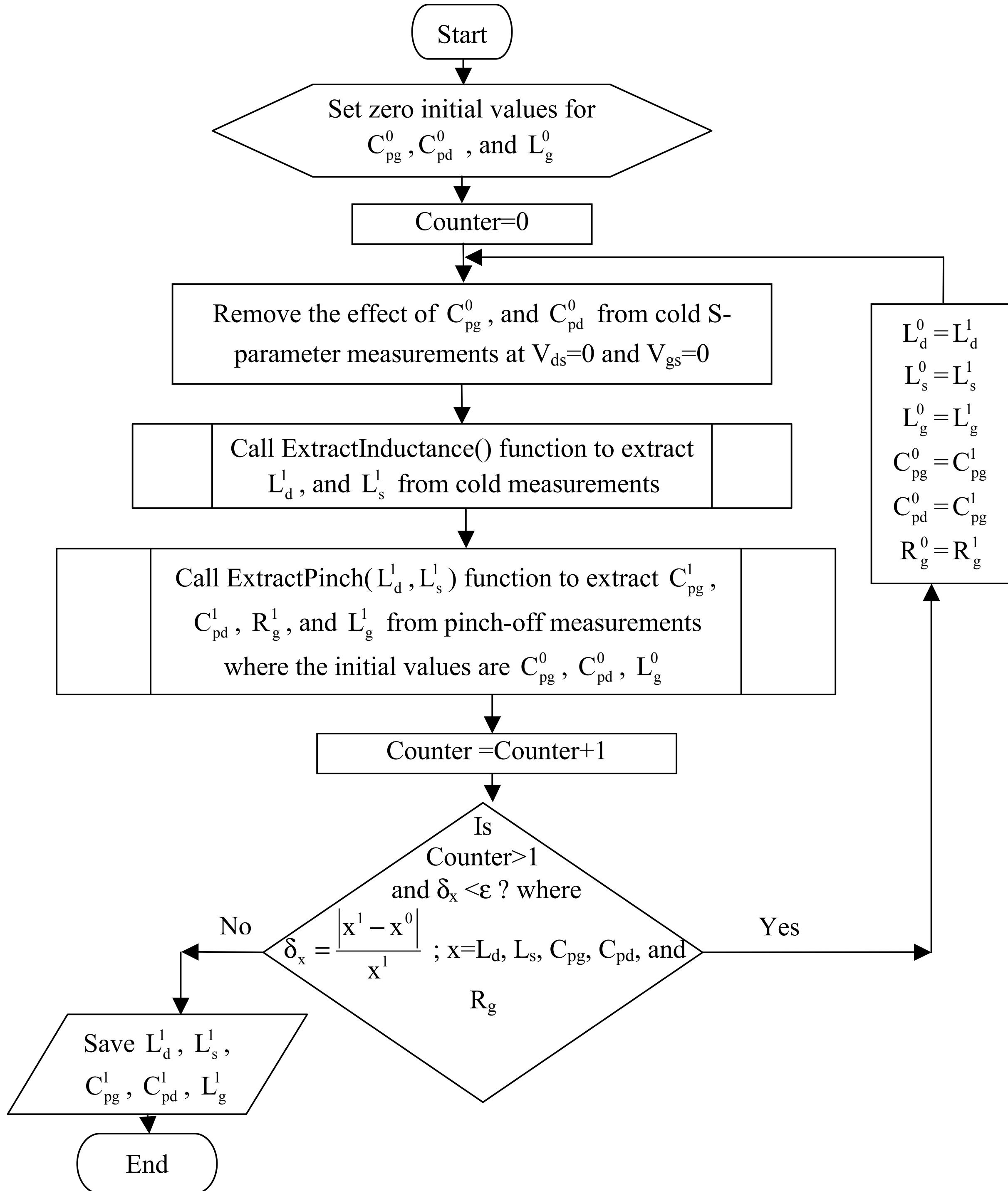

Figure 3.9 Flow chart of the iterative scheme to estimate L_d, L_s, C_{pg}, C_{pd}, and R_g.

In the first iteration, we assume that both C_{pg} and C_{pd} are equal to zero. The L_d and L_s are extracted from the cold measurements at V_{ds}=0 and V_{gs}=0 using a function called ExtractInductance(). This function exactly follows the technique described in section 3.3. Knowing the values of L_d and L_s, the parameters C_{pg} and C_{pd}, R_g, and L_g are extracted from pinch-off S-parameter measurements using a function called ExtractPinch(). This function implements the algorithm of section 3.2.3. L_g is estimated at this step to be used as the initial value for the next iteration. L_d and L_s are supplied to this function to be used as known variables. Finally, the objective function is checked out after the second iteration. The objective function implies that the absolute difference between two consecutive values of each variable with respect to its new value must be less than certain tolerance ε. The variables, whose errors must be checked, are L_d, L_s, C_{pg}, C_{pd}, and R_g. The objective function can be rewritten as:

$$\delta_x = \frac{\left| x^1 - x^0 \right|}{x^1} \tag{3.47}$$

where x=L_d, L_s, C_{pg}, C_{pd}, and R_g

If δ_x of each variable is less than ε, then the current values of the variables are saved; otherwise, C_{pg} and C_{pd} are removed from the cold S-parameter measurements and the procedure is repeated with the new values of L_d, L_s, C_{pg}, C_{pd}, R_g, and L_g. This scheme has been tested on the measurements of several devices whose structure are similar on the same wafer. It shows consistent values for the extracted variables as will be shown in the next chapter.

3.5.2 Estimation of the Unknown Parameters at Normal Bias Conditions:

This phase of the proposed technique is the last step, which should be described in more details. In fact, this step is the heart of our technique and lies in the middle between Shirakawa’s method and Lin’s method. Thus, it enjoys the advantages of both methods. Five elements have been estimated from the first step to reduce the number of unknowns

to ten elements. These elements are: R_d, R_s, L_g, C_{gs}, C_{gd}, C_{ds}, R_i, R_{ds}, g_m, and τ. The first three elements are the optimization variables. Although we can reduce the number of unknowns by using the value of L_g estimated from the iterative scheme of the previous subsection, we keep it unknown to compare its value with the predetermined one. Our results show good match between the value extracted at normal bias conditions and the value extracted from the iterative scheme.

Since the search space is reduced to three variables only, the convergence is much faster than that of the aforementioned methods. We start our procedure by removing the effect of C_{pg} and C_{pd} from the measured S-parameters. The optimization process then starts to match the calculated S-parameters with the measured ones and to achieve constant distribution for the intrinsic elements over the frequency band.

Our intensive computer work has shown that all intrinsic-resistive elements R_i and R_{ds} as well as τ are very sensitive to any measurement error such that any little error in measurements results in big errors in those elements. This phenomenon is specially pronounced at low frequency points. In contrast, all other elements are insensitive to such measurement error. This may be attributed to the nature of the model where all capacitances and g_m are prominent over other elements. This fact results in small values for the real parts of intrinsic Y-parameters compared to their associated imaginary parts. Consequently, all real parts, from which the resistive elements and τ are calculated, are very noisy especially at low frequency points.

This phenomenon guides us to use a similar error criterion similar to equation (3.45), but we should drop out the contributions of R_i, R_{ds} and τ from the error criterion. Moreover, the errors of the other components are estimated over the upper half of the frequency range only. This makes our objective function numerically stable and less sensitive to measurement error, which is well pronounced over the low frequency range. On the other hand, we use curve-fitting to calculate those elements, R_i, R_{ds}, and τ, in a way similar to that of Lin's method. We also use the l_2-norm of the discrepancy between the measured and calculated S-parameters as a complementary error criterion. Both

criteria together assure good matching between the measured and calculated S-parameters and constant element values over the frequency band of interest. The error criteria read:

$$\varepsilon_1^k\left(R_d, R_s, L_g\right) = \frac{1}{N}\sum_{i=N/2}^{i=N-1}\left|\rho_k\left(f_{ki} - \bar{f}_k\right)\right|^2 \qquad (3.48)$$

where,

$$\bar{f}_k = \frac{1}{N}\sum_{i=0}^{i=N-1} f_{ki}$$

f_{ki} is defined in equation (3.40) where R_g, L_d, and L_s are omitted from the argument list since they are no longer optimization variables. K takes the values: 1, 3, 4 and 7. f_k can be calculated the same way explained in section (3.1) leading to equation (3.10). The normalizing factor ρ_k is formulated in such a way so that all errors for different k's remain within the same order of magnitudes. It also enhances the error if f_{ki} is less than -1. ρ_k can be written in the following mathematical form:

Assuming: $\max f_k = \max_i(f_{ki})$ where i varies from N/2 to N-1

and $\min f_k = \min_i(f_{ki})$, where i varies from N/2 to N-1

If $\max f_k >= \left|\min f_k\right|$, then $\rho_k = \dfrac{1}{\max f_k}$

Else if $\min f_k >= -1$, then $\rho_k = \dfrac{1}{\left|\min f_k\right|}$

Otherwise $\rho_k = 1$. (3.49)

The second error criterion can be written as:

$$\varepsilon_2\left(R_d, R_s, L_g\right) = \sum_{p=1}^{2}\sum_{q=1}^{2}\sum_{i=1}^{N} W_{pq}\left|\frac{S_{pq}(\omega_i) - S_{cpq}(\omega_i, R_d, R_s, L_g)}{G_{pq}}\right|^2 \qquad (3.50)$$

where,

$$G_{11} = G_{22} = \max_i(|S_{11}(\omega_i)|)$$

$$G_{21} = G_{12} = \max_i(|S_{21}(\omega_i)|)$$

The weighting factor W_{pq} is set at 0.5. The normalization factor G_{pq} has already been discussed in section 3.2.3. The total error function can be determined as:

$$\varepsilon(R_d, R_s, L_g) = \sum_k \varepsilon_1^k + \varepsilon_2 \tag{3.51}$$

Equation (3.51) is called the error function (or the objective function) of our technique. The minimum of the objective function should be calculated using an optimization algorithm. The initial values of the optimization variables R_d, R_s, and L_g are those values estimated in step 1 of our proposed technique.

Our proposed optimization technique was applied to some MESFET device measurements to show small negative values for R_s at some bias points. As a result, a constraint should be imposed on R_s to avoid negative values. The constraint implies a modification to the value of R_s supplied to the objective function in case of negative values of R_s. The modification must assure the continuity of the first derivative of the objective function at all values of R_s in order not to disturb the gradient-based optimization algorithm used to locate the minimum point. The value of R_s is limited to a small positive number ULV. The value of R_s does not change for values of R_s larger than ULV. If R_s is to have a value smaller than ULV but larger than another positive value LLV, the R_s is assumed to be fixed at ULV. Otherwise, if R_s is to have smaller number than LLV, a penalty value of R_s is suggested so that the objective function becomes big. Typical values for ULV and LLV are 10^{-4} and 10^{-10}, respectively. The small range between ULV and LLV helps the first derivative of the objective function to be continuous. The modification can be mathematically expressed as:

If $R_s \geq$ ULV, then R_s=R_s

Elseif LLV $\leq R_s <$ ULV, then R_s=ULV

Else R_s=ULV+100*(LLV-R_s) (3.52)

3.6 Extraction of Large-Signal Model Parameters:

This section shows the relation between the small-signal model and large-signal model. The large-signal model is shown in Figure 2.5, Section 2.3 also demonstrates how the small-signal parameters are derived from the counterpart elements of the large-signal model. In this chapter, so far, we have explained the extraction process of the small-signal model parameters. The small-signal model parameters can be used to build up the large signal model.

There are many empirical large-signal models in the literature [2] and [33]. Each model proposes a set of equations to model the drain-source current (I_{ds}), the gate-source capacitance, and the gate-drain capacitance. Golio [2] showed that Advanced Curtice Model, which has been adopted by Meta-Software, achieved the best match between the measured and the modeled data. For this reason, we will use Advanced Curtice Model to explain the potential role of the small-signal model in building up the large-signal model. We will not go into deep analysis of the large-signal model nor verify its accuracy.

Moreover, we will confine our discussion to the model of the drain-source current only. Similar analysis can be applied to the gate-source, and the gate-drain capacitances. I_{ds} of Advanced Curtice Model can be expressed as:

$$I_{ds} = \beta_{eff} V_{gst}^{VGEXP} (1 + \lambda V_{ds}) \tanh(\alpha V_{ds}) \quad (3.53)$$

where

$$\beta_{eff} = \frac{\beta}{1 + \mu_{crit} V_{gst}}$$

$$V_{gst} = V_{gs} - V_p$$

$$V_p = V_{po} - \gamma V_{ds}$$

V_{gs} and V_{ds} are the intrinsic bias voltages; the effect of the extrinsic resistances should be eliminated. β, μ_{crit}, γ, V_{po}, VGEXP, λ, and α are the model parameters. The model is proposed to account for as many large-signal phenomena as possible. The pinch-off potential V_p is the modified version of the nominal pinch-off potential V_{po}, which shows dependence on V_{ds}. The current in the saturation region exhibits a square-law as a function of V_{gs} for small values of V_{gs}-V_p. It shows linear behavior for large values of V_{gs}-V_p. Thus, VGEXP has to be around 2.

The small-signal transconductance and output resistance have vital role in the modeling. They represent the link between small and large-signal models. The transconductance and the output conductance can be derived by differentiating I_{ds} with respect to V_{gs} and V_{ds}, respectively:

$$g_m = \frac{\partial I_{ds}}{\partial V_{gs}} = I_{ds}\left(\frac{VGEXP}{V_{gst}} - \frac{\mu_{crit}}{1+\mu_{crit}V_{gst}}\right) \tag{3.54}$$

$$g_{ds} = \frac{\partial I_{ds}}{\partial V_{ds}} = \beta_{eff}V_{gst}^{VGEXP}(1+\lambda V_{ds})\left(\frac{\alpha}{\cosh^2(\alpha V_{ds})}\right) + \beta_{eff}V_{gst}^{VGEXP}\lambda\tanh(\alpha V_{ds}) + g_m\gamma \tag{3.55}$$

The first step in the extraction of the large-signal model parameters is to estimate the intrinsic bias voltages to be used in the equations. The effect of R_d and R_s should be removed from the measured bias voltages. Since R_d and R_s have small values and have relatively week dependence on bias voltages, we can fix them at their average values. The average values can be calculated from the extracted values at different bias points in the saturation region. In addition, our calculations show that the effect of R_d and R_s is very slight. The intrinsic bias voltages can be estimated as:

$$V_{ds} = V_{ds}^m - I_{ds}(R_d + R_s) \tag{3.56a}$$

$$V_{gs} = V_{gs}^m - I_{ds}R_s \tag{3.56b}$$

where V_{gs}^m and V_{ds}^m are the measured terminal bias voltages. In order to estimate the large-signal model parameters, we fit the equations (3.53) through (3.55) to the measured

I_{ds}, and the extracted small-signal parameters g_m and g_{ds}, respectively. This fit process is used to compromise between the dc and ac performance of the actual device. The reason is, the analytical formulas of g_m and g_{ds} do not include the frequency dispersion because they are derived from I_{ds} model. Consequently, good fit to one measurement will come at the expense of the others. A more complex model for I_{ds} can be proposed [31] to increase the accuracy of simulating both dc and RF behaviors at the expense of the computational complexity. The I_{ds} model can be divide into dc model in parallel, with a capacitively coupled, RF model. In fact, we do not need this complexity to explain the relationship between the small-signal parameters and the large-signal model in our research. Thus, the compromising objective function is the sum of the square errors of all quantities:

$$E = \frac{1}{3n}\sum_{i=1}^{n}\left(W_{I_{ds}} E_{I_{ds}}(i) + W_{g_m} E_{g_m}(i) + W_{g_{ds}} E_{g_{ds}}(i)\right) \tag{3.57}$$

where

$$E_x(i) = \left(\frac{x_{data}(i) - x(i)}{x_{max}}\right)^2 \qquad ; x = I_{ds}, g_m, \text{ and } g_{ds}$$

n is the number of bias points and x_{max} is the maximum value of the parameter x. x_{data} is the measured or extracted small-signal parameters. $W_{I_{ds}}$, W_{g_m}, and $W_{g_{ds}}$ are weighting factors for I_{ds}, g_m, and g_{ds}, respectively. The model can be biased towards the ac characteristics of the device by increasing W_{g_m}, and $W_{g_{ds}}$, while increasing $W_{I_{ds}}$ biases the model closer to the dc characteristics of the device.

The Levenberg-Marquardt's optimization technique is used to minimize the objective function. The optimization process experiences a local minima problem. A simple random optimization technique should be applied prior to the Levenberg-Marquardt's to locate close initial values to the optimum solution. This random optimization technique is explained in section 3.7.4.

3.7 Nonlinear Optimization:

Nonlinear optimization can be defined as the process of finding the minimum or maximum of a nonlinear function. The nonlinear function for which the minimum or maximum should be determined is called the objective function. In our case, the objective function may be the error function stated in equation (3.51) or (3.57). The optimization subject is not that easy and has many aspects associated with it. Therefore, we will concern ourselves with the fundamentals of this subject so that we can fully understand the techniques used in this thesis. Since equations (3.51) and (3.57) are written in the form of the sum of squares, we will discuss two techniques for solving nonlinear least-squares optimization. These techniques are: Gauss-Newton and Levenberg-Marquardt methods. Both of them lie under the gradient optimization techniques.

Assume we have n independent variables, optimization parameters, x_1, and $x_2 \ldots x_n$ which can be written in the vector form:

$$\boldsymbol{x} = \begin{bmatrix} x_1 \\ x_2 \\ \vdots \\ x_n \end{bmatrix} \tag{3.58}$$

Assume that the objective function is called $R(\boldsymbol{x})$ which is a function of $\boldsymbol{x}$. For example, if equation (3.51) is to be optimized, the independent variables x_i's are the parameters of equation (3.51) R_d, R_s, and L_g while the objective function R is ε. The objective function can be written as a sum of squares of nonlinear function:

$$R(\boldsymbol{x}) = \sum_{i=1}^{m} r_i^2(\boldsymbol{x}) \tag{3.59}$$

where m is the total number of the nonlinear functions r_i constituting the objective function. Finding the minimum of a function like (3.59) is called nonlinear least squares. The functions r_i can be written in a vector form as:

$$\boldsymbol{r}(\boldsymbol{x}) = \begin{bmatrix} r_1 \\ r_2 \\ \vdots \\ r_m \end{bmatrix} \tag{3.60}$$

then, equation (3.59) can be written in a vector notation:

$$R(\boldsymbol{x}) = \boldsymbol{r}^{T}(\boldsymbol{x})\boldsymbol{r}(\boldsymbol{x}) \tag{3.61}$$

The gradient vector of R can be expressed as:

$$\boldsymbol{g}(\boldsymbol{x}) = \nabla R(\boldsymbol{x}) = \begin{bmatrix} \partial R / \partial x_1 \\ \partial R / \partial x_2 \\ \vdots \\ \partial R / \partial x_n \end{bmatrix} \tag{3.62}$$

First partial derivatives in equation (3.62) can be calculated from equation (3.59) as:

$$\boldsymbol{g}(\boldsymbol{x}) = 2\begin{bmatrix} \sum_{i=1}^{m} r_i \dfrac{\partial r_i}{\partial x_1} \\ \sum_{i=1}^{m} r_i \dfrac{\partial r_i}{\partial x_2} \\ \vdots \\ \sum_{i=1}^{m} r_i \dfrac{\partial r_i}{\partial x_n} \end{bmatrix} \tag{3.63}$$

If the Jacobian matrix $\boldsymbol{J}$ for the vector $\boldsymbol{r}$ is defined by,

$$\boldsymbol{J}(\boldsymbol{x}) = \begin{bmatrix} \partial r_1 / \partial x_1 & \cdots & \partial r_1 / \partial x_n \\ \vdots & \vdots & \vdots \\ \partial r_m / \partial x_1 & \cdots & \partial r_m / \partial x_n \end{bmatrix} \tag{3.64}$$

then, the gradient vector in equation (3.63) can be written as:

$$\boldsymbol{g}(\boldsymbol{x}) = \boldsymbol{2J^T r} \tag{3.65}$$

Taking the first derivatives for each element of $\boldsymbol{g}(\boldsymbol{x})$ in equation (3.62), we obtain what is called the Hessian matrix of the function R. This matrix contains the second derivatives:

$$\boldsymbol{G}(\boldsymbol{x}) = \nabla^2 R(\boldsymbol{x}) = \begin{bmatrix} \partial g_1 / \partial x_1 & \cdots & \partial g_1 / \partial x_n \\ \vdots & \vdots & \vdots \\ \partial g_n / \partial x_1 & \cdots & \partial g_n / \partial x_n \end{bmatrix} = \begin{bmatrix} \partial R / \partial x_1 \partial x_1 & \cdots & \partial R / \partial x_1 \partial x_n \\ \vdots & \vdots & \vdots \\ \partial R / \partial x_n \partial x_1 & \cdots & \partial R / \partial x_n \partial x_n \end{bmatrix} \tag{3.66}$$

The kj-element of the Hessian matrix can be calculated be differentiating the k-element of $\boldsymbol{g}(\boldsymbol{x})$ in equation (3.63) with respect to x_j:

$$G_{kj} = \frac{\partial g_k}{\partial x_j} = 2\sum_{i=1}^{m} \left(\frac{\partial r_i}{\partial x_j} \frac{\partial r_i}{\partial x_k} + r_i \frac{\partial^2 r_i}{\partial x_k \partial x_j} \right) \tag{3.67}$$

If the Hessian matrix of r_i is defined as T_i:

$$\boldsymbol{T}_i(\boldsymbol{x}) = \nabla^2 r_i(\boldsymbol{x}) \tag{3.68}$$

then, the Hessian matrix G(x) can be written as:

$$\boldsymbol{G}(\boldsymbol{x}) = 2\boldsymbol{J}^T\boldsymbol{J} + 2\sum_{i=1}^{m} r_i \boldsymbol{T}_i \tag{3.69}$$

We may notice that r_i is an error quantity or residue which should be too small at the optimization point (minimum). Thus, the second term can be neglected in equation (3.69). As a result, the Hessian matrix can be reduced to:

$$\boldsymbol{G}(\boldsymbol{x}) = 2\boldsymbol{J}^T\boldsymbol{J} \tag{3.70}$$

The equation (3.70) determines the Hessian matrix in terms of the first derivatives of the functions r_i's only. This is one of the attractive features of the least squares algorithms with small residuals that the computation of the Hessian matrix is easy.

Our optimization problem can be categorized as unconstrained optimization since we do not impose any constraints on the independent variables $\boldsymbol{x}$. This means that x_i can take any value in the real space. The necessary condition for a minimum [34] reads:

$$\boldsymbol{g}(\boldsymbol{x}^*) = 0 \tag{3.71}$$

where $\boldsymbol{x}^*$ is the solution at this minimum. The above condition is not a sufficient condition because this condition is also satisfied for other points such as maxima. The sufficient condition can be expressed as:

$$\Delta\boldsymbol{x}^T\boldsymbol{G}(\boldsymbol{x}^*)\Delta\boldsymbol{x} > 0 \tag{3.72}$$

where $\Delta\boldsymbol{x}$ is any arbitrary vector which is not equal to zero. The condition (3.72) is valid if $\boldsymbol{G}(\boldsymbol{x}^*)$ is positive definite. Fortunately, the Hessian matrix in equation (3.70) is at least positive semi-definite matrix. This can easily be proven by assuming $\boldsymbol{J}\Delta\boldsymbol{x} = \boldsymbol{Z}$, then:

$$\Delta \boldsymbol{x}^{\mathrm{T}} \boldsymbol{J}^{\mathrm{T}} \boldsymbol{J} \Delta \boldsymbol{x} = \boldsymbol{Z}^{\mathrm{T}} \boldsymbol{Z} \geq 0 \tag{3.73}$$

If the Hessian matrix is positive semi-definite, the solution $\boldsymbol{x}^*$ is probably not a minimum. However, the physical significance of our problem implies that this solution must be a minimum. To find the solution $\boldsymbol{x}^*$, equation (3.71) should be solved. Many algorithms are suggested to solve this equation to find the minimum. We will explain two algorithms. The next two algorithms can be considered as modified Newton's method. The Newton's method exhibits quadratic convergence if the Hessian matrix is positive definite. Quadratic convergence is normally the fastest convergence rate in nonlinear optimization. For this reason, Newton's method has special significance in nonlinear optimization. The Newton's method is an iterative scheme.

3.7.1 Gauss-Newton Method:

If $\boldsymbol{x}_k$ is an arbitrary point at iteration k and $\boldsymbol{S}_{\mathrm{k}}$ is an arbitrary vector, the gradient vector $\boldsymbol{g}(\boldsymbol{x})$ can be expanded in Taylor's series at the new point $\boldsymbol{x}_{k+1} = \boldsymbol{x}_k + \boldsymbol{S}_k$:

$$\boldsymbol{g}_{k+1} = \boldsymbol{g}(\boldsymbol{x}_{k+1}) = \boldsymbol{g}_k + \boldsymbol{G}_{\mathrm{k}} \boldsymbol{S}_k \tag{3.74}$$

The higher order terms are neglected. If $\boldsymbol{x}_{k+1}$ is assumed to be the minimum of the function, then $\boldsymbol{g}_{k+1}$ must be equal to zero according to equation (3.71), and in turn equation (3.74) can be reduced to:

$$\boldsymbol{G}_{\mathrm{k}} \boldsymbol{S}_k = -\boldsymbol{g}_k \tag{3.75}$$

Substituting for $\boldsymbol{g}_k$ and $\boldsymbol{G}_{\mathrm{k}}$ from equations (3.65) and (3.70), respectively, equation (3.75) can be expressed as:

$$\boldsymbol{J}_{\mathrm{k}}^{\mathrm{T}} \boldsymbol{J}_{\boldsymbol{k}} \boldsymbol{S}_{\boldsymbol{k}} = -\boldsymbol{J}_{\mathrm{k}}^{\mathrm{T}} \boldsymbol{r}_{\boldsymbol{k}} \tag{3.76}$$

Equation (3.76) is a set of linear equations which should be solved for $\boldsymbol{S}_{\mathrm{k}}$. $\boldsymbol{S}_{\mathrm{k}}$ represents the difference between the new point and the old point in the iteration process, so, it is called the Search Vector. The new point can then be written as:

$$\boldsymbol{x}_{\boldsymbol{k+1}} = \boldsymbol{x}_{\boldsymbol{k}} + \boldsymbol{S}_{\boldsymbol{k}} \tag{3.77}$$

Then, equation (3.76) should be solved at the new point and the process has to be repeated iteratively until proper termination criteria are met. The flow chart in Figure 3.10 shows the Gauss-Newton algorithm.

The termination criteria consist of three conditions which must be satisfied simultaneously in order that the process terminates. The first criterion implies that the maximum component of the search vector should be less than certain tolerance δ_1. δ_1 determines the number of accurate digits for $\boldsymbol{x}$. The second criterion is imposed to assure that the function reaches constant value at the minimum. In other words, the difference in function values for two successive iterations is less than certain tolerance δ_2. The last error criterion represents the original condition of the minimum imposed by equation (3.71) that the maximum component of the gradient vector should be less than certain tolerance δ_3. Typical values for δ_1 and δ_2 can be 10^{-4} and 10^{-8}, respectively. Our experience also shows that δ_3 may be set as a combination between δ_1 and δ_2:

$$\delta_3 = 0.1(\delta_1 + \delta_2) \tag{3.78}$$

The Gauss-Newton's method shows good convergence if the function at the minimum is small. It encounters convergence problems if the function value at the minimum is relatively large because the second order term in the equation (3.69) may become significant. Other methods modify Gauss-Newton's method to overcome this problem.

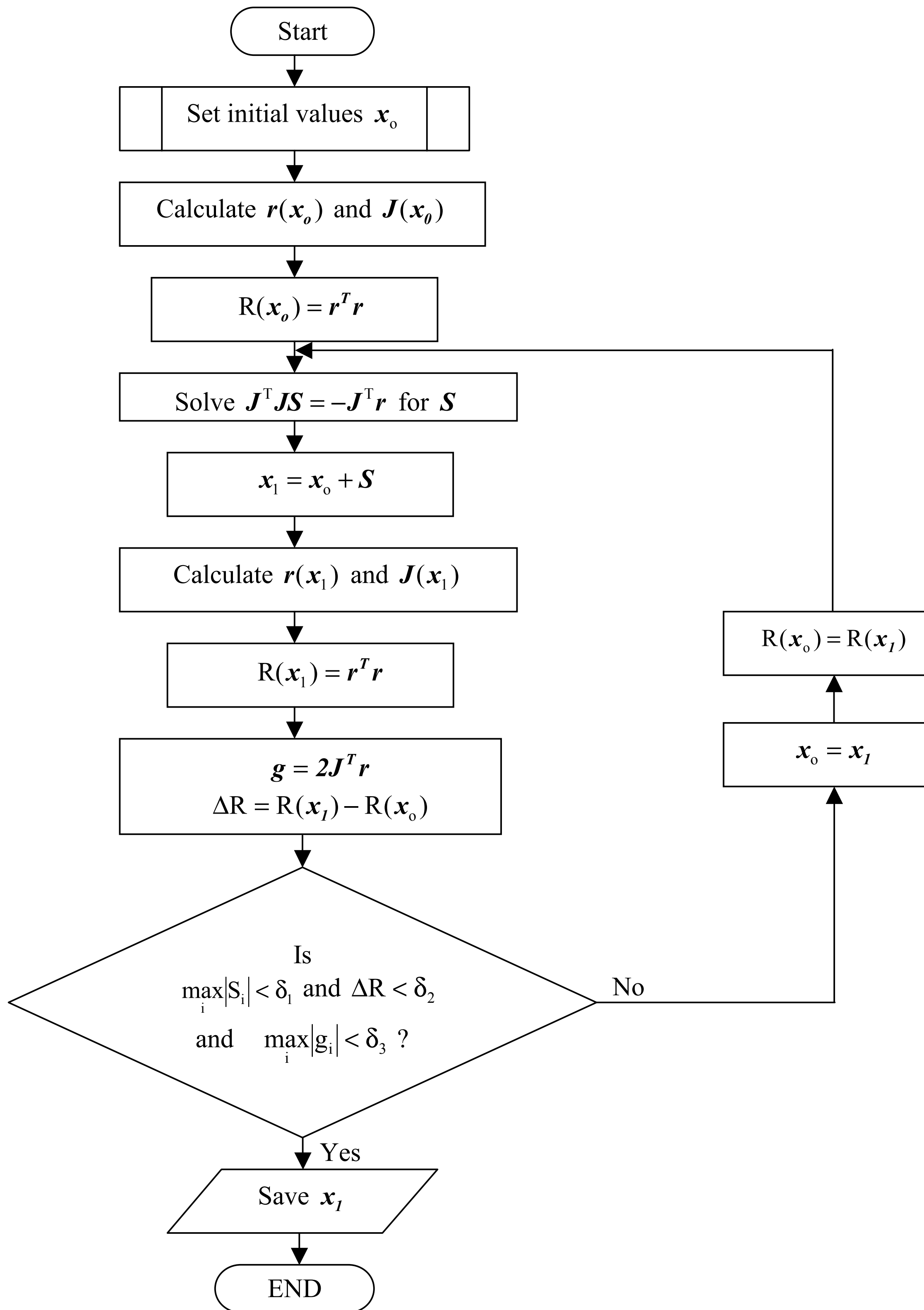

Figure 3.10 Flow Chart for Gauss-Newton optimization method.

3.7.2 Levenberg-Marquardt Method:

This method is basically a modified Gauss-Newton's method. It solves the convergence problem associated with Gauss-Newton's method in case of relatively large function value at the minimum. Equation (3.76) can be simply modified to:

$$\left(\boldsymbol{J}_k^T \boldsymbol{J}_k + \mu_k \boldsymbol{I}\right)\boldsymbol{S}_k = -\boldsymbol{J}_k^T \boldsymbol{r}_k \tag{3.79}$$

where μ_k is a positive scalar variable and $\boldsymbol{I}$ is the unit matrix of order n. Equation (3.79) is solved to calculate the search direction at iteration k. μ_k is modified for each iteration. It can be controlled so that the matrix $\left(\boldsymbol{J}_k^T \boldsymbol{J}_k + \mu_k \boldsymbol{I}\right)$ is positive definite. As μ_k increases, it becomes more difficult for the process to diverge. However, the convergence rate decreases. Therefore, it is important to decrease μ_k as minimum as possible to approach the quadratic convergence rate of Gauss-Newton's method. A strategy for selecting μ_k was proposed by Marquardt [34]. It compares the function value of the new iteration with that of the current value, and if it is large, μ_k should increases. Otherwise, it accepts the value of μ_k and moves to the next iteration. The change of μ_k is determined by another positive factor ν. ν is usually equal to 10 and the initial value of μ is equal to 0.01. The algorithm of Levenberg-Marquardt's method can be explained as follows:

1. Set initial values for $\boldsymbol{x}_o$, μ=0.01, and ν=10
2. Set $\mu=\mu/\nu$
3. Repeat
4. Solve $\left(\boldsymbol{J}_o^T \boldsymbol{J}_o + \mu \boldsymbol{I}\right)\boldsymbol{S}_o = -\boldsymbol{J}_o^T \boldsymbol{r}_o$ for $\boldsymbol{S}_o$
5. $\boldsymbol{x}_1 = \boldsymbol{x}_o + \boldsymbol{S}_o$
6. if R($\boldsymbol{x}_1$)>R($\boldsymbol{x}_o$)
7. $\mu=\mu\,\nu$
8. end
9. Until R($\boldsymbol{x}_1$)<R($\boldsymbol{x}_o$)
10. $\boldsymbol{x}_o = \boldsymbol{x}_1$ and R($\boldsymbol{x}_o$)=R($\boldsymbol{x}_1$)

11. If all termination error criteria mentioned in the flow chart of Figure 3.10 are met, then stop the process, else go to step number 2.

3.7.3 The First Derivative Calculation:

The reader might have noticed that we need to calculate the first order derivative of all functions for the determination of the Jacobian matrix. The functions in our case are complicated and therefore it is not wise to look for analytical formula for such derivatives. In this case, we resort to a numerical technique to calculate derivatives. Finite difference approximation is a good candidate for derivatives. The derivative of the functions with respect to a variable x_j can be written in terms of the forward difference equation as:

$$J_j = \frac{\partial \boldsymbol{r}}{\partial x_j} = \frac{\boldsymbol{r}(x_j + \Delta_j) - \boldsymbol{r}(x_j)}{\Delta_j} \tag{3.80}$$

where J_j is the jth column of the Jacobian matrix and j varies from 1 to n. Δ_j is an infinitesimal quantity which can be computed as [34]:

$$\Delta_j = \max\left(\min\left(|R(\boldsymbol{x})|, \Delta'_j \right), \xi^{\frac{1}{2}} \right) \tag{3.81}$$

where, $$\Delta'_j = \begin{cases} \xi^{\frac{1}{2}} & \text{if} |x_j| < 10^3 \xi^{\frac{1}{2}} \\ 10^{-3}|x_j| & \text{if} |x_j| \geq 10^3 \xi^{\frac{1}{2}} \end{cases}$$

ξ is the machine relative precision which is approximately equal to 10^{-16} in IBM double precision. The above rule for choosing Δ_j was reported that its performance in our iterative techniques is closely similar to that of the corresponding analytical derivative algorithms. It attempts to balance truncation and cancellation error to some extent when working with a digital computer precision.

3.7.4 Random Optimization Technique:

A random optimization technique is vital in the extraction of the large-signal model parameters. It is used in conjunction with a gradient method, such as Levenberg-Marquardt's, to supply it with a new starting point every time it is run. This starting point is usually close to the optimum solution. The random optimization technique requires prior knowledge about the magnitude limits of each variable. This knowledge is usually available for our problems. Knowing such limits, one can bracket the minimum of the objective function. The algorithm of a simple random optimization technique can be demonstrated as follows:

1. Set N=number of optimization variables
2. Set tol=tolerance termination value
3. Set MaxIterations=maximum number of iterations
4. Bracket each variable by imposing maximum and minimum limits $\boldsymbol{x}_{max}$ and $\boldsymbol{x}_{min}$
5. k=0, and R($\boldsymbol{x}_o$)=R($\boldsymbol{x}_{min}$)
6. Repeat
7. Set $\boldsymbol{M}$=vector of random numbers between 0 and 1
8. For i=1 to N
9. $x_1(i)=x_{min}(i)+(x_{max}(i)- x_{min}(i))M(i)$
10. Next i
11. Evaluate R($\boldsymbol{x}_1$)
12. If R($\boldsymbol{x}_1$) < R($\boldsymbol{x}_o$), then R($\boldsymbol{x}_o$)=R($\boldsymbol{x}_1$) and $\boldsymbol{x}_o = \boldsymbol{x}_1$
13. k=k+1
14. Until (R($\boldsymbol{x}_o$) < tol) or (k > MaxIterations)

This is a simple technique for random optimization. Other sophisticated techniques can be used to resolve the problem of the local minima. One of these techniques is the Simulated Annealing.

Chapter 4
Results and Analyses

In the previous chapter, we addressed many techniques for extracting small-signal model parameters for MESFET devices. In this chapter, we will discuss the results of these techniques and argue their significance and accuracy. We will also show how accurate our proposed technique is. The argument will be supported by hypothetical measurement data analysis. Some thermal results for the model parameters will also be presented. In addition, we will discuss the drain-source current modeling in large-signal models.

4.1 S-Parameter Measurements Data and Error Sources:

To verify the modeling techniques discussed in the previous chapter, a hypothetical MESFET model is assumed. In this hypothetical model a set of small-signal model parameters, which resemble typical values of a MESFET device, are assumed. In addition to verification, using known model parameters allows us to evaluate the reliability and robustness of the modeling technique and estimate the accuracy of each extracted parameter in the model. In addition, the hypothetical model can be used to investigate the technique and its convergence properties.

We will investigate each technique and its associated programming code using a hypothetical set of data first. If it shows good results, then we will apply it to the actual device measurements. The candidate MESFET model parameters of the hypothetical device are tabulated in Table 4.1 [2]. The pad capacitances C_{pg} and C_{pd} are excluded for simplicity during evaluation of each extraction technique because the study of each technique does not require the presence of these elements. Moreover, our proposed technique relies on the pad capacitance values extracted from pinch-off measurements; which means that pad capacitances are known to the main procedure of our proposed

technique. However, of course, we will include them if the technique is going to be applied to actual data.

Table 4.1. MESFET model parameters for a hypothetical device.

R_g (Ω)	R_d (Ω)	R_s (Ω)	L_g (pH)	L_d (pH)	L_s (pH)	C_{gs} (fF)	R_i (Ω)	C_{gd} (fF)	g_m (mS)	τ (ms)	g_{ds} (mS)	C_{ds} (fF)
6.5	4.93	2.35	89	91	2	504.3	0.5	31.41	62.52	2.32	1.067	51.39

It is relevant to state that the S-parameters obtained from the assumed model would be clean and would not have the measurement errors and noise typically present in actual data. To make our verification realistic, noise/errors should be introduced to the hypothetical model used. But first, we need to examine type of errors and noise present in actual measured S-parameters of MESFET devices. Network-analyzer measurements experience three types of errors [35]: systematic errors, random errors, and drift errors.

The systematic errors are stable and repeatable because they result from imperfections in the equipment and its components. These errors can be reduced by measurement calibration. The random errors are non-repeatable and cannot be characterized because they result from unpredicted and random conditions; they are due to trace noise, noise floor, cable repeatability, and connector repeatability. This type of errors cannot be corrected by measurement calibration, however averaging can reduce the random errors. Sotoudeh et al. [36] confirmed this postulate by doing measurement statistical analysis on a simulated network analyzer model to show that the real and imaginary parts of the measurements almost follow Gaussian distribution. Thus, simple averaging is an effective way to reduce such errors. The drift errors are time-related errors because they result from time dependent conditions such as temperature, pressure, humidity, and other environmental variations. These errors drift both the frequency and the measured parameters; and so measurement calibration does not correct drift errors. However, these errors can be reduced if the network-analyzer is warmed-up to the steady state temperature since temperature is the primary factor for drift errors.

The limits of measurement uncertainty can be estimated using some complex equations [35]. The phase of the errors can be any value between -180° and $+180^o$. The error distribution might be Gaussian, but it is no longer Gaussian after averaging. The network analyzer is automated to average multiple readings at the same measurement. For this reason, the simulated S-parameters of the hypothetical device are perturbed by noise to emulate the unavoidable measurement errors; and we assumed for simplicity that the noise has uniform real and imaginary distribution whose limits are (+/-0.5%).

The S-parameters of the hypothetical device are shown in Figure 4.1 as the "Ideal data". The noisy data is also displayed in the same figure. Both the ideal (noiseless) and noisy data will be used in the verification process to study the effect of the added noise on the model extraction scheme. Moreover, the S-parameters are calculated over frequency range 0.2-12.2 GHz to be consistent with the actual device measurements, as shown in Figure 4.2.

The actual S-parameter data was measured for a GaAsTEK 0.8x300 μm^2 MESFET. GaAsTEK is a unit of ITT industries located in Roanoke, Virginia. The gate length and width are 0.8 μm and 300 μm, respectively. Figure 4.2 shows the measured S-

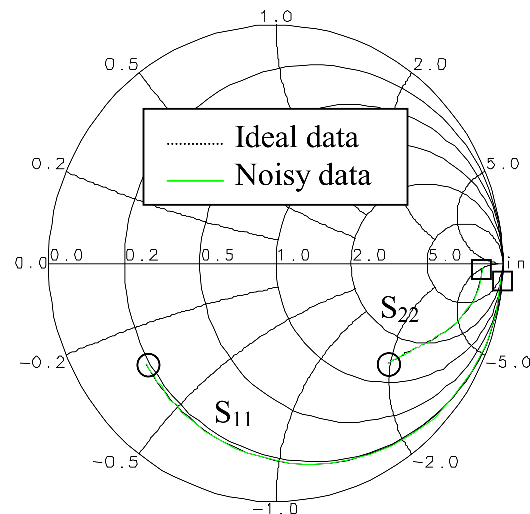

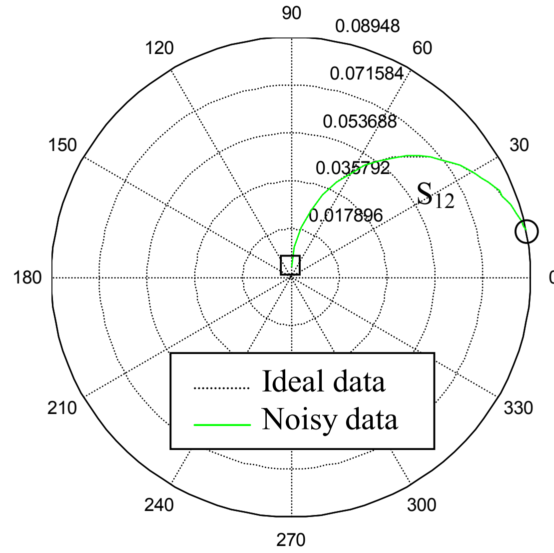

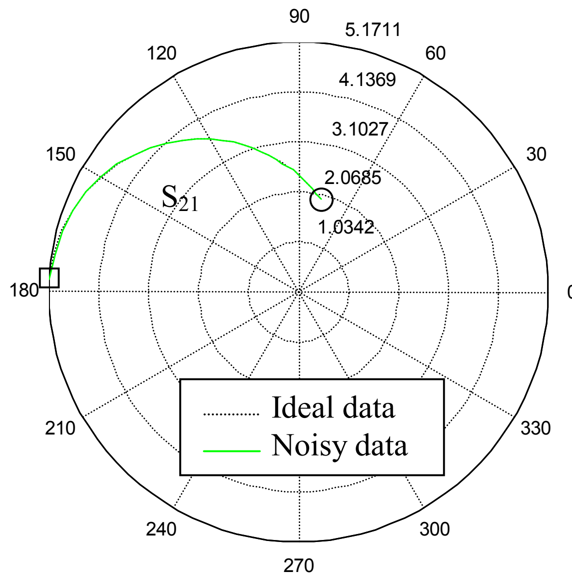

Figure 4.1 S-parameters of the hypothetical model for ideal and noisy data; the square indicates the starting frequency 0.2 GHz while the circle indicates the ending frequency 12.2 GHz.

parameters of this device at V_{gs}=-1.2v and V_{ds}=3v. The technician staff at GaAsTEK did the measurements and we relied on the information they supplied us pertaining to the device geometry and properties.

4.2 Shirakawa's Method:

Shirakawa's method was applied to both the ideal and noisy S-parameters of the verification MESFET model. The ideal data shows good convergence towards the correct solution for all parameters, although there is no normalization factor in the original objective function of Shirakawa equation (3.41) to confine all errors within the same order of magnitudes. This proves that all contributing errors in the objective function have only one minimum at the optimum solution. When Shirakawa's method was applied

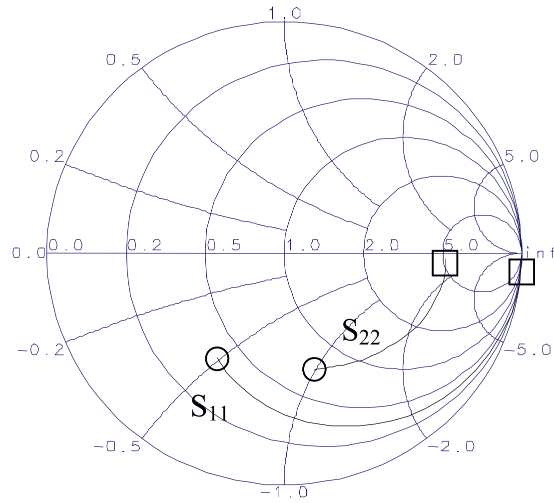

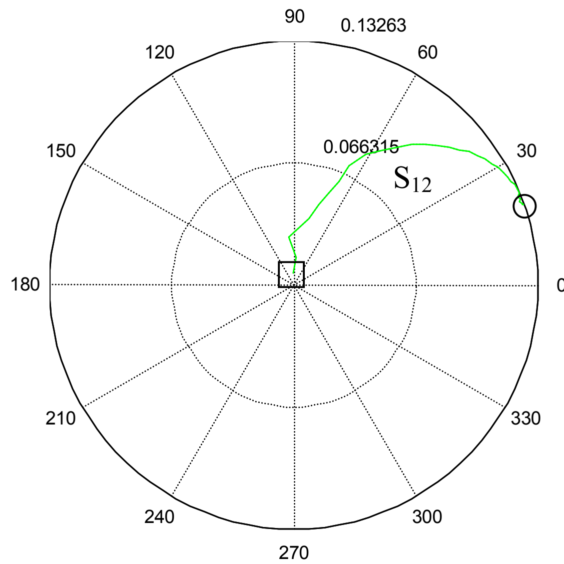

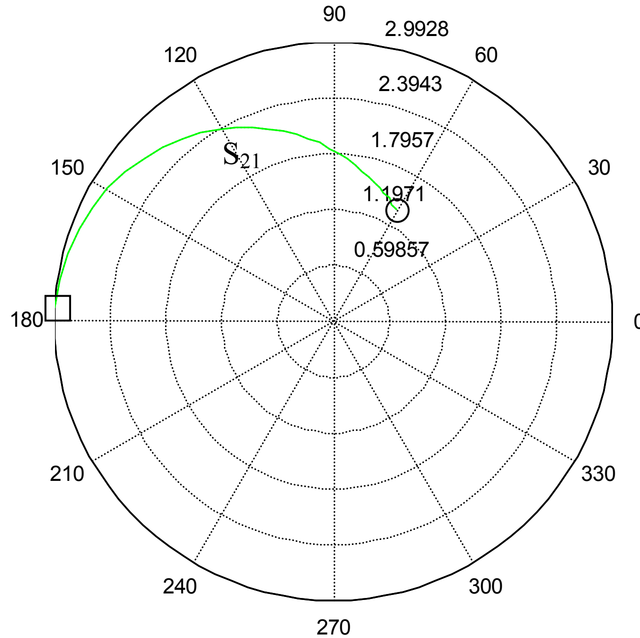

Figure 4.2 Measured S-parameters of GaAsTEK 0.8x300 μm^2 MESFET at V_{gs}=-1.2v and V_{ds}=3v; the square indicates the starting frequency 0.2 GHz while the circle indicates the ending frequency 12.2 GHz.

to the noisy data, the solution of the optimization parameters was erroneous if zero initial values were used, see Table 4.2. However, if the initial values were the same as the optimum solution, then the optimizer maintained the optimum solution. This phenomenon suggests that when noisy data is used, the objective function seems to have some local minimums. Thus, depending on the initial values, the final solution may be determined at the closest minimum to the initial values.

Table 4.2 Shirakawa's solution for noisy data with zero initial conditions.

Parameter	R_g (Ω)	R_d (Ω)	R_s (Ω)	L_g (pH)	L_d (pH)	L_s (pH)
Values	16	1.9	7.15	89	65.9	15.5
Err%	-146	61	-204	0	28	-675

The error percentage (Err%) of a variable can be defined as:

$$Err\% = \frac{Actual - Calculated}{Actual} x100 \qquad (4.1)$$

In our efforts to improve the objective function sensitivity to all intrinsic parameters, we changed the normalization factor to be matched with equation (3.49). We made further investigation and sensitivity analysis for the objective function to locate the weakness points in Shirakawa's method. Such weakness points lead to incorrect solutions. Changing the normalization factor does not result in significant improvement in solution extracted from noisy data.

The objective function sensitivity analysis is depicted in Figure 4.3. In This figure, the elementary errors of the objective function are plotted versus R_g around the optimum solution as an example. The objective function sensitivity analysis of the other optimization variables shows similar results. It is noticed from this plot that errors of R_i, and g_{ds} are dominating the objective function although the low frequency data points of R_i are removed because of the big error associated with them. τ also shows significant error for some optimization variables. In addition, the minimum of the optimum solution is slightly deviated for the noisy file. One may think that the optimizer should locate this deviated optimum solution. In fact, the optimizer located a wrong minimum when noisy data was used. This solution is tabulated in Table 4.3. Comparing the objective function values at both this wrong solution and the correct solution, we found out that the objective function value at the correct solution is larger than that at the wrong solution. This interprets why the optimizer slipped over the correct solution, where a local minimum may exist, to a global minimum. Moreover, it is obvious that adding noise to the measured data moves the global minimum from the correct solution point to a wrong solution point.

Some interesting points can be observed from Table 4.3. The error percentage of all resistive elements is relatively large, especially that of R_i, as well as that of L_s. The most accurate elements are the capacitance elements, except C_{gs}, as well as L_g and L_d. C_{gs} is

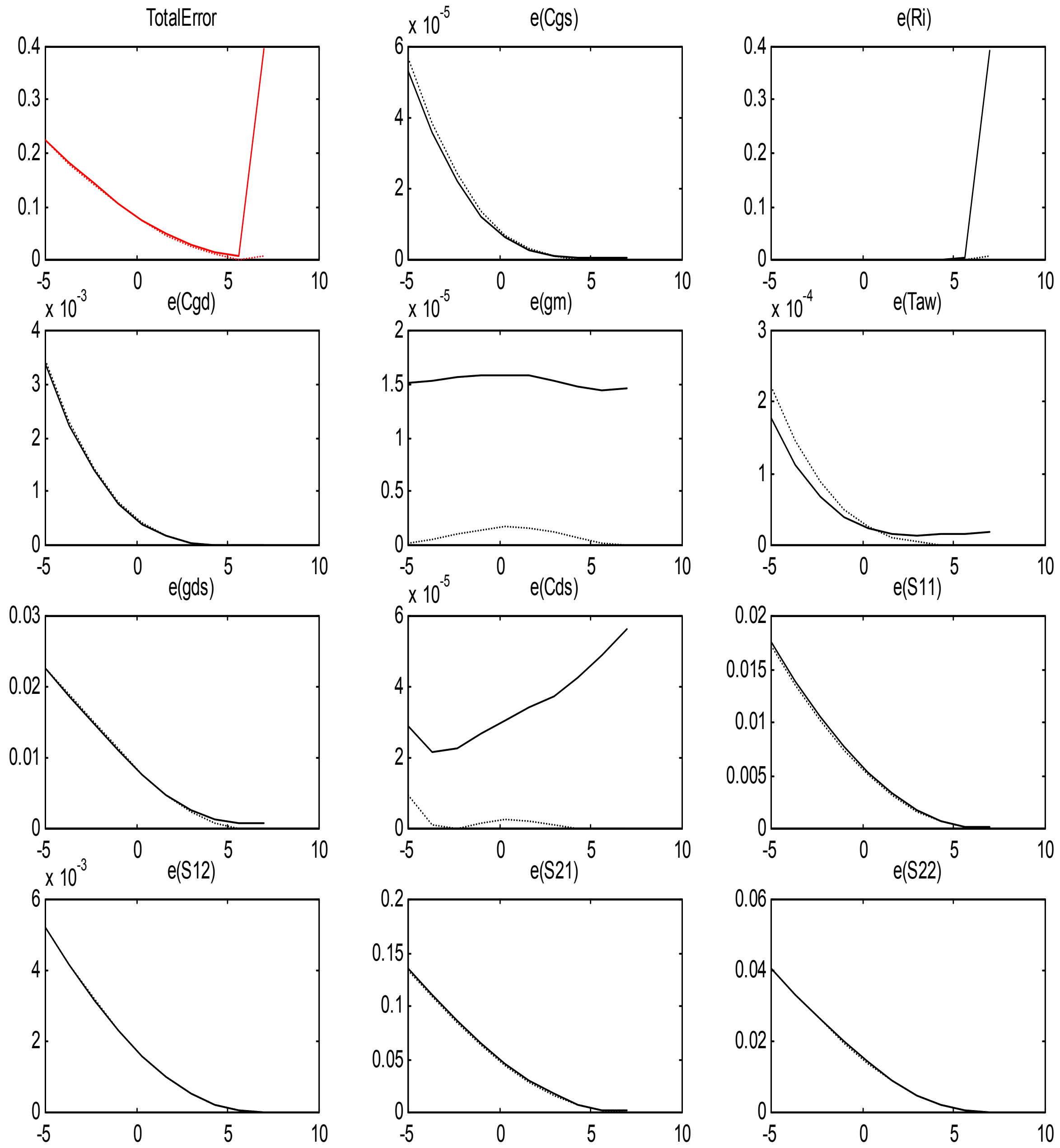

Figure 4.3 Objective function as well as its elementary components versus R_g plotted around the optimum component of R_g=6.5 Ω; dashed curve indicates ideal data is used while solid curve indicates noisy data.

not as accurate as other capacitance elements because it is calculated simultaneously from the same data of R_i, the most inaccurate element. The above observations make sense to some extent because the resistance values in the model are much less than the capacitance

impedance values. This is more confirmed at low frequency points. As a result, all capacitance elements can be easily extracted with a high degree of confidence.

Table 4.3 Complete solution set using noisy data.

Parameter	Value	Err%	Parameter	Value	Err%
R_g (Ω)	-1.5	123	R_i (Ω)	13.8	2660
R_d (Ω)	7.92	-61	C_{gd} (fF)	33.7	-7.29
R_s (Ω)	-3.2	236	g_m (mS)	46	26
L_g (pH)	92	-3.37	τ (ms)	2.09	10
L_d (pH)	92	-1.1	g_{ds} (mS)	0.79	26
L_s (pH)	3.87	-94	C_{ds} (fF)	49.31	3.9
C_{gs} (fF)	360	29			

Another trick was tried to help the optimizer finding out the correct solution. Constraints were added to avoid negative values of the optimization parameters. Unfortunately, those constraints failed to guide the optimizer to locate the correct solution. The reason is, the optimizer enforces those elements, which would have negative values if the constraints do not exist, to have as small values as possible, almost around zero. The optimizer again tried to decrease the objective function towards the global minimum and since there was a penalty function for negative values, it located a minimum as close to the global minimum as possible.

Thus, it is not recommended, at this stage, to impose any constraints on the optimization variables, rather it is recommended either to modify the objective function so that it has only one global minimum or to change the optimization technique.

4.3 Modeling-Optimization Problem and Solution:

We need to further investigate noise effects on the optimization process so that we can identify the problems; and hence solutions may be suggested to overcome such problems. Measured S-parameters were converted into intrinsic Y-parameters (Y_{int}) for both ideal

and noisy data. S-parameters were converted into Z-parameters, then the extrinsic Z-parameters were subtracted resulting in intrinsic Z-parameters, and finally the intrinsic Z-parameters were converted into Y_{int}. Figure 4.4 shows the real and imaginary parts of Y_{int} for both ideal and noisy data at the optimum solution. The intermediate conversions plots, which are not shown here, reveal that as the conversion goes from one level to another, the noise level becomes larger. In other words, the conversion process amplifies noise.

The real parts of Y_{int11}, Y_{int12}, and Y_{int22} have significant amount of noise as shown in Figure 4.4. Those components are the most sensitive parts to noise. R_i and g_{ds} are calculated from the real parts of Y_{int11} and Y_{int22}, respectively. This clarifies why R_i has the largest percentage error in Table 4.3. In addition, one might notice that these noisy components are used to calculate the resistive elements of the intrinsic model.

Figure 4.4 also gives some insight to what is going on during the optimization process. It shows how big the effect of the measurement errors on the intrinsic Y-parameters is. As a result, the error level may overwhelm the original signal. Under this condition of big error level, it might become too difficult to extract the resistive elements of the model in the presence of the dominating capacitance impedances. The reason is that the resistive values might become comparable to the noise level. For example, assume we have impedance of (5-j1000) ohms, which consists of resistance of 5 ohms and capacitive impedance of 1000 ohms. Consider noise of 1% of the impedance magnitude is to be added to both real and imaginary parts as a result of a series of conversions. The final impedance will be (15-j990) ohms. The percentage error of the resistance is 200% while that of the capacitive impedance is only 1%. This interpretation may be valid for the proposed model under this optimization algorithm. In other words, if another optimization algorithm is used or the model is changed, the effect of the noise might become less pronounced.

We also studied the effect of the different components whose errors contribute to the objective function. Figure 4.5 shows the histogram of all intrinsic elements calculated from the ideal and noisy S-parameters at the optimum solution. The horizontal axis

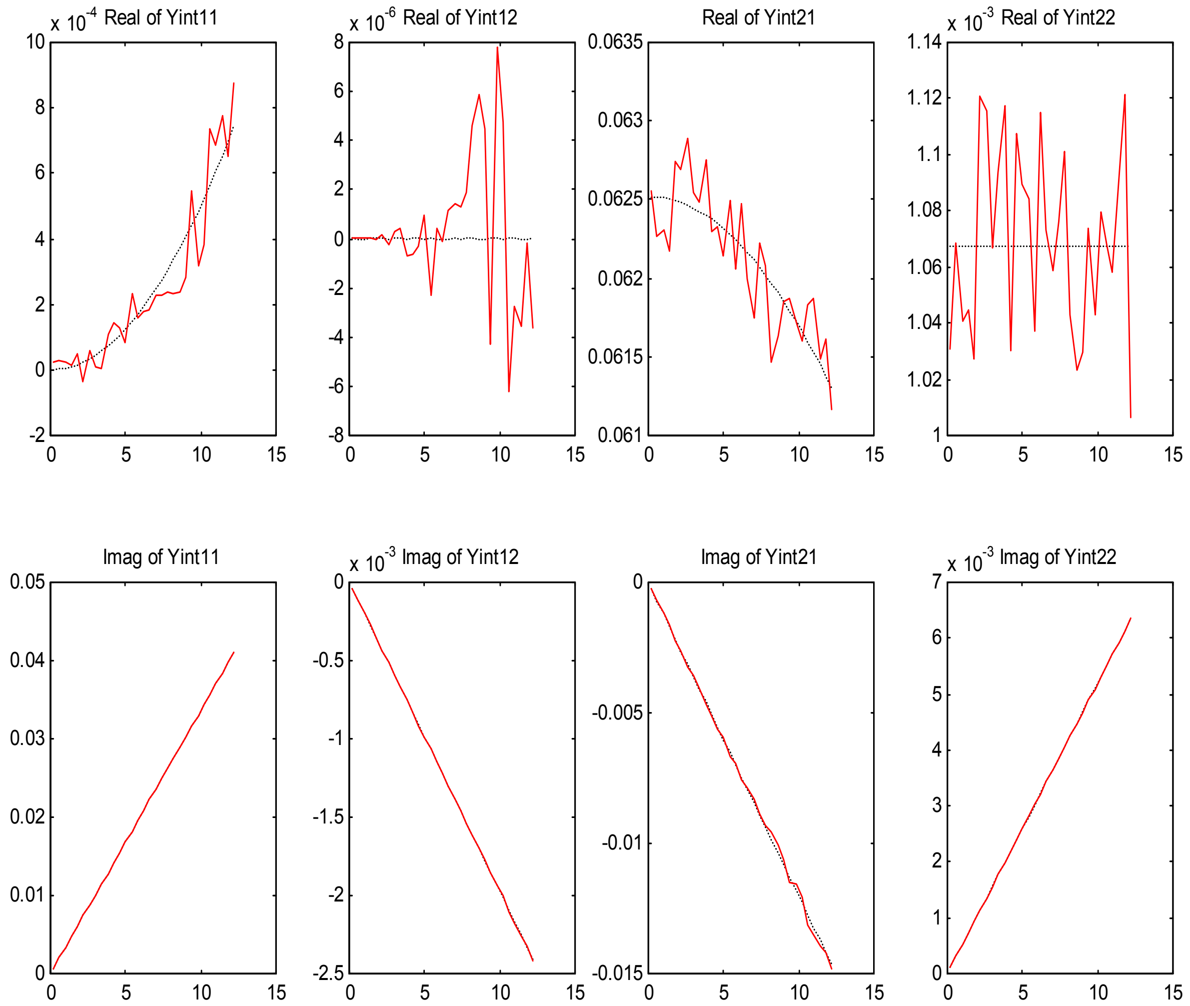

Figure 4.4 The real and imaginary parts of Y_{int} versus frequency (0.2-12.2 GHz) for both ideal and noisy data at the optimum solution; red curve indicates results of the noisy data while black curve indicates results of the ideal data.

represents possible values of an element while the vertical axis represents number of repetitions over the whole frequency range within a specific value range. The histograms of R_i, g_{ds} and τ explain non-normal distribution characteristic. The normal distribution characteristic is important for a parameter to be defined by l_2-norm in the objective function and to calculate its value as a simple averaging.

As a conclusion, it is not wise to use R_i, g_{ds}, and τ error functions in l_2-norm in the objective function. We may either change their error format in the objective function or

drop out their contribution in the objective function. We decided to drop out their contribution in the objective function. Moreover, those elements are calculated by curve fitting to fit the corresponding branch impedances, as shown in Appendix B.

Up till this point, we have not resolved the problem of the global minimum deviation under the effect of measurement errors. The first solution, which might come to our mind, is to get rid of the measurement noise or smoothing out the measured S-parameters.

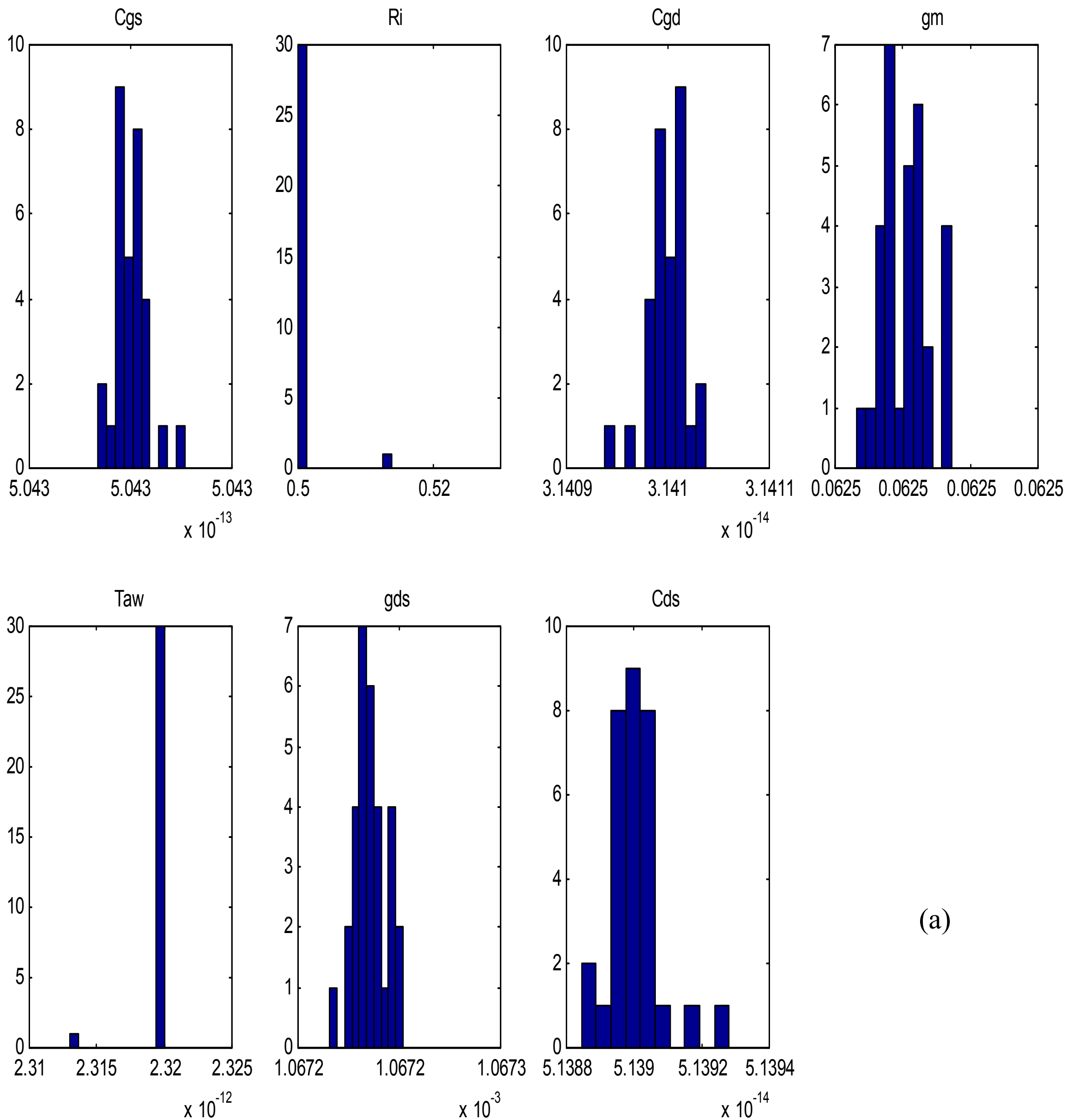

(a)

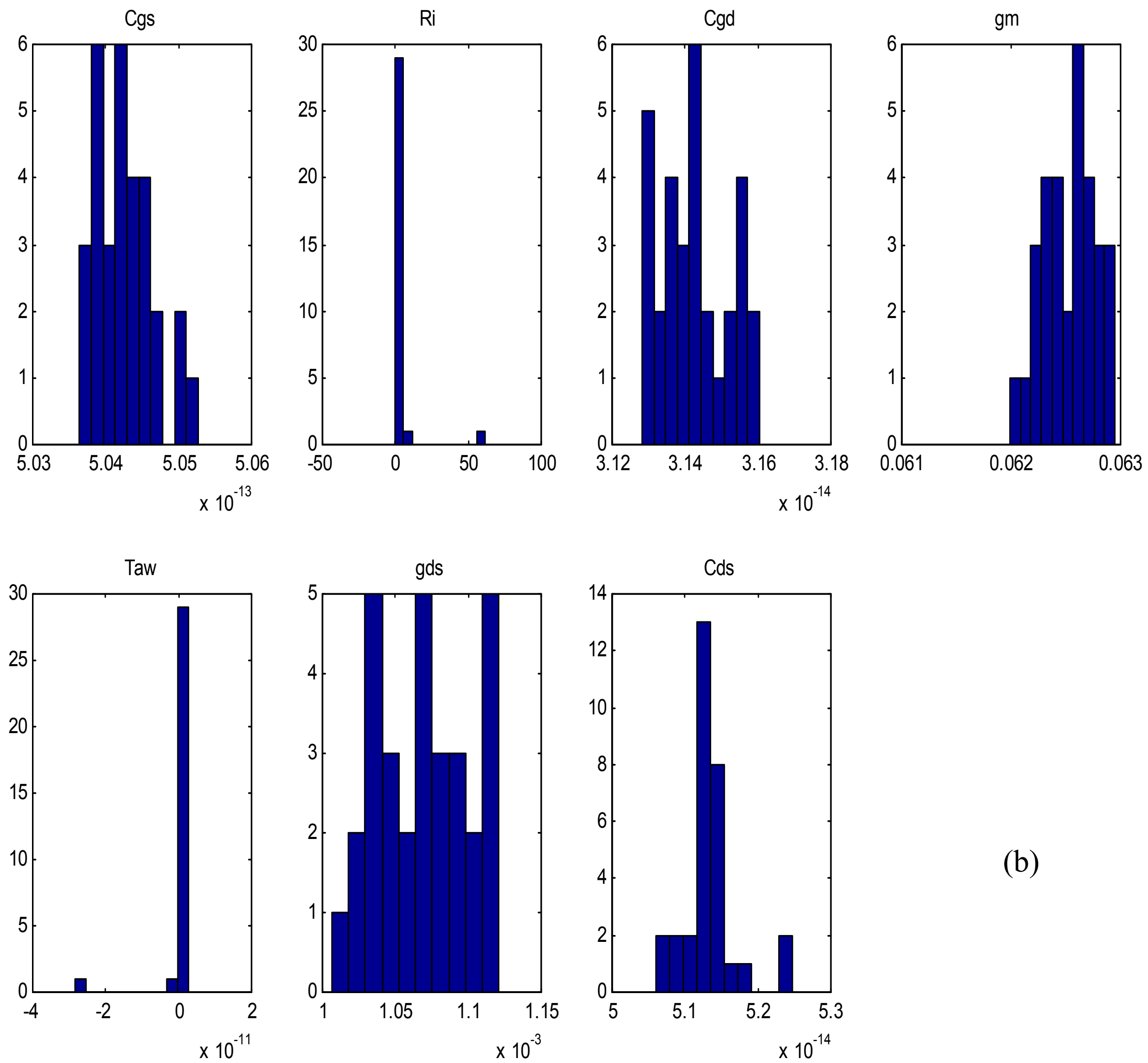

Figure 4.5 Histogram of all intrinsic elements calculated at the optimum point: (a) Ideal data is used, (b) Noisy data is used.

Two methods were used to smooth out S-parameters: Cepstrum and polynomial curve fitting. Unfortunately, both methods failed to restore the original S-parameters.

Cepstrum is a method, which is used in signal processing to separate two mixed signals from each other. The two signals must have different frequency bands. Cepstrum method calculates the Fourier transform of the mixed signal, and then filters out the low frequency signal to isolate it. Inverse Fourier transform should be carried out to obtain the time domain signal. The Cepstrum method was applied to the noisy S-parameters of

the verification model to extract the original signal, but it failed to extract it because the frequency band of the noise interfered with the high frequency component of the original signal. It was applied not only to noisy S-parameters but also to the transformed Z-parameters and intrinsic Y-parameters. In all cases, the noise components are not separable from the original signal components.

The other alternative is to fit a polynomial to the noisy S-parameters. This method also failed to extract the original S-parameters although we tried to fit a polynomial whose degree was as big as fifteen. The reason is that any small variation in S-parameters data results in large variation in calculating the resistive values of the model and thus the optimizer locates a wrong solution. Other curve fitting methods were tried such as doing curve fitting for the real parts of the intrinsic Y-parameters at each iteration of the optimization process. Many function formats were tried to fit the real part of Y_{int11}.

For the above reasons, we had to change the optimization method itself. As we mentioned before, all resistive elements, in the model, have the largest relative errors. This guides us to a possibility that the resistive elements in the circuit may be redundant over this frequency range and measurement error. In other words, this model does not represent the minimal circuit for this frequency range [17]. The minimal equivalent circuit for a specific frequency range and measurement set can be defined as the circuit with the minimum number of elements that can represent the measured data within a specified error tolerance.

The optimizer ran using the noisy S-parameters while one of the resistive elements was held constant at its correct value. The optimizer was able to locate the correct solution within a reasonable error tolerance. This observation confirms our conclusion that the resistive elements are linked together through two types of relationships: strong and weak. The strong relationships are those in which the resistive elements are prominent, in turn the effect of the frequency range or measurement error is insignificant in these strong relationships. Some authors [27] reported that there is a strong relationship between R_g, R_i, and R_s. In contrast, the weak relationships are those in which the resistive elements

are insignificant so that their weight in the equation is comparable to the measurement error.

Consequently, some of the resistive elements constraints become loose under the effect of the measurement noise. To compensate for these loose conditions, other information or constraints should be imposed. This justifies why the optimizer can locate the correct solution if one of the resistive elements is known. Table 4.4 shows the solution when R_g is held constant at its correct value R_g=6.5 ohms, in addition, Table 4.5 shows the solution when R_i is held constant at its correct value 0.5 ohms.

Table 4.4 The solution when R_g=6.5ohms.

Parameter	Value	Err%	Parameter	Value	Err%
R_g (Ω)	6.5	0	R_i (Ω)	0.517	-3.4
R_d (Ω)	4.95	-0.41	C_{gd} (fF)	31.4	0.032
R_s (Ω)	2.365	-0.64	g_m (mS)	62.6	-0.128
L_g (pH)	89.022	-0.025	τ (ms)	2.313	0.302
L_d (pH)	92.6	-1.76	g_{ds} (mS)	1.0673	-0.028
L_s (pH)	1.794	10.3	C_{ds} (fF)	51.38	0.019
C_{gs} (fF)	505	-0.1388			

Table 4.5 The solution when R_i=0.5ohms.

Parameter	Value	Err%	Parameter	Value	Err%
R_g (Ω)	6.5	0	R_i (Ω)	0.5	0
R_d (Ω)	4.956	-0.53	C_{gd} (fF)	31.4	0.03
R_s (Ω)	2.37	-0.851	g_m (mS)	62.6	-0.128
L_g (pH)	89.03	-0.034	τ (ms)	2.317	0.129
L_d (pH)	92.36	-1.49	g_{ds} (mS)	1.0675	-0.047
L_s (pH)	1.819	9.05	C_{ds} (fF)	51.4	-0.0195
C_{gs} (fF)	505	-0.139			

The solutions of both cases show very good agreement with the actual optimum point within a reasonable tolerance. Although anyone of the resistive element should theoretically be held fixed at its correct value, it is not feasible to assume fixed value for one of the intrinsic resistive elements. The intrinsic resistive elements are usually bias dependent. Moreover, both R_d and R_s are also bias dependent, however, their dependence on bias voltage is weak and can be ignored in most cases. Consequently, the most convenient element which can be assumed constant is R_g. Fortunately, R_g can be calculated from S-parameter measurements at different bias points as explained in section 3.5.1.

4.4 Ooi's Method:

The theoretical bases of Ooi's method were explained in detail in section 3.4.3. Ooi's method is very similar to Shirakawa's method except that R_g is not an optimization parameter. It is calculated in terms of the other optimization parameters. Thus, the number of the optimization parameters decreases to five instead of six, and in contrast the number of objective error function elements increases to eight instead of seven.

Although this method shows reduction in the number of the optimization variables, it does not circumvent the problem associated with Shirakawa's method. The Redundancy of the resistive elements still exists under the effect of limited frequency band and measurement error; the same implicit weak relationships of the resistive elements are pronounced throughout the computational work. The Ooi's method was able to locate the correct solution with zero initial values using the ideal data. In contrary, it could not find the correct solution using the noisy data even if the initial value set was the correct solution.

Therefore, it is not enough to reduce the number of optimization variables it is most important to afford new constraints or information on the resistive elements. Table 4.6 shows the same wrong solution for the model parameters using Ooi's method.

Table 4.6 The solution set using Ooi's method with noisy data.

Parameter	Value	Err%	Parameter	Value	Err%
R_g (Ω)	3.45	46.9	R_i (Ω)	5.3	-960
R_d (Ω)	5.186	-5.19	C_{gd} (fF)	32	-1.88
R_s (Ω)	0.257	89	g_m (mS)	55	12
L_g (pH)	89.5	-0.56	τ (ms)	2.31	0.431
L_d (pH)	90	1.099	g_{ds} (mS)	0.95	10.97
L_s (pH)	3.097	-54.85	C_{ds} (fF)	50.14	2.43
C_{gs} (fF)	440	12.75			

4.5 Lin's Method:

This method is different from both Shirakawa's method and Ooi's method in many aspects. Lin's method uses l_1-norm for the objective function. It also includes only the discrepancy between the calculated and measured S-parameters. It does not include any information about the intrinsic elements in the objective function. The optimization method is an improved simplex method, which is a non-gradient optimization technique. It uses frequency-weighted curve fitting technique to fit the intrinsic branch admittances so that the intrinsic parameters can be calculated.

Moreover, Lin's method can be considered as initial-value sensitive technique that if the initial values are far away from the correct solution the optimizer may converge to a wrong local minimum. We used FMINS() function of MATLAB to test Lin's method. FMINS() uses the simplex search algorithm of Nelder and Mead [37]. We did not need to generate initial values for the optimization parameters because Lin's method was carried out on the hypothetical S-parameters data where the solution set was known priory.

The solution of Lin's method is shown in Table 4.7. The data is the hypothetical noisy S-parameters and the initial value set is the same as the correct solution. Comparing this solution with the solution of Table 4.4, one may notice that most of the resistive element

errors are larger than that of Table 4.4. The error of R_i has risen to -30%, which is relatively big.

Table 4.7 Lin's method solution for the noisy data.

Parameter	Value	Err%	Parameter	Value	Err%
R_g (Ω)	6.4	1.54	R_i (Ω)	0.653	-30.6
R_d (Ω)	5.335	-8.215	C_{gd} (fF)	31.4	0.032
R_s (Ω)	2.35	0	g_m (mS)	62.58	-0.096
L_g (pH)	88.56	0.494	τ (ms)	2.273	2.026
L_d (pH)	94.5	-3.85	g_{ds} (mS)	1.0646	0.225
L_s (pH)	1.67	16.5	C_{ds} (fF)	51.5	-0.214
C_{gs} (fF)	504	0.06			

In addition, we tested the objective function value around the obtained solution to discover some points at which the objective function value is less than its value at the obtained solution in Table 4.7. This indicates that the obtained solution by Lin's method is a local minimum and not a global minimum. The philosophy of Lin's method is to find an initial values set for the optimization parameters as close to the correct solution as possible, and then the optimizer should look for the correct solution in the neighborhood of the initial values set. The correct solution supposedly lies at a local minimum. The initial values can be generated from S-parameters data measured at a passive pinch-off bias point (V_{ds}=0 and V_{gs}<-|V_p|), as shown in section 3.2.2.

This observation about Lin's method was confirmed by applying it using the actual device S-parameter data, Figure 4.2. Zero initial values were assumed. The obtained solution had some negative resistive values. This is attributed to the wrong choice of the initial values. The initial values should be calculated from S-parameters measured at a passive pinch-off bias point.

4.6 Results of the Novel Systematic Parameter-Extraction Technique:

We will handle the results of our proposed technique described in section 3.5 throughout this section. Our proposed technique is composed of two sequential stages. Five parameters are calculated at first stage in preparation for the next stage. In the first stage, cold-measurements along with pinched–off device measurements are used to extract values of L_d, L_s, C_{pg}, C_{pd}, and R_g. In the second stage, all other model parameters are extracted at normal bias conditions. We will explain the results of the first stage over the next three subsections. The fourth subsection is allocated for the results of the second stage.

4.6.1 Cold-Measurement Results:

Cold S-parameter measurements are used to extract both L_d and L_s. The algorithm used here comprises a corner stone for the first stage of our proposed technique. S-parameters are measured at zero drain-source bias voltage (V_{ds}=0). The gate-source bias voltage is equal to zero (V_{gs}=0) so that the condition (3.32) is satisfied. The extraction process was described in detail in section 3.3. Figure 4.6 depicts the imaginary parts of Z-parameters for the actual GaAsTEK 0.8x300 μm^2 MESFET. The imaginary parts of Z-parameters are in good agreement with the theoretical calculations in equation (3.38). Imaginary parts of Z_{12}, Z_{21}, and Z_{22} are linearly proportional to the frequency over a low frequency range (0.2-7.8 GHz) while imaginary part of Z_{11} exhibits nonlinear relationship according to equation (3.38a). Moreover, imaginary part of Z_{12} is almost equal to imaginary part of Z_{21}.

L_g, L_s, and L_d were calculated by curve fitting and following equation (3.38). Different frequency ranges were used in curve fitting to study the effect of frequency range on the accuracy of extracted values. Table 4.8 shows the results of curve fitting for the extracted parameters L_s, L_d, and L_g. L_s and L_d were calculated to a high degree of accuracy and confidence as shown in the table. They are insensitive to frequency range variation as long as the frequency range is still in the low frequency band. In contrast, L_g shows large

variations between different frequency ranges although weighted-frequency curve fitting are used. Weighted frequency curve fitting enhances the high frequency data points. Therefore, we are less confident about the calculation of L_g.

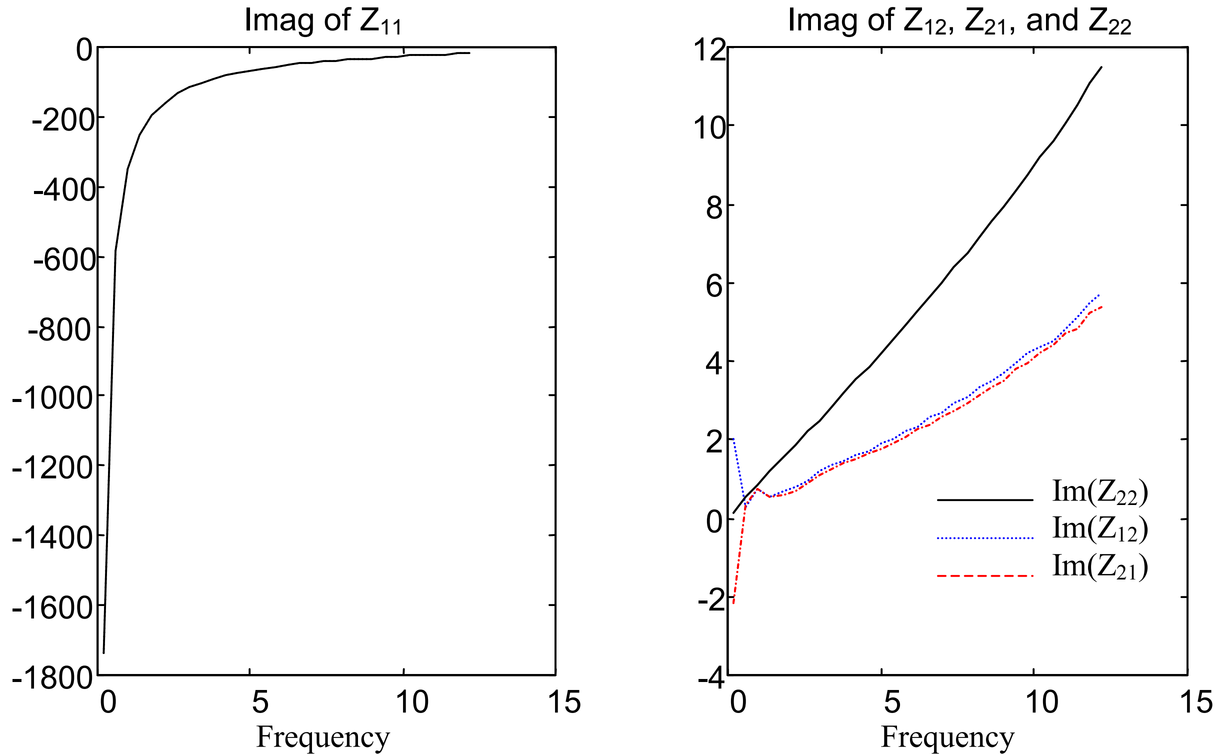

Figure 4.6 Imaginary parts of cold-measurement Z-parameters for 0.8x300 μm^2 MESFET.

Table 4.8 L_s, L_d and L_g extracted at different frequency ranges.

	0.2-5 GHz	0.2-7.8 GHz	2.6-7.8 GHz
L_s (pH)	59.0	59.66	59.6
L_d (pH)	74.7	76.0	76.2
L_g (pH)	42.0	65.8	73.8

This variation can be justified that the imaginary part of Z_{11} is composed of two impedances connected in series: inductive impedance of L_g and capacitive impedance of

"C". The capacitive impedance is dominating the imaginary part of Z_{11} as shown in Figure 4.6 that the imaginary part of Z_{11} is highly negative. The inductive contribution of L_g takes effect at higher frequencies. As a result, the value of L_g, extracted over the frequency range (2.6- 7.8 GHz), is supposedly the most accurate value. However, it is recommended to extract the value of L_g from pinch-off measurements as explained in the next section.

The solution listed in the third column of Table 4.8 will be used in the following section to calculate the pad capacitances and gate resistance.

4.6.2 Pinched-off Device Measurement Results:

The pinched-off device measurements are used to extract values of pad capacitances C_{pg} and C_{pd} along with the gate resistance R_g. This is the second corner stone for the first stage of our proposed technique. The evolution of the final extraction process mentioned in section 3.2.3 has gone through a few steps. The frequency range of S-parameters data was 0.2-12.2 GHz. We started with Lin's method, which is explained in section 3.2.2, to extract the parasitic elements and pad capacitances. Unfortunately, the extracted values had unacceptable big errors over the aforementioned frequency range.

We modified Lin's method so that the optimization variable is C_{pd} only where C_{pg} is known priory. We calculated C_{pg} using the same method mentioned in section 3.2.1. Again, this modification did not help to resolve the main problem of Lin's method that capacitive impedances overwhelm inductive impedances. For this reason, we decided to calculate L_d and L_s from cold measurements and then to incorporate them into the extraction process as shown in section 3.2.3 to show good preliminary results for pad capacitances and gate resistance.

The procedure is even evolved to incorporate both C_{pg} and C_{pd} as optimization variables along with the condition that C_{gs} and C_{gd} are equal. The reason is, we do not want to rely on the approximate values of C_{pg}, C_f, and C_{pds}. Our study showed that any

minor change in C_{pds} or C_f resulted in a big error in C_{pd}. Consequently, we used the same constraint implied in this approximation, that C_{gs}=C_{gd}, with C_{pg} and C_{pd} as optimization variables. Finally, in order to make our technique more accurate and insensitive to the frequency band, the objective function is modified to include the errors of the capacitive components as in equation (3.26). In the following paragraphs, we will discuss the results of these development trials.

Hypothetical S-parameters of a pinched-off MESFET device model was used to verify the extraction methods. The model of a MESFET device at pinch-off voltage is shown in Figure 3.5. The hypothetical model-parameters are listed in Table 4.9 [28]. These model parameters were used to generate two sets of hypothetical S-parameter data: ideal and noisy data over the frequency range 0.2-12.2 GHz. The noisy data was generated from the ideal data by adding (+/-0.5%) of uniform noise to both real and imaginary parts.

Table 4.9 Hypothetical model-parameters at pinch-off voltage.

R_g (Ω)	R_d (Ω)	R_s (Ω)	L_g (pH)	L_d (pH)	L_s (pH)	C_g (fF)	C_d (fF)	C_s (fF)	C_{pg} (fF)	C_{pd} (fF)
2.18	1.26	0.56	193.8	199.6	31.0	400	200	200	31.9	25.9

Figure 4.7 shows a 3D plot of the objective function (3.22) for the two data sets: ideal and noisy in case of Lin's method where both C_{pg} and C_{pd} are optimization parameters. While this plot shows good agreement between the minimum and the correct solution of the pad capacitances for the ideal data, it obviously shows serious shift in the minimum point under the effect of noise. In addition, it reveals an important feature of the objective function that it has only one minimum. Consequently, it does not matter what initial values are used.

To confirm the mentioned observations, the Lin's method was applied to the ideal data with zero initial values. The solution set for ideal data was typically identical to the correct solution. In contrast, when it was applied to the noisy data, the solution set had

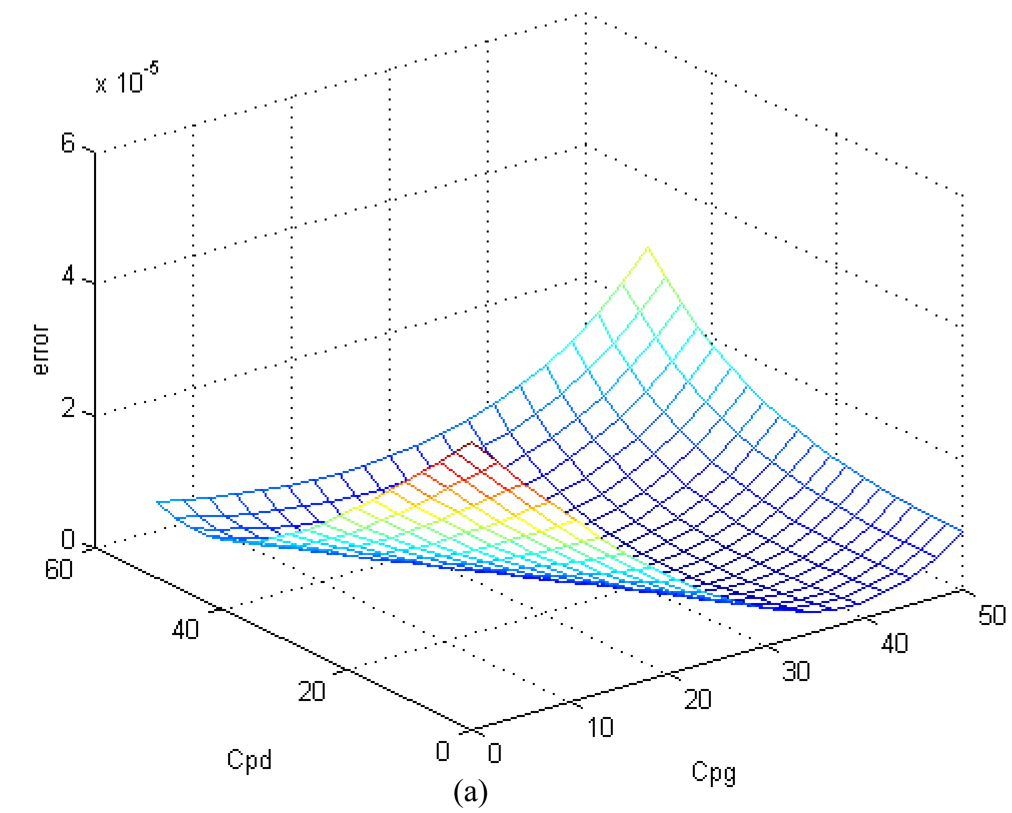

(a)

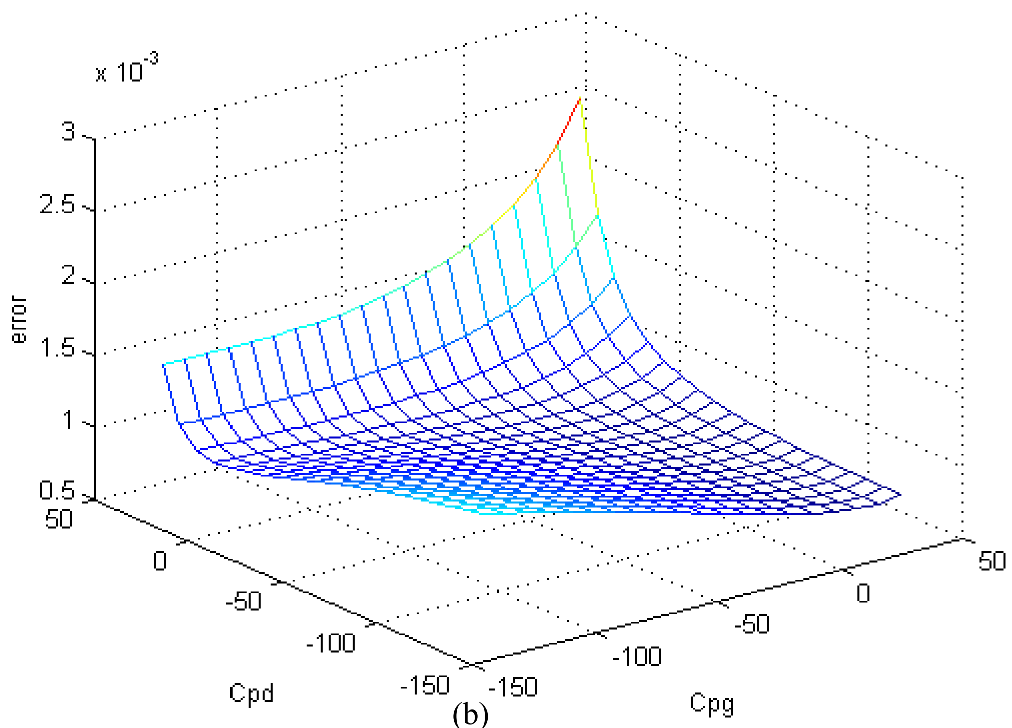

(b)

Figure 4.7 Lin's Objective function versus C_{pg} and C_{pd} of the hypothetical model of Table 4.9: (a) ideal data, (b) Noisy data showing serious shift in the minimum.

large errors as shown in Table 4.10. R_s, L_d, L_s, C_d, C_s, and C_{pd} have relatively the biggest errors. This may be attributed to the big discrepancy between the inductive and the capacitive impedances of the circuit. The inductive impedances are much less than the capacitive impedances. Therefore, their effect may be embedded in the noise leading to multiple solutions depending on the noise.

Table 4.10 The solution set of Lin's method for noisy data.

Parameter	Value	Err%	Parameter	Value	Err%
R_g (Ω)	2.4	-10	C_g (fF)	260	35
R_d (Ω)	0.39	69	C_d (fF)	463	-132
R_s (Ω)	-0.015	103	C_s (fF)	488	-144
L_g (pH)	235	-21	C_{pg} (fF)	27	15.36
L_d (pH)	65	67	C_{pd} (fF)	-111	529
L_s (pH)	-19	161			

This observation was confirmed by extracting the parameters over a limited frequency range (5.4-12.2 GHz). The low frequency range (0.2-5 GHz) was ignored because the inductive impedances are much less than the capacitive impedances over this frequency range. As expected, the parameter errors decreased.

The first modification to Lin's method was carried out hoping the problem might be resolved. The extraction process was carried out over two steps. In the first step, values of C_{pg}, C_{gs}, C_{gd}, and (C_{ds}+C_{pd}) were extracted over a frequency range 0.2-5 GHz using the method explained in section 3.2.1. In the second step, all inductances, resistances, C_{ds} and C_{pd} can be extracted over a frequency range 5.4-12.2 GHz while C_{pd} is the only optimization parameter. Unfortunately, this modification of Lin' method does not resolve the problem and the minimum of the objective function is still deviated under the effect of noise. The objective function is shown in Figure 4.8 for both the ideal and noisy data. C_{pg}, C_{gs}, C_{gd}, and (C_{ds}+C_{pd}) values are assumed to be equal to the ideal values from Table 4.9.

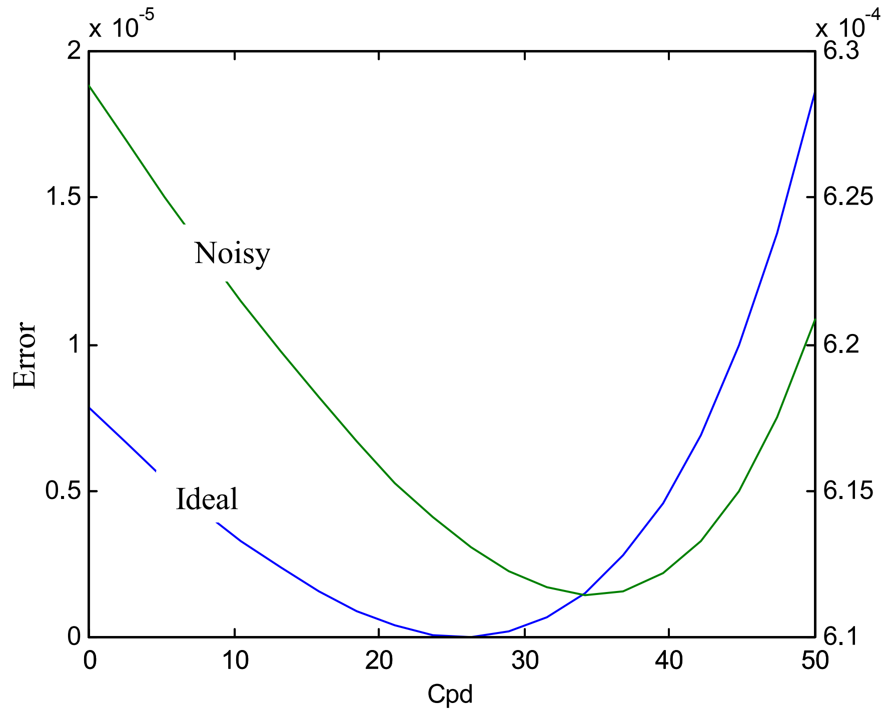

Figure 4.8 Objective function versus C_{pd} for the ideal and noisy data.

Another modification to Lin's method was introduced requiring one inductive element at least to be known. This is one of the basic features of the process explained in section 3.2.3. This method shows good results for the pad capacitances and parasitic resistances. Figure 4.9 plots the objective function for both the ideal and noisy data versus the optimization parameter C_{pd}. The objective function is calculated over the whole frequency range (0.2-12.2 GHz). Both L_d and L_s are fixed at their ideal values while C_{pg}, C_{gs}, C_{gd}, and (C_{ds}+C_{pd}) values are assumed to be equal to the ideal values from Table 4.9. The plot shows good agreement between the minimum of the ideal data and that of the noisy data at the correct solution of C_{pd}.

To further investigate this method, it was applied to the hypothetical noisy data. Table 4.11 lists all element values for the pinch-off model after the extraction process is done. The associated errors of the extracted parameters are very small. It is obvious that the capacitive elements have the least errors because of their dominating contribution to S-parameters. This method proves one of the important clues in the solution that one inductive element at least should be fixed.

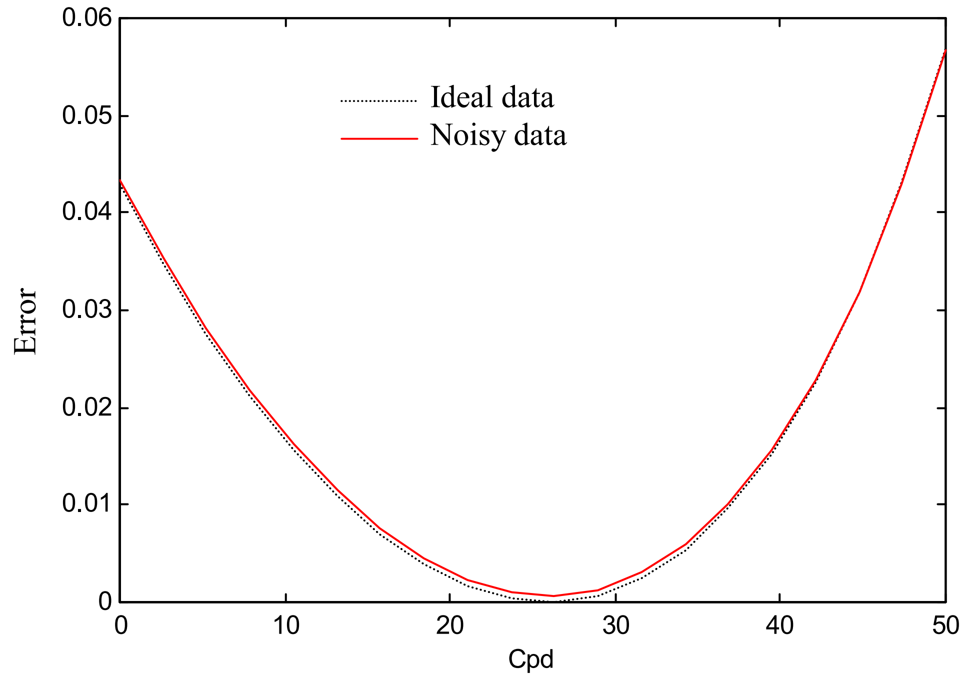

Figure 4.9 Objective function versus C_{pd} showing good minimum agreement between ideal and noisy data; L_d and L_s are known.

Table 4.11 The pinch-off parameters where L_s and L_d are known.

Parameter	Value	Err%	Parameter	Value	Err%
R_g (Ω)	2.15	1.376	C_g (fF)	400.152	-0.038
R_d (Ω)	1.332	-5.714	C_d (fF)	199.924	0.038
R_s (Ω)	0.59056	-5.457	C_s (fF)	199.924	0.038
L_g (pH)	194.583	-0.4	C_{pg} (fF)	31.9	0
L_d (pH)	199.6	0	C_{pd} (fF)	25.94	-0.15
L_s (pH)	31	0			

Although the errors in Table 4.11 are small, in reality the errors should be larger because values of C_{pg}, C_{gs}, C_{gd}, and (C_{ds}+C_{pd}) are not ideally calculated. In contrast, their values are approximations. Our investigation showed that the final results are very sensitive to the accuracy of C_{pg}, C_{gs}, C_{gd}, and (C_{ds}+C_{pd}); minor perturbations in these values show big errors in the other elements. The approximate values of C_{pg}, C_{gs}, C_{gd}, and

$(C_{ds}+C_{pd})$ should practically be estimated over the low frequency range from 3.8 GHz up to 4.6GHz. The low frequency points (0.2-3.8 GHz) should be eliminated because the S-parameter measurements, over this low frequency points, are very noisy and unreliable as shown in Figure 4.10. Figure 4.10 shows C_{pg}, C_f ($C_f=C_{gs}=C_{gd}$), and C_{pds} ($C_{ds}+C_{pd}$) for the actual GaAsTEK 0.8x300 μm^2 MESFET at pinch-off voltage V_{gs}=-2v and V_{ds}=0.

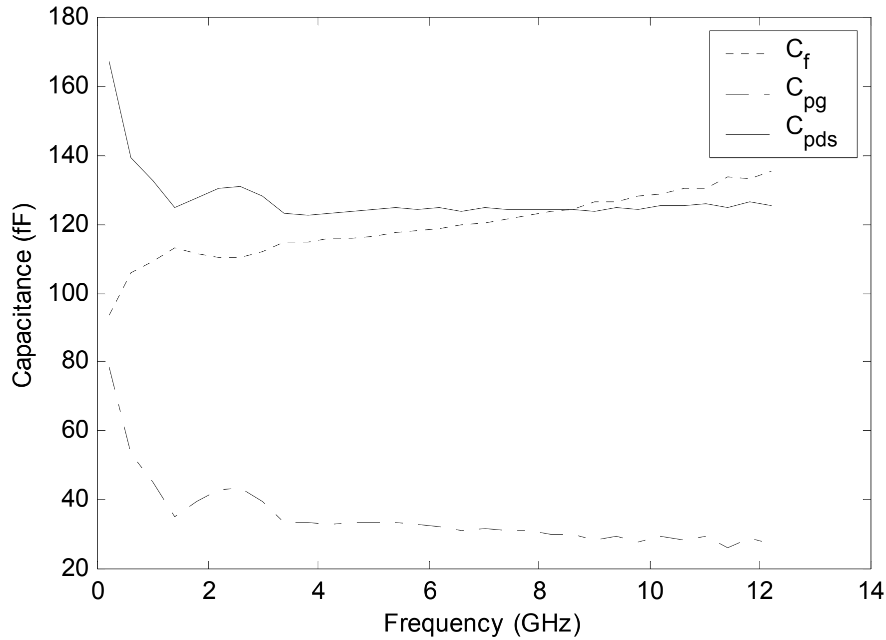

Figure 4.10 Capacitances of the simplified pinch-off model for GaAsTEK 0.8x300 μm^2

The values of C_{pg}, C_f, and C_{pds} are estimated and listed in Table 4.12a for the hypothetical noisy data. The full-model parameters are extracted using these values over the rest of the frequency band (4.6-12.2 GHz). These parameters are listed in Table 4.12b to show big errors, especially for C_{pd}, since C_{pg}, C_f, and C_{pds} have slight deviation from the exact values. As a result, we have to make both C_{pg} and C_{pd} optimization parameters while L_d and L_s are fixed and $C_{gs}=C_{gd}$.

Once again, to investigate this alteration, the hypothetical S-parameters data was used. Although this method shows much better results, it is pronounced that the results are very sensitive to the frequency band of interest. The low frequency points should be ignored.

The problem is how to decide the optimum starting frequency point for the analysis. It is not an easy task and depends on trial-and-error. Tables 4.13 and 4.14 show the results coming out of two different frequency bands (0.2-12.2 GHz) and (3.8-12.2 GHz), respectively. If the starting frequency increases above 0.2 GHz, the solution significantly improves because the noisiest points are excluded. If the starting frequency further increases beyond 3.8 GHz, the solution's accuracy deteriorates indicating that 3.8 GHz is the optimum starting frequency for this set of measurements and measurement error.

Table 4.12a C_{pg}, C_f, and C_{pds} of the hypothetical noisy data.

Parameter	C_{pg} (fF)	C_f (fF)	C_{pds} (fF)
Value	29.324	105.02	75.707
Err%	8.08	-5.02	0.25

Table 4.12b Pinch-off full-model parameters of the hypothetical noisy data.

Parameter	Value	Err%	Parameter	Value	Err%
R_g (Ω)	2.046	6.21	C_g (fF)	494.15	-23.54
R_d (Ω)	1.541	-22.29	C_d (fF)	182.66	8.67
R_s (Ω)	0.717	-28.12	C_s (fF)	182.66	8.67
L_g (pH)	142.889	26.27	C_{pg} (fF)	29.324	8.08
L_d (pH)	199.6	0	C_{pd} (fF)	36.876	-42.37
L_s (pH)	31	0			

Table 4.13 Solution of the hypothetical data over the frequency band (0.2-12.2 GHz).

Parameter	Value	Err%	Parameter	Value	Err%
R_g (Ω)	2.1	3.28	C_g (fF)	408.48	-2.12
R_d (Ω)	1.40	-11.4	C_d (fF)	195.02	2.49
R_s (Ω)	0.62	-10.85	C_s (fF)	195.02	2.49
L_g (pH)	200.48	-3.4	C_{pg} (fF)	31.07	2.59
L_d (pH)	199.6	0	C_{pd} (fF)	28.85	-11.40
L_s (pH)	31	0			

Table 4.14 Solution of the hypothetical data over the frequency band (3.8-12.2 GHz).

Parameter	Value	Err%	Parameter	Value	Err%
R_g (Ω)	2.19	-0.4	C_g (fF)	400.69	-0.17
R_d (Ω)	1.28	-1.7	C_d (fF)	199.71	0.146
R_s (Ω)	0.59	-5.3	C_s (fF)	199.71	0.146
L_g (pH)	195.02	-0.63	C_{pg} (fF)	31.71	0.58
L_d (pH)	199.6	0	C_{pd} (fF)	26.07	0.65
L_s (pH)	31	0			

To avoid the difficulty of choosing the optimum starting frequency point, we finally modified the algorithm as explained in section 3.2.3. The objective function is modified to include the errors of the capacitive components as in equation (3.26). L_g is added to the optimization variables to end up with three optimization variables. This method shows relatively accurate results and insensitivity to the frequency band of analysis as well. Tables 4.15 and 4.16 show the results of two different frequency bands (0.2-12.2 GHz) and (6.2-12.2 GHz), respectively. The values are fairly matching.

Table 4.15 Solution of final proposed method over the frequency band (0.2-12.2 GHz).

Parameter	Value	Err%	Parameter	Value	Err%
R_g (Ω)	2.27	-4.12	C_g (fF)	403.04	-0.76
R_d (Ω)	1.19	5.56	C_d (fF)	198.68	0.66
R_s (Ω)	0.62	-10.59	C_s (fF)	198.68	0.66
L_g (pH)	194.87	-0.55	C_{pg} (fF)	31.59	0.97
L_d (pH)	199.6	0	C_{pd} (fF)	26.69	-3.05
L_s (pH)	31	0			

Although the errors of some elements in Table 4.16 are slightly bigger than these in Table 4.15, our analysis proves that the errors over the frequency band (6.2-12.2 GHz) are less in the presence of finite resistive value between the drain and the source R_{ds}, in parallel with C_{ds},. For this reason, it is preferable to limit the frequency to (6.2-12.2 GHz) during pinch-off analysis.

Table 4.16 Solution of final proposed method over the frequency band (6.2-12.2 GHz).

Parameter	Value	Err%	Parameter	Value	Err%
R_g (Ω)	2.27	-4.06	C_g (fF)	403.52	-0.88
R_d (Ω)	1.19	5.39	C_d (fF)	198.52	0.74
R_s (Ω)	0.62	-10.78	C_s (fF)	198.52	0.74
L_g (pH)	194.73	-0.48	C_{pg} (fF)	31.57	1.04
L_d (pH)	199.6	0	C_{pd} (fF)	26.79	-3.45
L_s (pH)	31	0			

4.6.3 Iterative Scheme for Parasitics:

This is the last step to calculate the parasitics L_d, L_s, C_{pg}, C_{pd}, and R_g. After the two principal procedures have been tested in the last two subsections, we incorporate them in an iterative scheme as described in section 3.5.1. The scheme was applied to a few similar MESFET devices fabricated on the same wafer and measured at different temperatures. The tolerance ε of the stop criteria is 10^{-5}. The devices have the same nominal geometry and construction. Each device is GaAsTEK 0.8x300 μm^2 MESFET. S-parameters were measured for each device at pinch-off voltage V_{gs}=-2v while V_{ds} was set at zero bias voltage. All the extracted parameters are listed in Table 4.17 for the different devices at 25°C. The devices are identified on the wafer by two indices. The indices most probable point out the position of the device on the wafer indicating the row and the column of the device.

The perturbations of all elements are reasonable. Nevertheless, the perturbation of C_{pg} is relatively big which might be attributed to the individual variations in the device fabrication. Although all the devices are built up on the same wafer, the devices might be slightly different in its electrical and physical properties. For example, the doping density cannot be uniform over the wafer. This slight variation should lead to some electrical properties variations from device to device on the same wafer.

Table 4.17 L_d, L_s, C_{pg}, C_{pd}, and R_g of the GaAsTEK 0.8x300 μm^2 MESFET devices at 25°C.

Device ID#	02-00	03-01	01-01	02-01	02-02	PERT%
L_d (pH)	73.80	71.83	69.35	73.08	70.79	6.20
L_s (pH)	66.79	67.02	70.65	67.08	68.11	5.68
C_{pg} (fF)	28.34	26.69	45.86	27.97	33.15	59.16
C_{pd} (fF)	59.16	59.79	56.96	59.01	57.32	4.84
R_g (Ω)	9.03	8.90	9.99	8.85	9.09	12.43

PERT is the perturbation in the parameter value for all devices which can be defined as:

$$PERT\% = \frac{\max imum\ value - \min imum\ value}{average} x100 \quad (4.2)$$

The parameters were extracted for the devices (02-00 and 02-02), which were measured at two more different temperatures –40°C and 85°C. The data was helpful to understand and analyze the effect of the temperature on the different elements of the model. Figures 4.11a through 4.11c show the variation of each parameter with the temperature. Figure 4.11a shows interesting features for the inductive parasitics. Both devices show similar thermal characteristics.

L_d and L_s demonstrate that the inductances do not exhibit regular increase or decrease with temperature and are not constant either. All curves, rather, show peak inductances at room temperature. In fact, we need more points on the curves to accurately determine the temperature at which the maximum inductance occurs and to be able to suggest fitting function to the inductance. We might justify the trend of the inductive curve that the dimensions of the pad metalization and substrate thickness shrink down at very low temperatures; consequently the magnetic flux linkage decreases. On the other hand, the length and width of the metalization increase at high temperatures so that the net magnetic flux linkage decreases. This might be possible because the effect of the width growth is larger than that of the length growth.

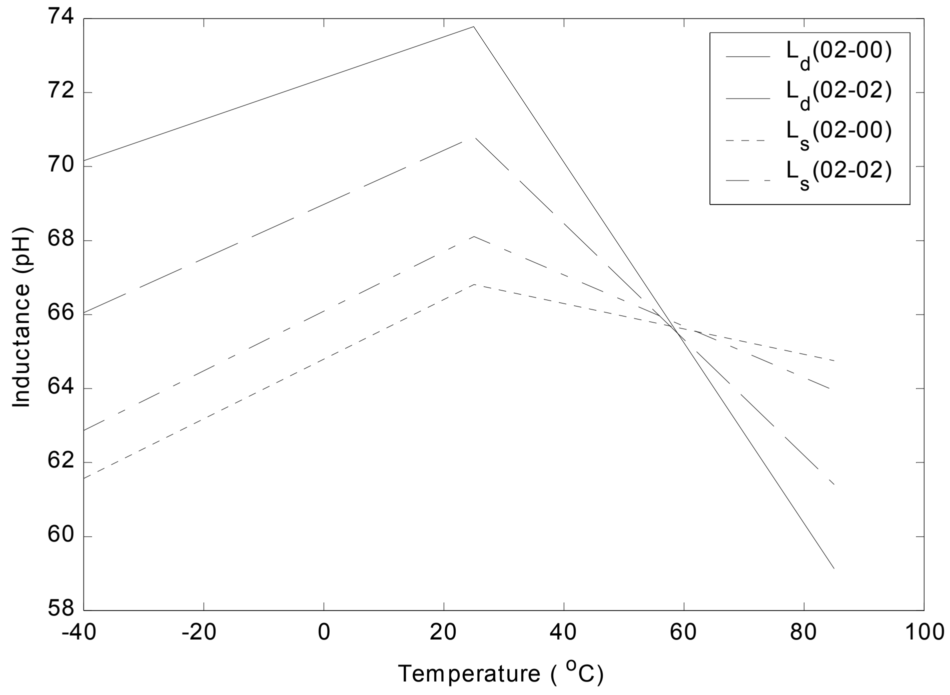

(a)

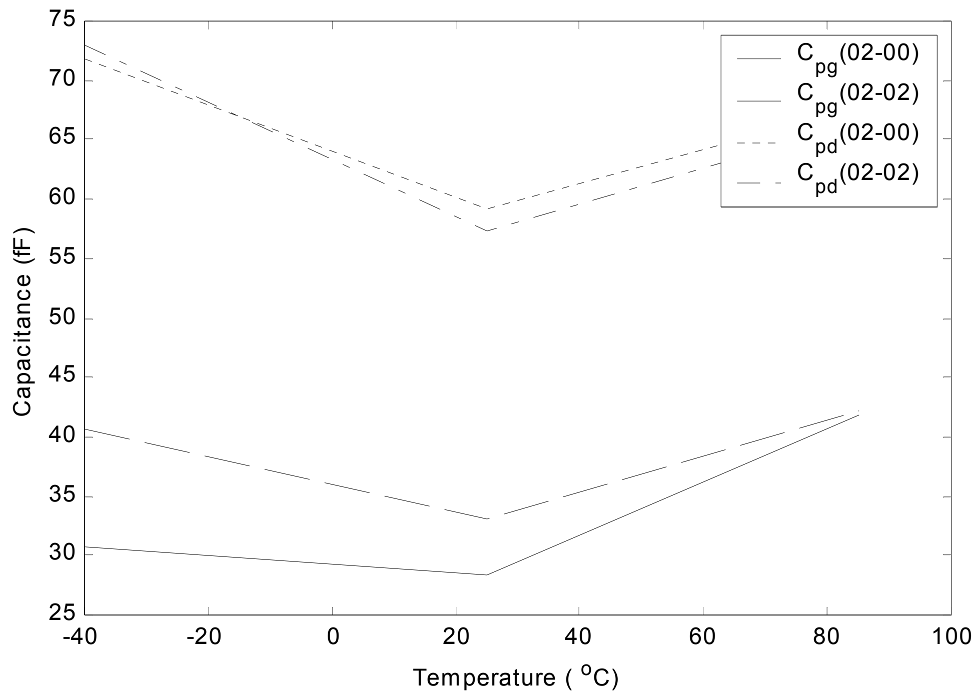

(b)

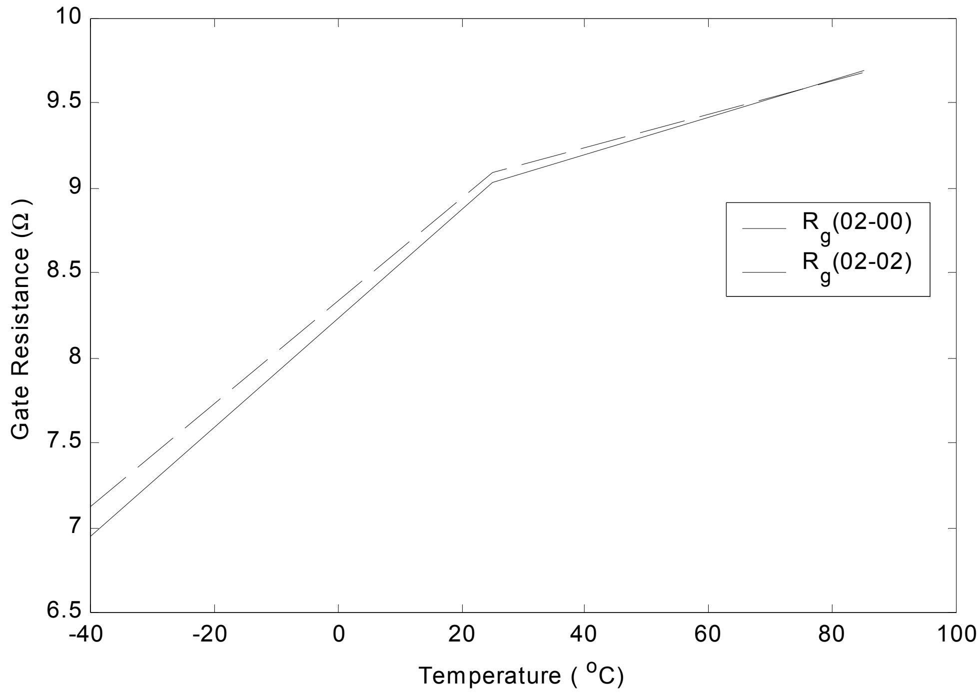

(c)

Figure 4.11 Parasitic parameters versus temperature for two devices. 02-00 and 02-02: (a) L_d and L_s (b) C_{pg} and C_{pd} (c) R_g

Figure 4.11b also shows some interesting features for the pad capacitances. Both pad capacitances C_{pg} and C_{pd} exhibit the same trend that the pad capacitance increases if temperature deviates from room temperature in either ways. The interpretation of such phenomenon depends on the metalization layout as well as the thermal properties of both the semi-insulating GaAs substrate and the crossover insulating material. These factors are not well known for the device of concern. The thermal properties of GaAs, to the best of our knowledge, are not documented in the literature. However, we may propose some justifications for the pad capacitance behavior versus temperature. The pad capacitance comes from the capacitance through the GaAs substrate in addition to the crossover areas between drain (or gate) metalization and source metalization. The pad capacitance, therefore, can be modeled as a simple parallel plate capacitance. As the temperature decreases, the insulator thickness decrease dominates the area shrinkage to effectively

increase the capacitance. In contrast, as the temperature increases, the area expansion dominates the insulator thickness increase. Alternatively, the permitivity of the material may increase as the temperature varies in either directions above or below the room temperature.

R_g is plotted in Figure 4.11c which shows a reasonable behavior. The behavior is somehow analogous to the well-known behavior of metals with temperature. The resistance of a metal increases linearly with the temperature. R_g declines from the straight line at high temperatures because the metal of the gate probably leaks through the semiconductor material or the effective temperature coefficient of the metalization layers of the gate probably decreases with temperature.

4.6.4 Model Parameters at Normal Bias Conditions:

The last step in our systematic extraction technique is to calculate the unknown parameters at normal bias conditions knowing the values of L_d, L_s, C_{pg}, C_{pd}, and R_g. The parameters have been extracted at multiple bias voltages for different devices at three different temperatures. We will explain the results and show the robustness of our proposed technique. Let us first analyze the results of one device (02-00) at the room temperature 25°C. The values of L_d, L_s, C_{pg}, C_{pd}, and R_g for the device (02-00) are listed in Table 4.17. The extraction technique was applied to the measured S-parameters of the device for multiple V_{gs} and V_{ds} bias voltages.

Figure 4.12 shows the calculated and the measured S-parameters at V_{gs}=-1.2v and V_{ds}=4v. The calculated S-parameters are in good agreement with the measured S-parameters. Similar results were obtained at different bias points. The return transmission parameter S_{12} seems to have a relative big discrepancy compared to the other parameters. This is might be acceptable since the value of S_{12} is small compared to S_{21}. All other measured and modeled S-parameters are almost coincided which show how reliable our extraction procedure is.

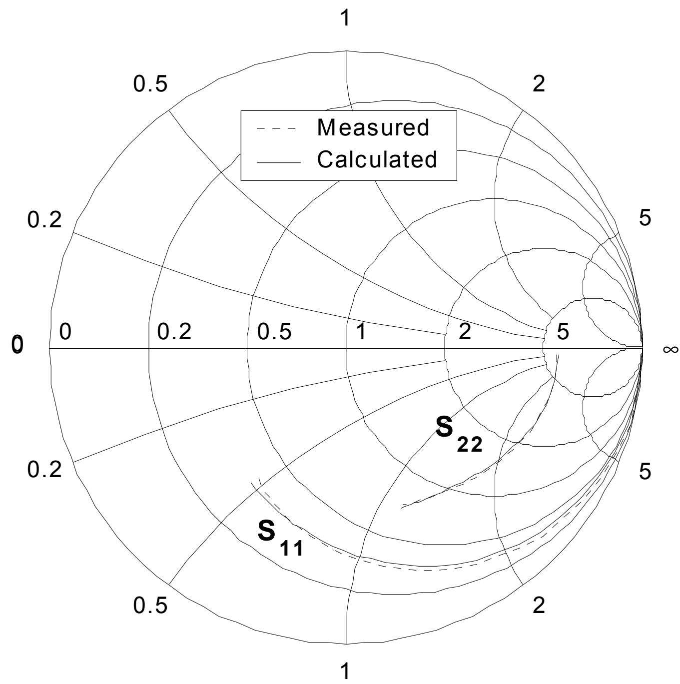

1
0.5
2
Measured
Calculated
0.2
5
0
0
0.2
0.5
1
2
5
∞
S22
0.2
5
S11
0.5
2
1

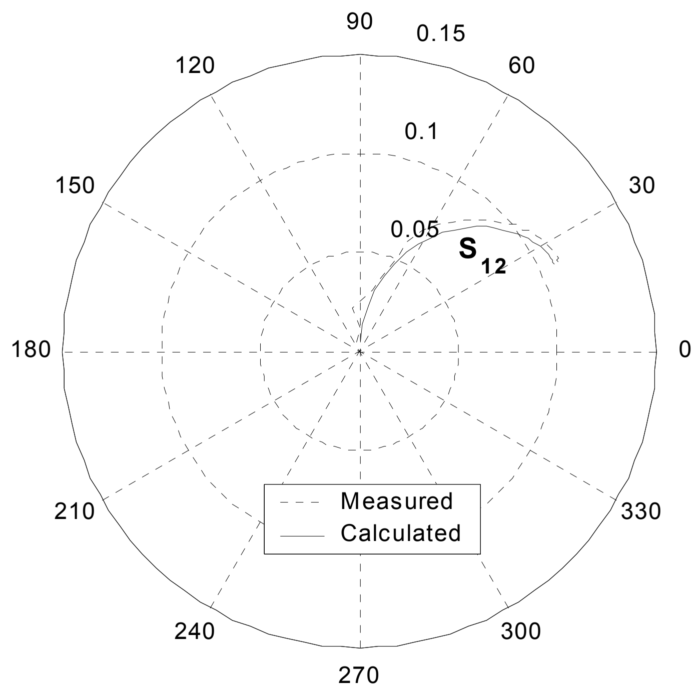

90
0.15
120
60
0.1
150
30
0.05
S12
180
0
Measured
Calculated
210
330
240
300
270

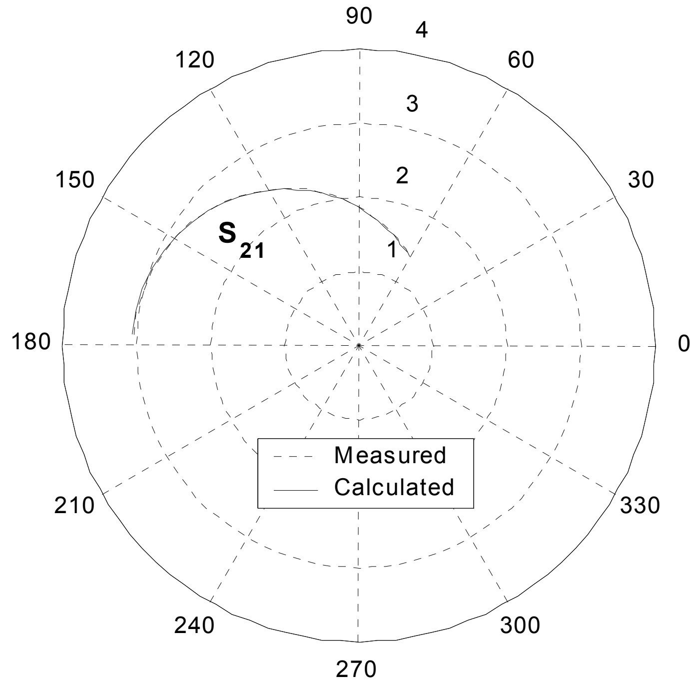

Figure 4.12 Measured and calculated S-parameters of the device (02-00) at V_{gs}=-1.2v and V_{ds}=4v showing good agreement.

The parameters of the model have been also extracted for the same device for different values of V_{gs} and V_{ds} at room temperature 25°C. The bias voltages of V_{ds} are 3, 4, and 7V while these of V_{gs} are 0, -1.2, -1.4, -1.5, -1.6, -1.8, and –2V. The nominal pinch-off voltage of this device is –2V. The different parameters are plotted in Figure 4.13, which depicts the behavior of each parameter as a function of the gate and the drain bias voltages. C_{gs} is plotted in Figure 4.13(a) while C_{gd} is plotted in Figure 4.13(b). Both graphs are physically meaningful. The value of C_{gs} increases as V_{gs} increases since the reverse bias voltage across the gate-source junction decreases. It is well known from the junction physics that the depletion capacitance increases as the reverse bias voltage decreases because the depletion region width decreases. Also, the value of C_{gs} slowly increases as V_{ds} increases. The reason is, when V_{ds} increases, the reverse bias voltage across the gate-drain junction increases, and in turn the gate-drain depletion width increases. On the other hand, the gate-source depletion width reduces which results in higher values of C_{gs}. Since V_{ds} do not directly affect the depletion width of the gate-source junction, the dependence of C_{gs} on V_{ds} is not strong.

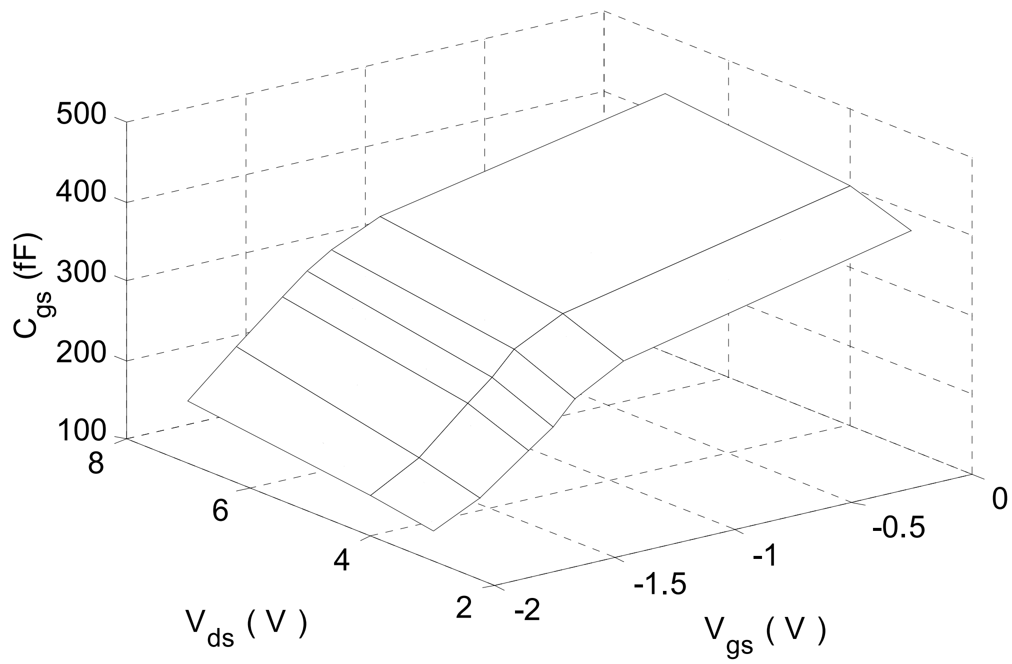

(a)

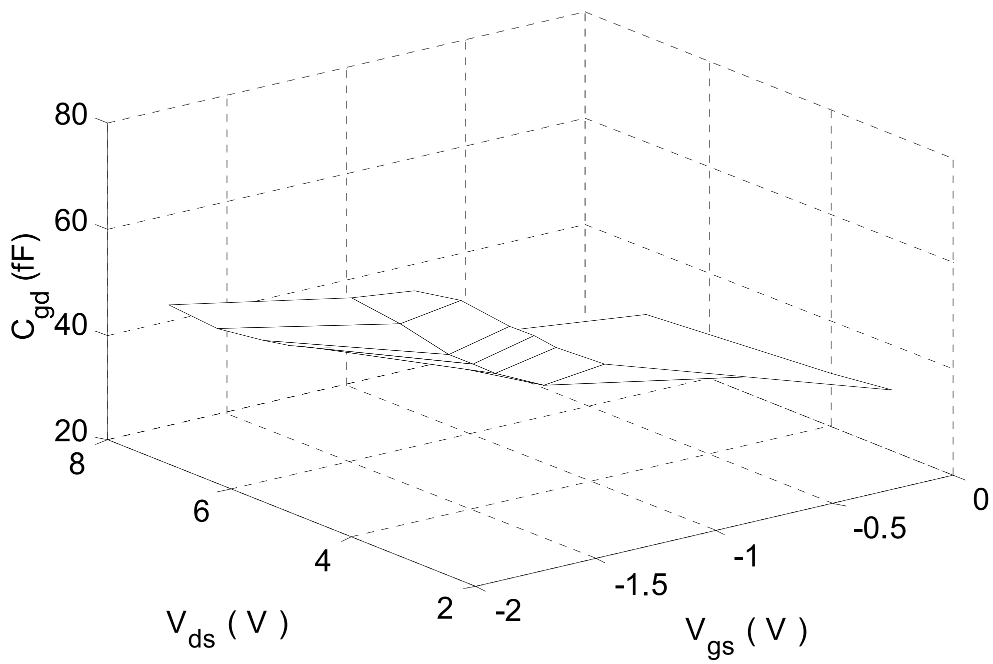

(b)

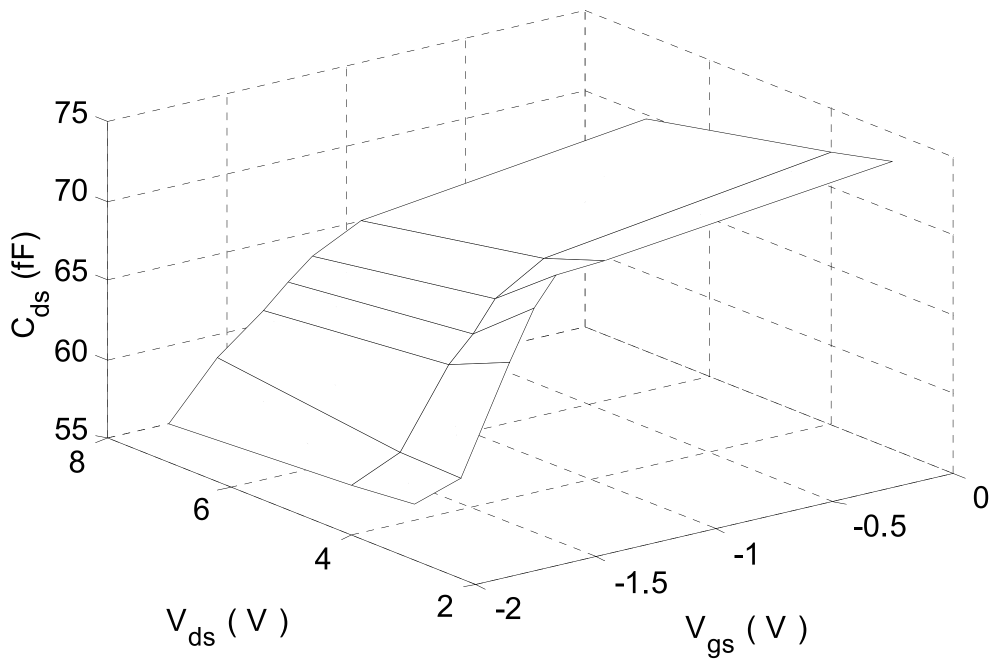

(c)

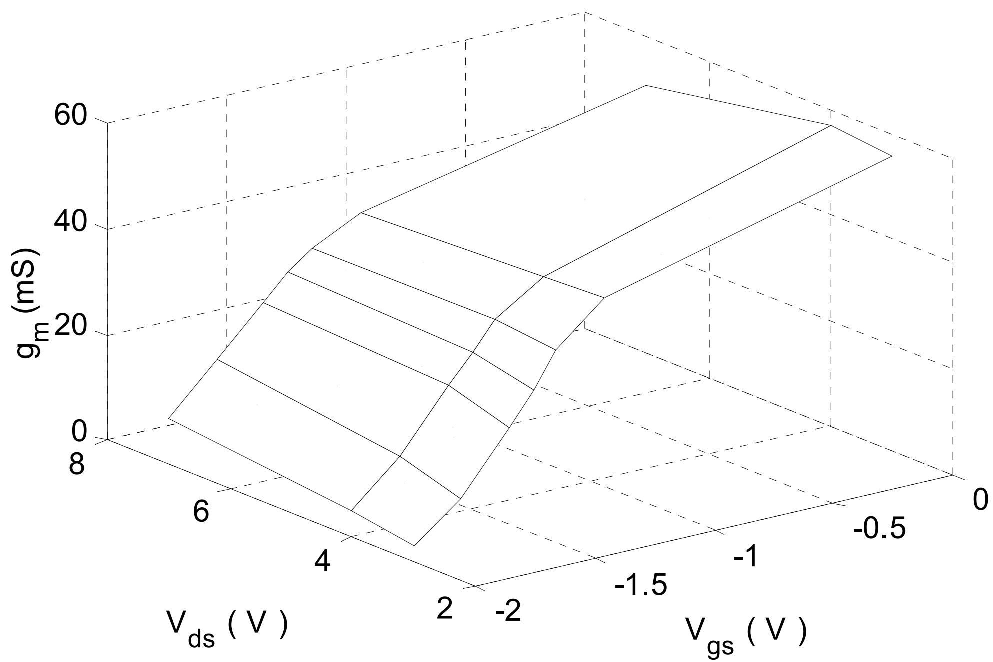

(d)

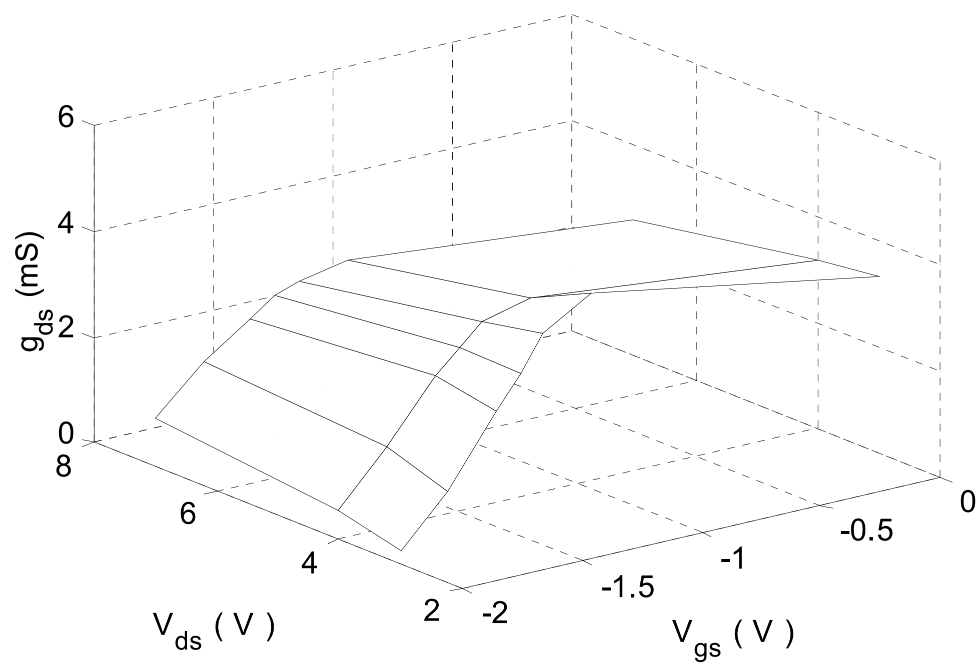

(e)

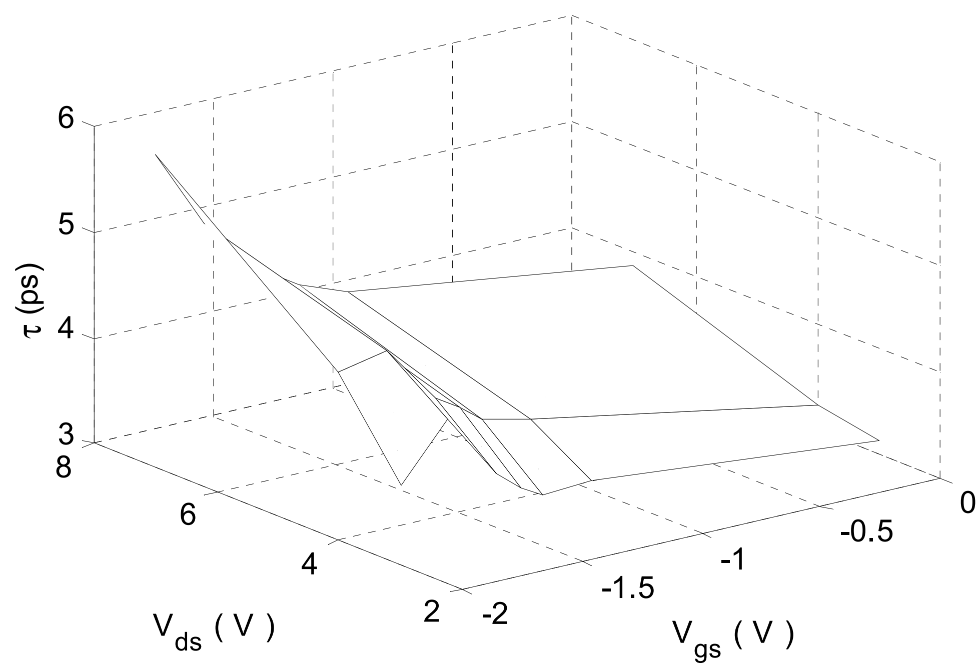

(f)

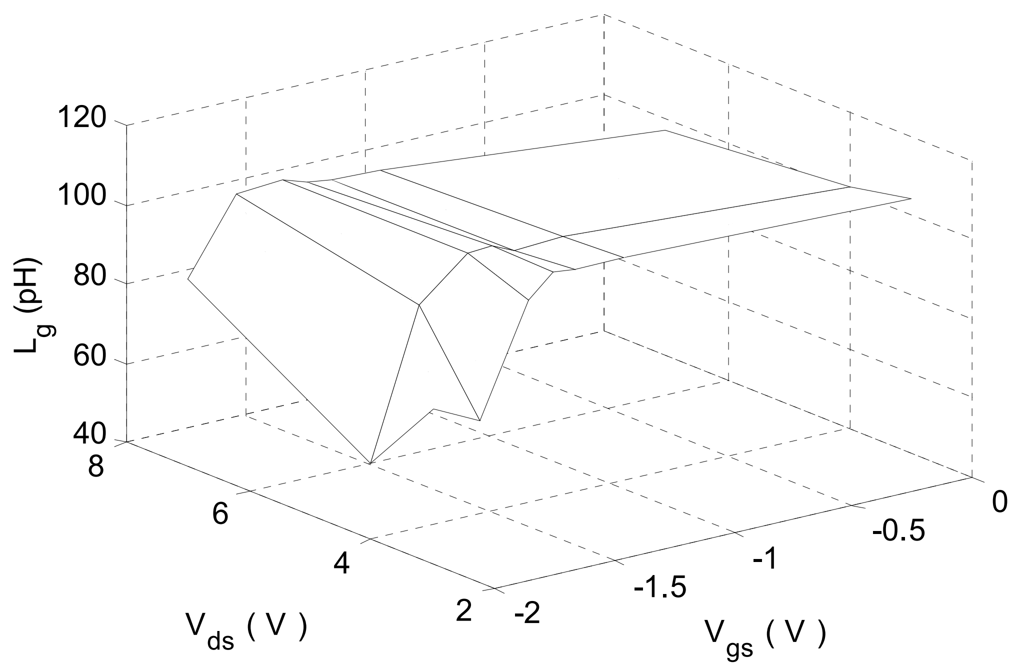

(g)

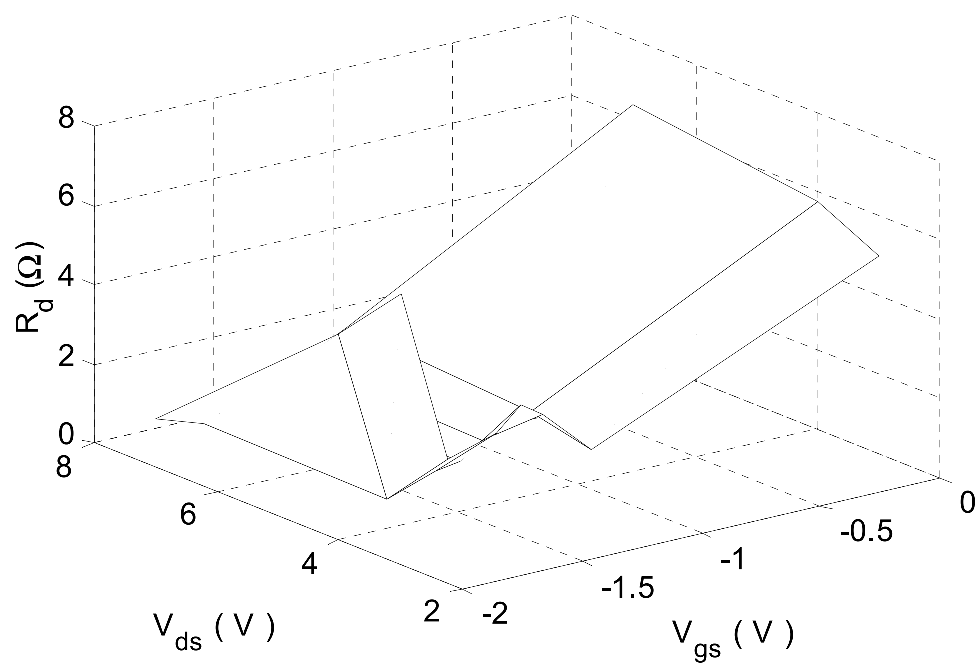

(h)

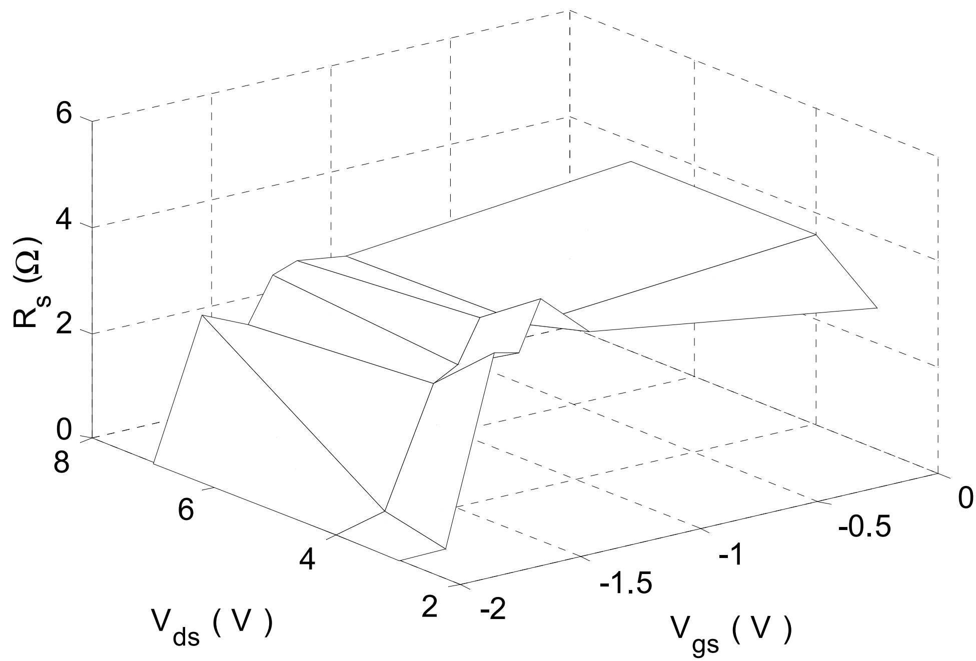

(i)

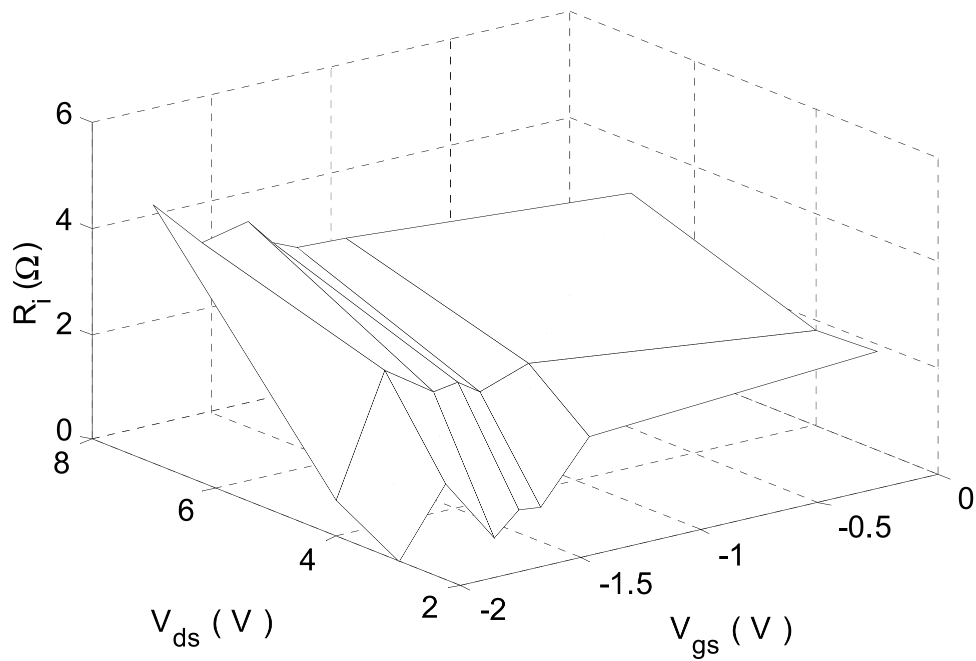

(j)

Figure 4.13 The different parameters of the model versus V_{gs} and V_{ds}.for the device (02-00)

Similar conclusions can be drawn from the C_{gd} plot in Figure 4.13(b). The behavior is perfectly the opposite to that of C_{gs} because increasing the depletion region width towards one side diminishes the depletion region width on the other side.

The characteristics of C_{ds} is shown in Figure 4.13(c) which provides good evidence that C_{ds} is less affected by the bias voltages specially for larger values of (V_{gs}-V_p) where V_p is the pinch-off voltage. This behavior is expected because C_{ds} basically exists due to parasitic capacitance through the substrate. Many authors, for this reason, assume that C_{ds} is constant. However, C_{ds} shows declination at smaller values of (V_{gs}-V_p) because of the charge accumulation regions in the channel.

The transconductance g_m is plotted in Figure 4.13(d) which shows reduction in the value as V_{gs} decreases. The plot supports the theoretical expectations. Since all values of V_{ds} are in the saturation region, the dependence of g_m on V_{ds} is very slight in this region. Figure 4.13(e) explains the dependence of g_{ds} on V_{gs} and V_{ds}. g_{ds} is highly dependent on V_{gs} and weakly dependent on V_{ds} in the saturation region. This observation is evident from the I_{ds}-V_{ds} characteristic curves of MESFET devices.

The transit time τ is depicted in Figure 4.13 (f). The value of τ can be assumed constant in the saturation region, which is implied in the literature. The value of τ becomes longer as V_{gs} decreases, which might make sense, because the depletion region extends to narrow down the channel. Consequently, the drain-source current takes longer time to respond to any V_{gs} variation. A glitch is noticed in the plot at V_{gs}=-2V, which is not related to the physical behavior, rather it is a numerical error because, at pinch-off voltage, I_{ds} is theoretically equal to zero. For this reason, τ loses it is physical meaning at such bias voltages.

The last four graphs of Figure 4.13 demonstrate the behavior of the extrinsic parasitic elements L_g, R_d, R_s, as well as the charging resistance R_i. These elements are the least accurate elements in the extraction process. Therefore, some spikes may appear in the graphs especially at smaller values of (V_{gs}-V_p). However, we can extract the trend of each

element as a function of V_{gs} and V_{ds}. The value of L_g at the pinch-off voltage can be ignored; thus, it is obvious that L_g is constant at 95pH. Both parasitic resistances R_d and R_s experience reduction in their values as V_{gs} decreases, which can be interpreted by the extension of the depletion area, and in turn the diminishing of the neutral area. The neutral area represents the most significant contributor of the parasitic resistances. In fact, R_i has no solid physical meaning that we can rely to interpret its behavior. It is primarily added to improve the match to S_{11}.

The high accuracy of our optimization procedure has been confirmed by investigating the results of some similar devices on the same wafer at the same bias voltages and temperature. The extracted parameters of these devices at 25°C, V_{gs}=-1.2V, and V_{ds}=3V are tabulated in Table 4.18, where PERT% was defined in equation (4.2). The maximum perturbation is 56.4%, which occurs for R_i. Also, The largest perturbation values are associated with the resistive elements R_d, R_s, and R_i because they are the least significant elements in the model. These values of perturbations are very acceptable for such elements since these elements may not be reproducible in the fabrication. This means that a big part of the perturbation is pertaining to the individual variation in the fabrication. The other elements have very appealing perturbation values, which indicate that these elements are the characteristic elements for both the device and its model.

Finally, we would like to end up our discussion with the thermal characteristics of the small-signal parameters. The parameters were extracted at V_{gs}=-1.2V, and V_{ds}=3V for two devices (02-00) and (02-02) at three temperatures –40, 25, and 85°C. The parameters are plotted in Figure 4.14. The parasitic resistances R_d, and R_s, as shown in Figure 4.14(a), almost exhibit the same behavior with the temperature that the resistances increase as the temperature goes up and down around the room temperature. In my opinion, the thermal behavior is characterized by the thermal behavior of the two parts forming the parasitic resistance: semiconductor resistance and metalization resistance. At higher temperatures, the metalization resistance becomes dominant while at lower temperatures the semiconductor resistance becomes dominant.

Table 4.18 Model parameters at V_{gs}=-1.2v and V_{ds}=3v for similar devices at 25°C.

Device ID#	02-00	03-01	01-01	02-01	02-02	PERT%
R_d (Ω)	1.79	2.11	1.78	1.52	1.43	39.40
R_s (Ω)	3.46	3.47	3.69	2.97	3	21.70
R_i (Ω)	1.49	1.36	0.828	1.57	1.33	56.40
L_g (pH)	106	107	123	108	113	15.26
C_{gs} (fF)	297	305	278	293	277	9.66
C_{gd} (fF)	48.9	51.2	46.7	52	51.9	10.57
C_{ds} (fF)	71	70.2	70.7	68.5	69.1	3.58
g_m (mS)	41.4	40.2	36.9	38.3	35.6	15.07
τ (ps)	3.38	3.49	3.12	3.56	3.48	12.92
g_{ds} (mS)	4.3	4.07	3.95	3.91	3.78	12.99

The behavior of R_i is not obvious, as shown in Figure 4.14(b), where each device experience a different trend at high temperatures. Once again, the physical origin of R_i is not clear enough to be analyzed. The gate inductance L_g shows interesting characteristics in Figure 4.14(c). The inductance is almost constant below the room temperature; in contrast it exhibits drastic declination at higher temperatures. The only interpretation, that we can afford here, is that the gate width expanded as the temperature increases; thus the inductance decreases. We may notice that the effect of width expansion should dominate the length expansion since the gate is relatively long (300 μm).

The gate intrinsic capacitances C_{gs} and C_{gd} are illustrated in Figure 4.14(d). C_{gs} is almost constant below 25°C while it shows significant increase at higher temperatures. C_{gd} is effectively constant; however it shows slight decrease as the temperature increases. The abrupt-junction approximation [3] indicates that the depletion capacitance can be written as:

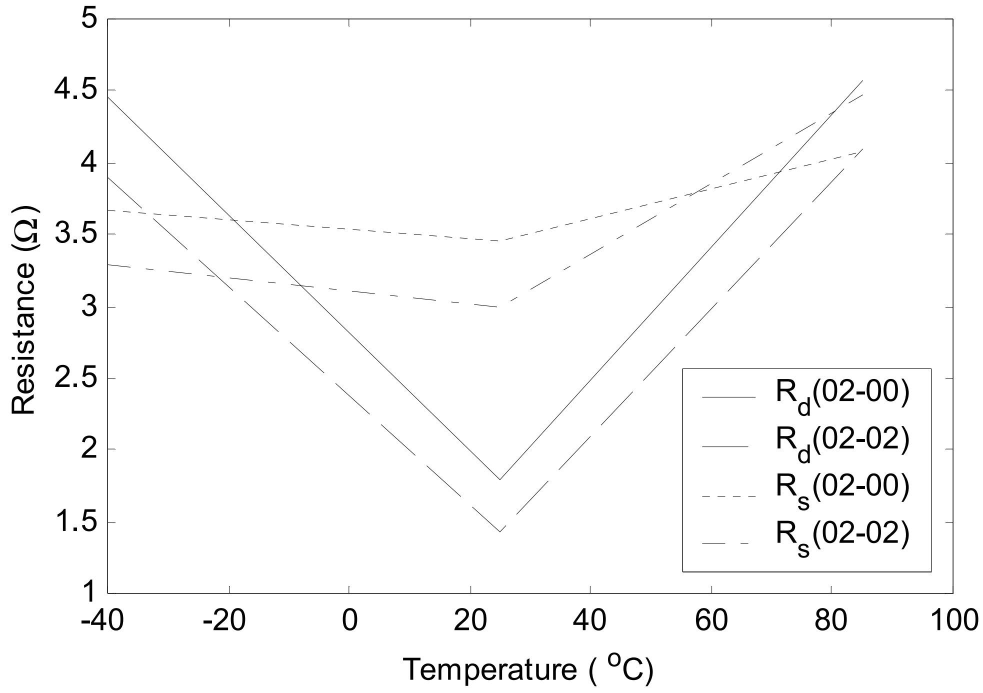

(a)

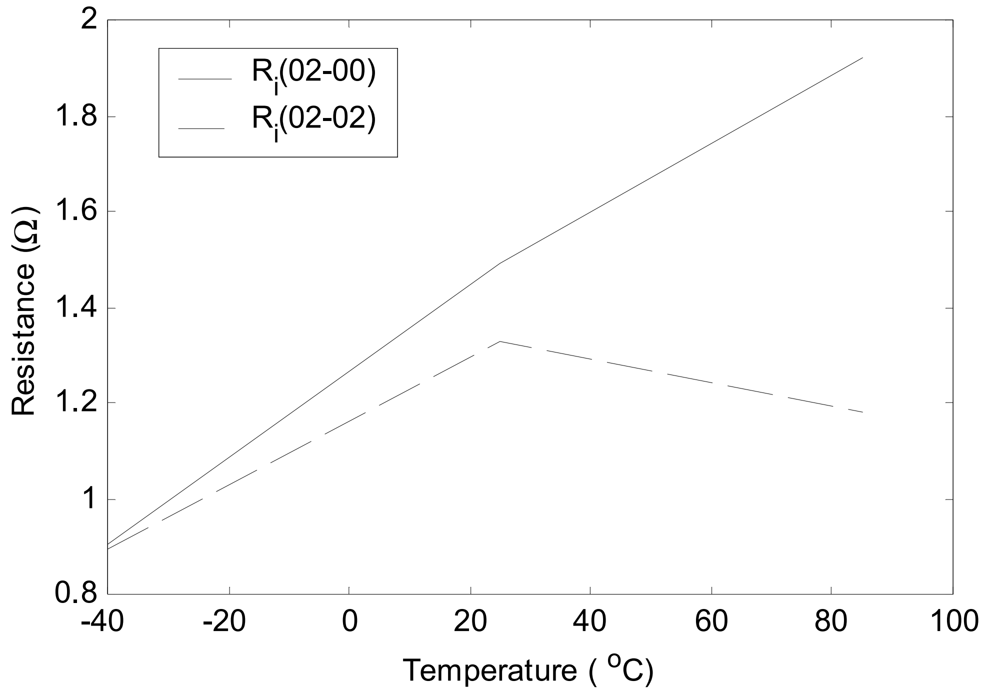

(b)

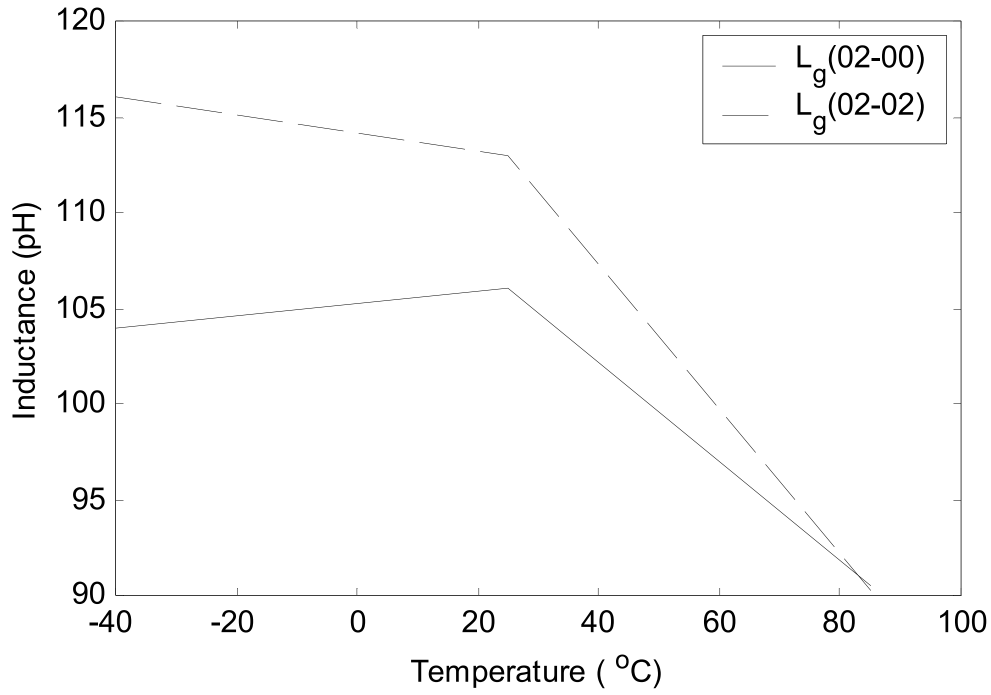

(c)

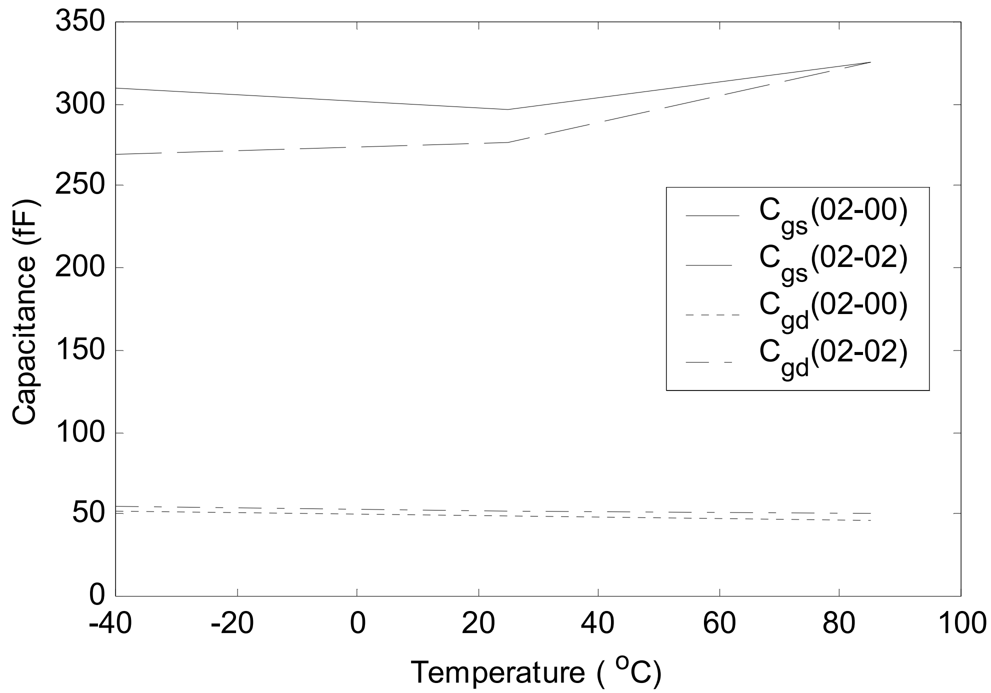

(d)

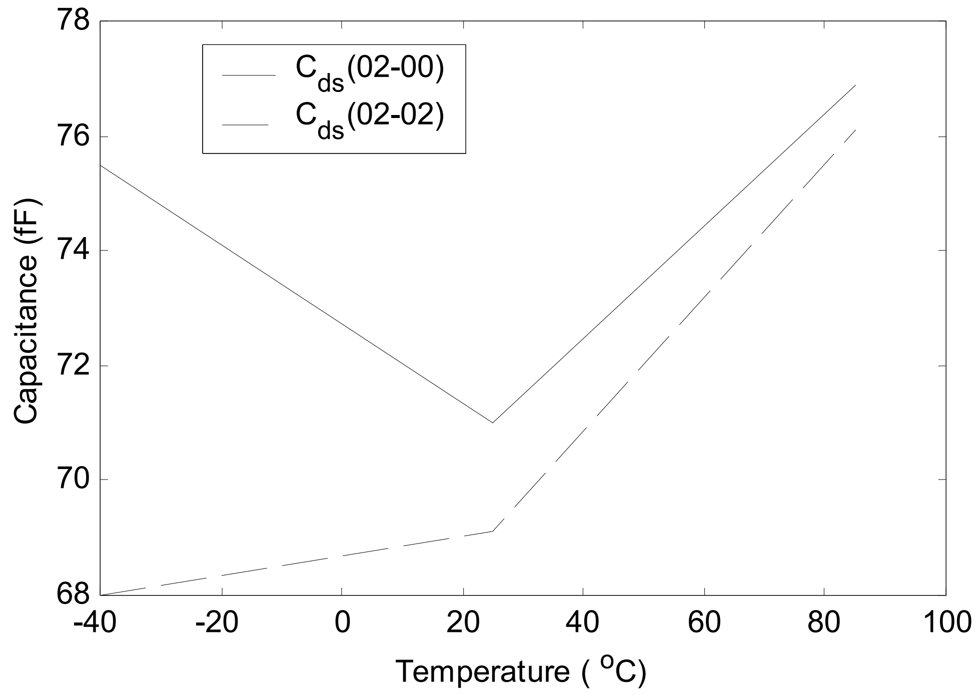

(e)

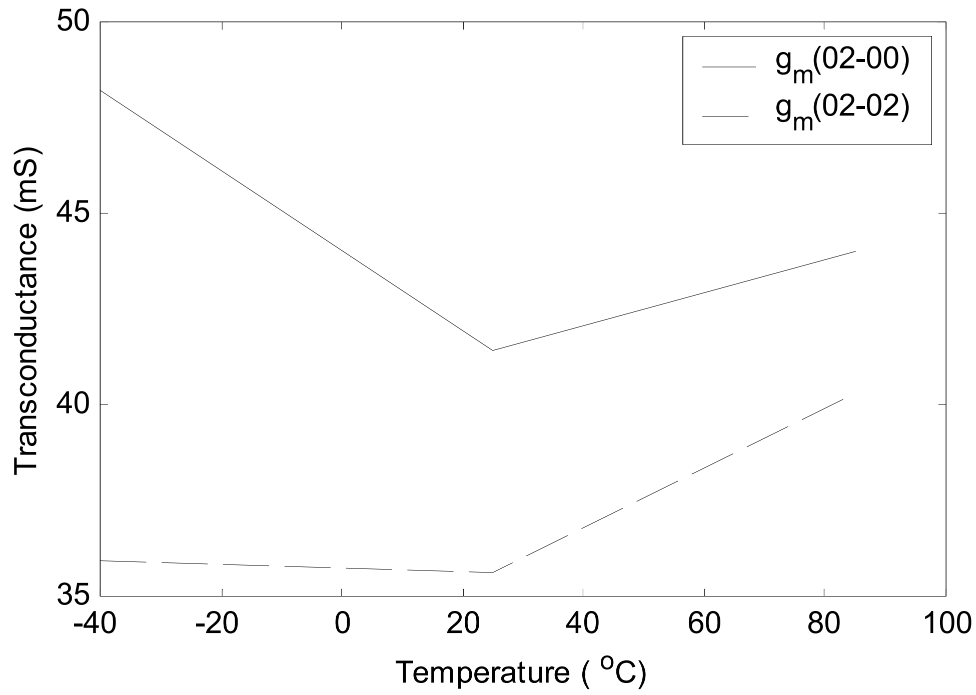

(f)

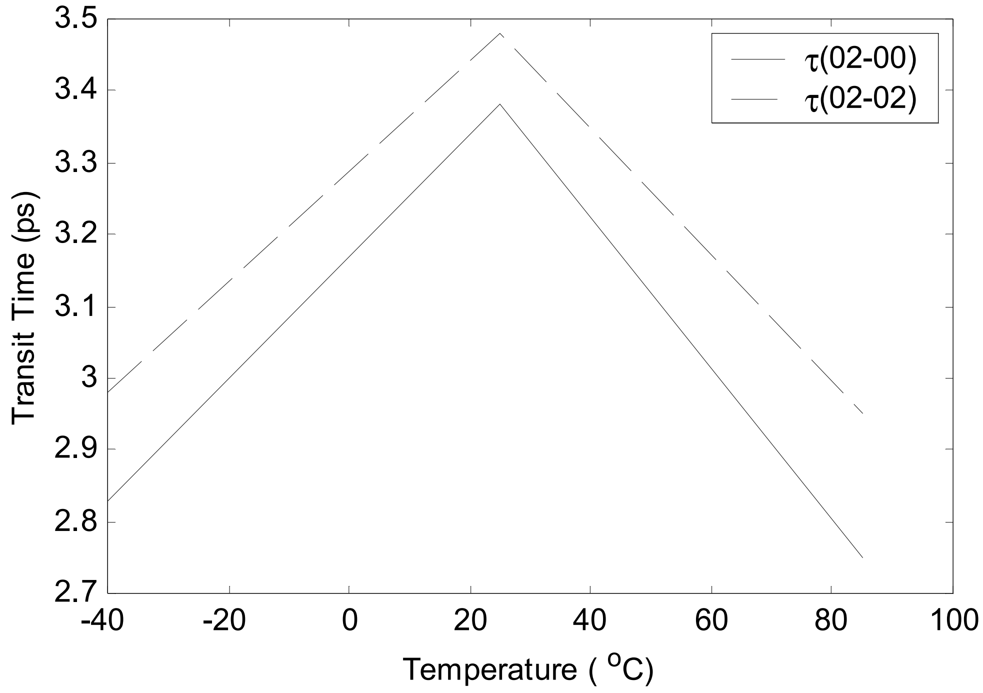

(g)

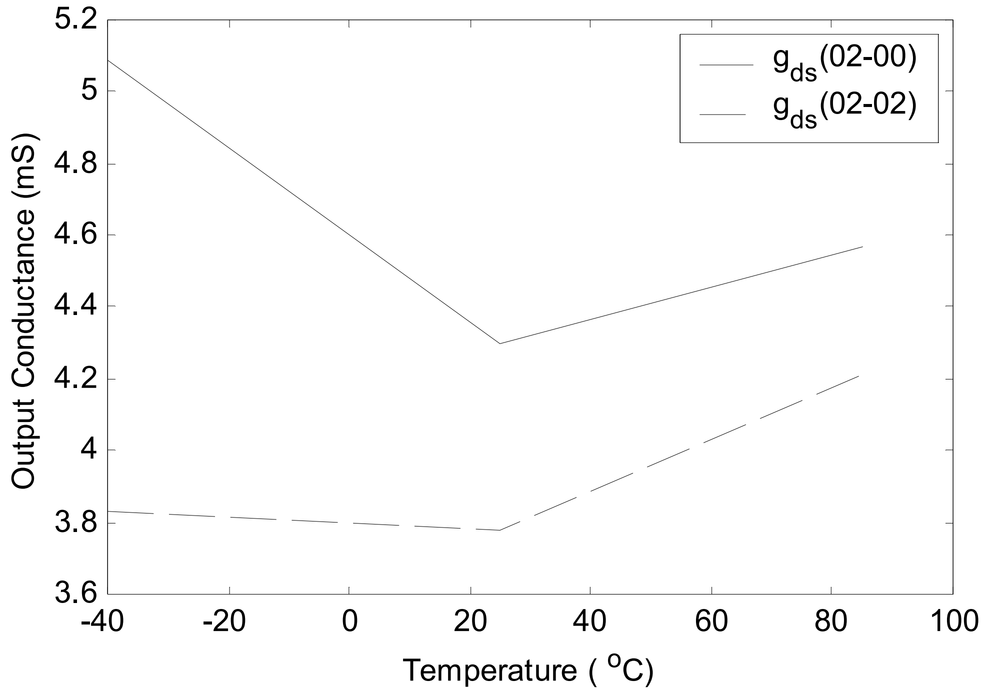

(h)

Figure 4.14 Small-Signal model parameters versus temperature at V_{gs}=-1.2V and V_{ds}=3V for the devices (02-00) and (02-02).

$$C = \frac{\varepsilon_s}{W} A \qquad (4.3)$$

where ε_s is the GaAs permitivity, A is the gate area and W is the depletion layer width. The thermal characteristics of the three parameters in equation (4.3) collaborate to control the thermal characteristics of C_{gs} and C_{gd} as shown in the figure. Unfortunately, the thermal characteristics of W are not well documented in the literature to thoroughly discuss C_{gs} and C_{gd} thermal characteristics.

The characteristics of C_{ds} are demonstrated in Figure 4.14(e) which shows weak dependence on the temperature. The substrate properties are accountable for such characteristics of C_{ds}. The behavior below 25° is contradicting for the two devices which might be pertaining to either the location of the device on the wafer or the calculation accuracy. Figure 4.14(f) shows an improvement in g_m as the temperature diverts from the room temperature. This dependence might be justified by the dependence of g_m on the drain-source current. The drain-source current depends on two main temperature-dependent factors: electron mobility and electron density. The electron mobility increases as the temperature decreases; in contrast the electron density increases as the temperature increases. The net variations of these factors contribute to the characteristics of g_m.

The transit time experience an improvement (decrease) as the temperature diverts from the room temperature, as shown in Figure 4.14(g). This implies that the drain-source current responds faster to the gate bias voltage variations. Figure 4.14(h) shows the thermal characteristics of g_{ds} indicating that the best temperature for this parameter is the room temperature at which g_{ds} is minimum. Otherwise, the slope of the drain-source current with respect to the drain-source voltage will increase resulting in less output resistance and larger output conductance.

4.7 Large-Signal Model Parameters:

This section is concerned with the results of the large-signal parameters for the drain-source current. A theoretical background is introduced in section 3.6. This section is not intended to demonstrate deep analysis for the large-signal model; it rather shows how the small-signal model parameters can be used as building units for the large-signal analysis, and therefore it explains the drain-source current model only. If a full large-signal model is needed, it is necessary to derive models for the other elements of the large-signal model such as C_{gs} and C_{gd}.

The VGEXP parameter is fixed at 2. This choice is reasonable since most of the other models, other than Advanced Curtice Model, assumes this value, which complies with the physical behavior of the drain current as a function of V_{gs}. We fixed this parameter in order to avoid entrapment in local minima and to help the optimizer to locate reasonable values for the other parameters. Figure 4.15 shows the measured and calculated drain current, transconductance, and output resistance as functions of V_{ds} for different V_{gs} values. The measurements are carried out for the device (02-00) at 25°C. The weighting factors are $W_{I_{ds}}$=1, W_{g_m}=1, and $W_{g_{ds}}$=0.01. These values of weighting factors biases the modeled quantities towards the RF behavior of the device since g_m and g_{ds}, which are RF quantities, are used with one dc quantity I_{ds} in the optimization. Figure 4.15 shows good compromise between the dc and RF performance. Figure 4.16(a) through Figure 4.16(c) show the effect of the weighting factors on the modeled parameters versus V_{ds} at zero gate-source bias voltage. The optimization was run on three weighting factors combinations. The model is optimized to dc performance only implied by $W_{I_{ds}}$=1, and $W_{g_m} = W_{g_{ds}}$=0. The model is then optimized to the RF performance only implied by $W_{I_{ds}}$=0, and $W_{g_m} = W_{g_{ds}}$=1. Finally, it is optimized to compromise both dc and RF performances indicated by DC/RF on the figure; the weighting factor combination is $W_{I_{ds}} = W_{g_m}$=1, and $W_{g_{ds}}$=0.05.

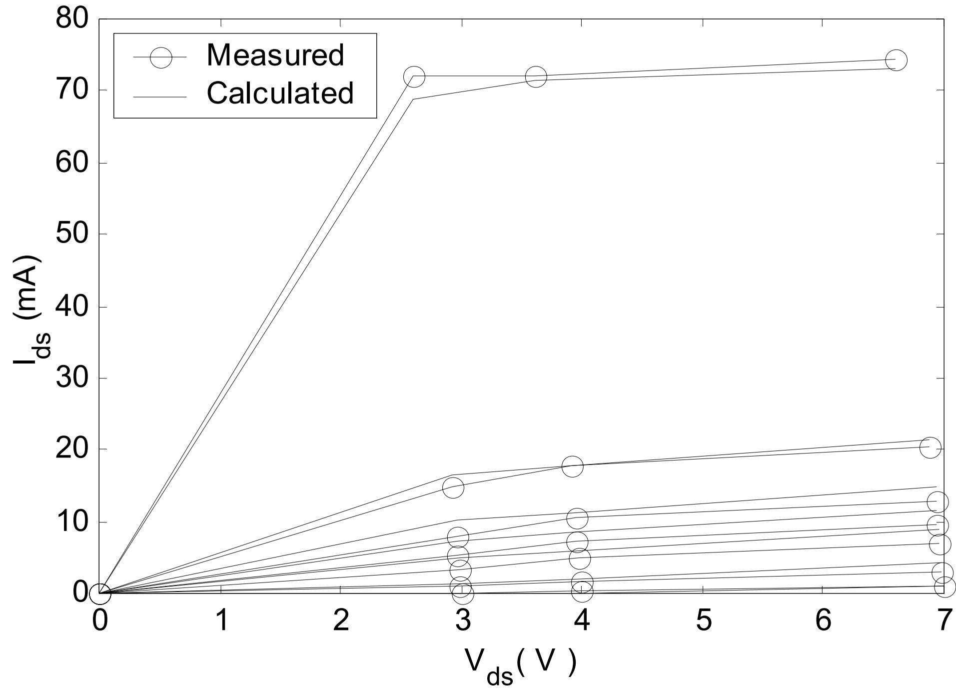

(a)

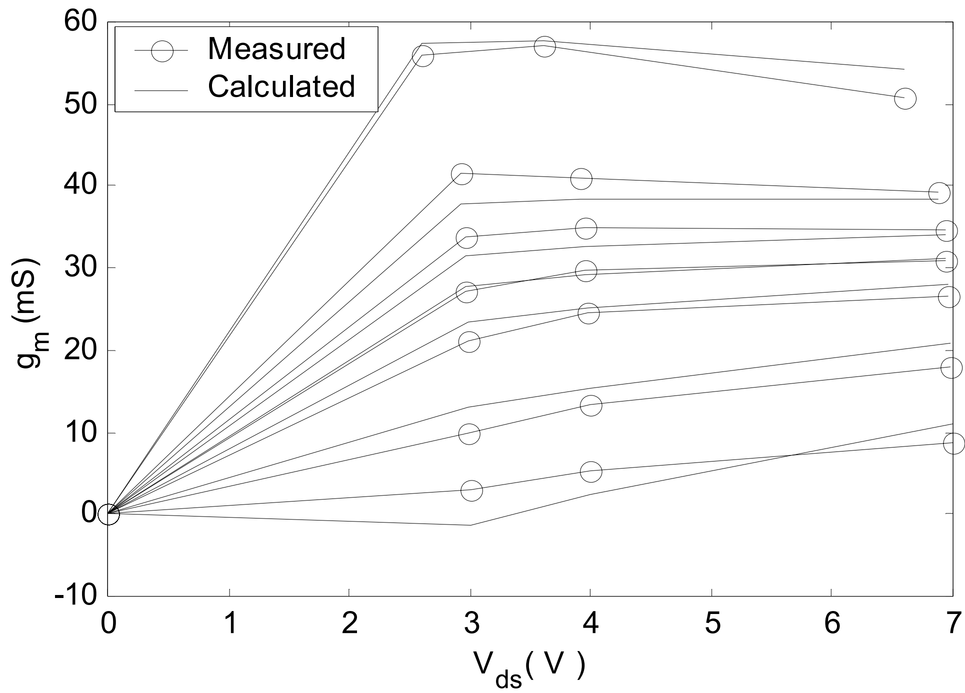

(b)

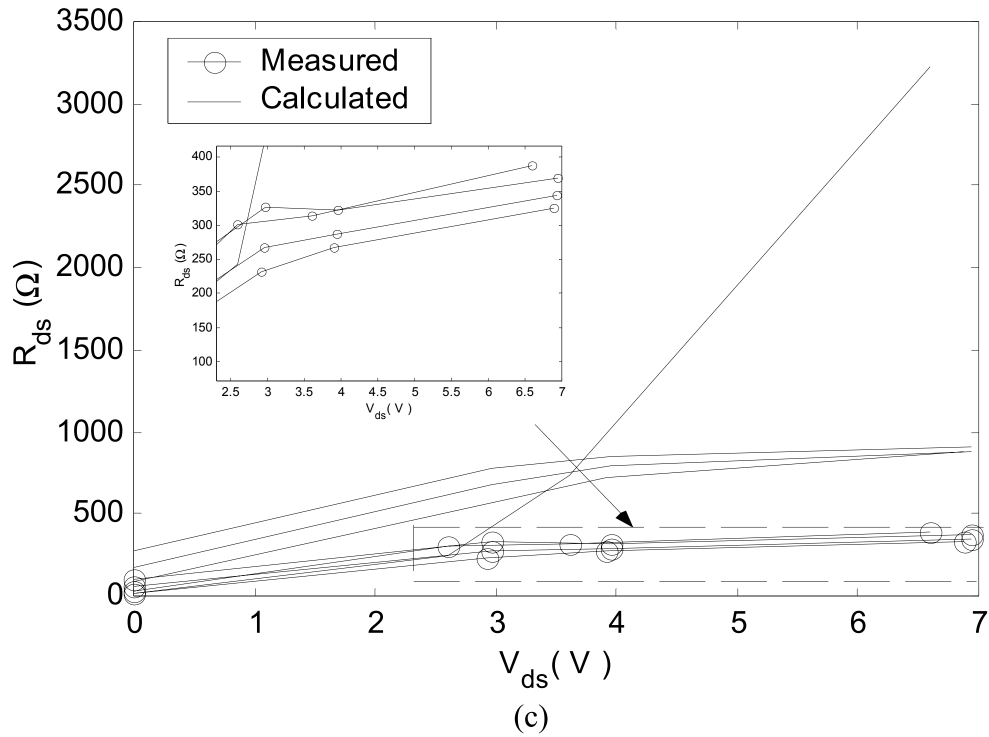

(c)

Figure 4.15 Measured and Calculated I_{ds}, g_m, and R_{ds} versus V_{ds} for device (02-00) at different V_{gs} values: (a) drain current (b) transconductance (c) output resistance.

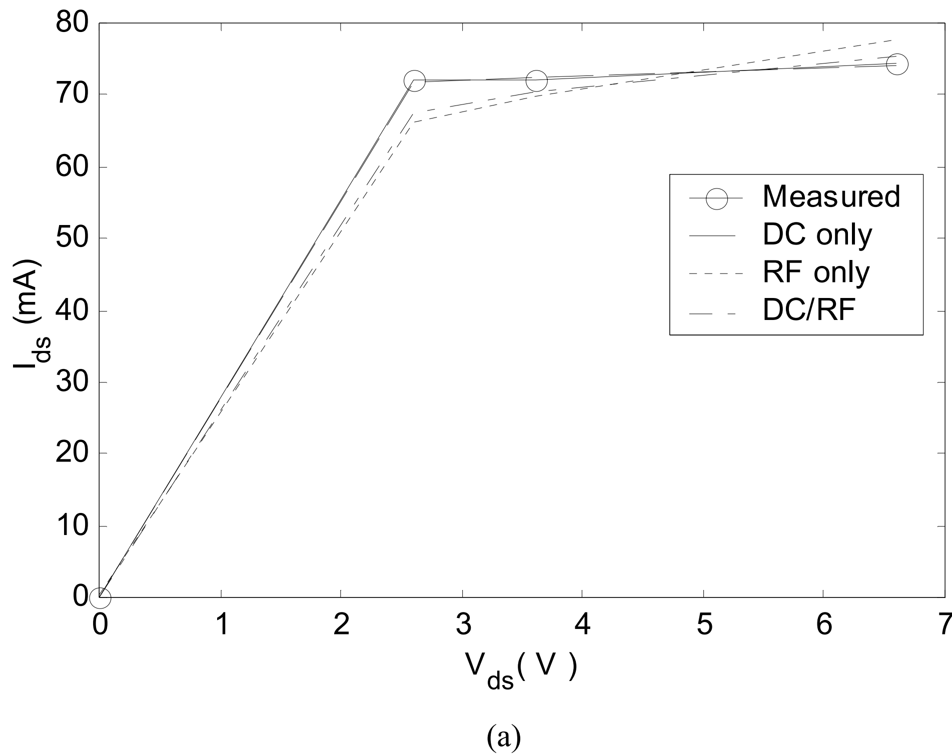

(a)

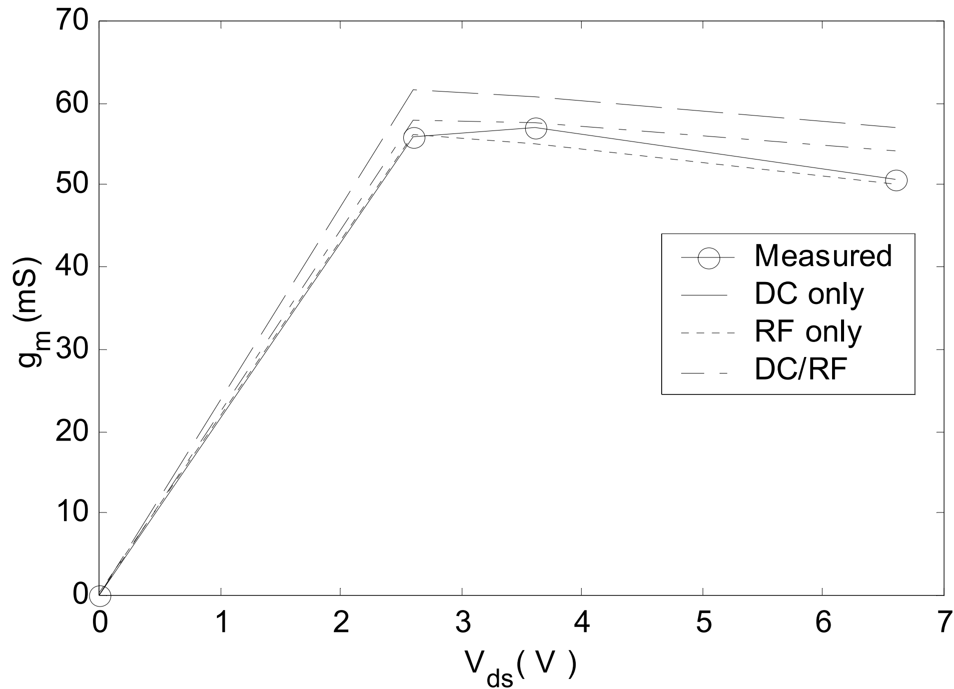

(b)

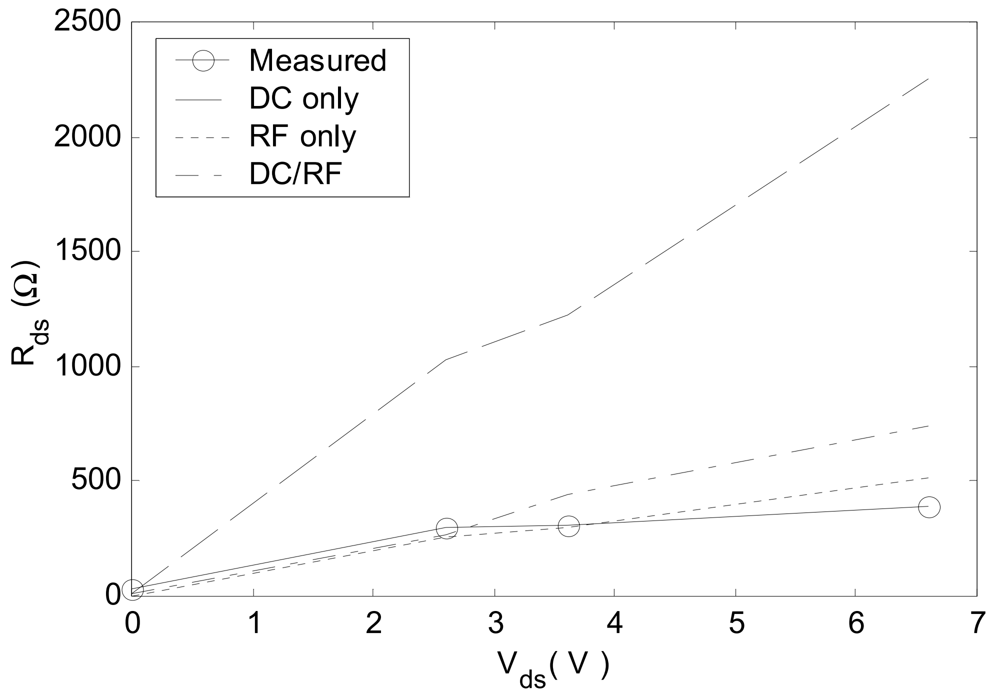

(c)

Figure 4.16 Effect of weighting factor combinations on different parameters versus V_{ds} at V_{gs}=0: (a) drain current (b) transconductance (c) output Resistance.

Figure 4.16(a) illustrates measured and modeled drain current. The dc-based model is almost identical to the measured dc current. On the other hand, if RF data is used only, the modeled current has big discrepancy with the measured current. When both dc and RF data are used, the modeled current shows a compromise between dc and RF data. The transconductance and output resistance show similar behavior in Figures 4.16(b) and 4.16(c), respectively. The measured g_m and g_{ds} are the extracted RF small-signal parameters. So, The use of RF data biases the modeled parameters towards the measured values. In contrast, the use of dc data pushes the modeled parameters away from the measured values. Again, The use of dc and RF data achieves a reasonable compromise between the dc and RF values of these parameters.

Chapter 5

Conclusion

In this dissertation, we developed a novel systematic procedure to extract a 15-element small signal MESFET model from three sets of S-parameter measurements at different bias conditions. We explained that one resistive parameter of the model, at least, should be pre-determined before the main optimization process is started to extract other parameters. This problem was thoroughly discussed and some analysis was introduced to support the problem statement. We recognized that the best resistive element is the gate resistance because it is bias-independent. In other words, its value is almost constant over operating bias voltages. In contrast, the source and drain resistances may be bias-dependent.

The modeling technique goes through two major steps. The first step is aimed to estimate the gate resistance R_g as well as the pad capacitances (C_{pg} and C_{pd}) and the parasitic inductances of the source and the drain (L_d and L_s). The Cold-measurements at V_{ds}=0 and V_{gs}=0 are iteratively used with the pinch-off measurements to achieve this goal. The second step finalizes our proposed technique by extracting all other elements at normal bias conditions. The objective functions of the two steps are proposed so that good match between the measured and the modeled S-parameters are achieved and the variance of the dominant elements of the model is minimum. The objective function assures good accuracy and less sensitivity to the frequency range of measurement.

This technique was investigated to reveal that it could almost work over any frequency range with the presence of the unavoidable measurement errors. We explained its accuracy, preciseness, robustness and reliability using S-parameters of hypothetical models at pinch-off and normal bias voltage conditions. The hypothetical S-parameters were contaminated with noise to emulate the measurement errors. We discussed other optimization-based extraction methods and investigated their ability to extract the model parameters over relatively small frequency range (0.2-12.2 GHz). We saw how these

methods are sensitive to any measurement errors. Our technique shows accurate results over this limited frequency range in the presence of noise.

The technique was also applied to the S-parameter measurements of some actual MESFET devices. The devices were GaAsTEK 0.8x300 μm^2 MESFET devices whose measurements were obtained from GaAsTEK, a unit of ITT industries. The model parameters of similar devices on the same wafer were extracted and investigated to provide us with consistent and precise results. The measured and modeled S-parameters show good match to assure the ability of our technique to extract accurate values. The extracted parameters at different bias voltages are plotted versus V_{gs} and V_{ds}. The behavior of each parameter is analyzed in terms of the physical operation as both V_{gs} and V_{ds} are varied.

Moreover, the model parameters of two similar devices were extracted from the measurements at three temperatures 25^oC, –40^oC and 85^oC. The two devices show similar thermal characteristics that, once again, assured the preciseness, and robustness of the extraction technique. The thermal characteristics of the various model elements are discussed and related to its physical behavior.

The relation between the small-signal parameters and the extraction of the large-signal model parameters are also introduced. The transconductance and the output conductance are used in conjunction with the dc current measurements to extract the parameters of an empirical drain-source model. The objective function is proposed to fit the small-signal parameters and the dc current measurements; thus it affords a good compromise between the RF performance and the dc performance. The RF performance is implied by transconductance and the output conductance while the dc behavior is implied by the dc current measurements. Our work does not cover the full large-signal model. A full large-signal model requires deriving models for the other elements of the large-signal model such as C_{gs} and C_{gd}. Therefore, the work can be extended to the other elements of the model. The weakly bias-dependent elements can be assumed fixed to reduce the complexity of the computation with no significant sacrificing of the accuracy.

This work can also be extended to develop thermal models. The thermal models are integrated models to the large-signal and small-signal models about which we have already discussed. Each element of the small or the large signal model should be a function of the temperature as well. Thus, the extraction process may be repeated using S-parameter measurements at different temperatures for the same bias point. A temperature dependent relationship may be proposed whose parameters may be calculated by fitting this relationship to the extracted data [38]. The thermal models are vital in predicting the heating effects, which affect the performance of some circuits significantly. Power amplifiers are examples of circuits whose performance is subject to heating effects.

All the extraction procedures discussed so far are applied to one-finger gate layout only. The work can be extended to cover interdigitated-gate layouts. The model of the interdigitated-gate layout should be examined; and an extraction procedure can be proposed based on the topology of the model.

All the procedures in the dissertation were implemented in MATLAB. The graphs were also generated with MATLAB.

Appendix A
Intrinsic Small-Signal Model

The Intrinsic small-signal model of MESFET devices is shown in Figure 3.1, which consists of 8 elements: C_{gs}, R_i, C_{gd}, R_{gd}, g_m, τ, R_{ds}, and C_{ds}. This appendix demonstrates the derivation of the Y-parameters of this model described by equations (3.7). It also explains how the intrinsic parameters can be derived in equations (3.9).

A.1 Derivation of Intrinsic Y-Parameters:

Figure A.1 shows the intrinsic model separately out of Figure 3.1. The figure shows the intrinsic circuit as a 2-port network. The terminal voltage relations of this 2-port network can be expressed in terms of the Y-parameters as:

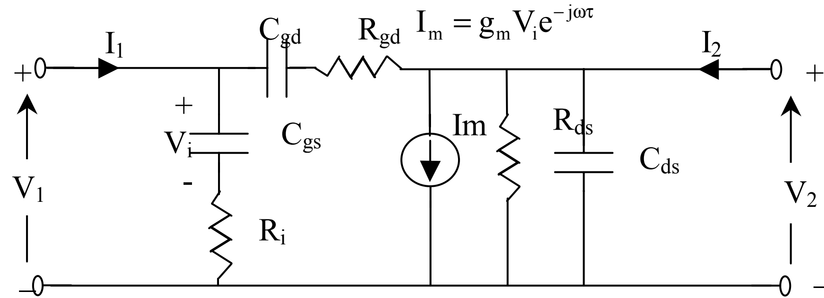

Figure A.1 Intrinsic model for MESFET devices.

$$I_1 = y_{11}V_1 + y_{12}V_2 \tag{A.1a}$$

$$I_2 = y_{21}V_1 + y_{22}V_2 \tag{A.1b}$$

The Y-parameters of equations (A.1a) and (A.1b) can be calculated for the circuit of Figure A.1 as:

$$y_{11} = \left.\frac{I_1}{V_1}\right|_{V_2=0} = \frac{1}{R_i + \frac{1}{j\omega C_{gs}}} + \frac{1}{R_{gd} + \frac{1}{j\omega C_{gd}}} = \frac{j\omega C_{gs}}{1 + j\omega R_i C_{gs}} + \frac{j\omega C_{gd}}{1 + j\omega R_{gd} C_{gd}} \quad \text{(A.2a)}$$

$$y_{21} = \left.\frac{I_2}{V_1}\right|_{V_2=0} = \frac{I_m - \frac{j\omega C_{gd}}{1 + j\omega R_{gd} C_{gd}} V_1}{V_1} = \frac{g_m e^{-j\omega\tau}}{1 + j\omega R_i C_{gs}} - \frac{j\omega C_{gd}}{1 + j\omega R_{gd} C_{gd}} \quad \text{(A.2b)}$$

$$y_{12} = \left.\frac{I_1}{V_2}\right|_{V_1=0} = -\left(\frac{-I_1}{V_2}\right) = -\frac{j\omega C_{gd}}{1 + j\omega R_{gd} C_{gd}} \quad \text{(A.2c)}$$

$$y_{22} = \left.\frac{I_2}{V_2}\right|_{V_1=0} = g_{ds} + j\omega C_{ds} + \frac{j\omega C_{gd}}{1 + j\omega R_{gd} C_{gd}} \quad \text{(A.2d)}$$

Applying simple mathematical manipulations, all Y-parameters can be rewritten in the form of equation (3.7) where the subscript 'int' is omitted for simplicity.

A.2 Derivation of Intrinsic Parameters:

Equations (A.2a) through (A.2d) form eight equations into eight unknowns; each equation can be split into real and imaginary equations. Therefore, these equations can be solved for the intrinsic parameters. The real and imaginary parts of all Y-parameters are known after de-embedding them from the measured S-parameters. Since the real and imaginary parts of y_{11}, y_{12}, and y_{22} are needed in the following derivation, we can write them separately as:

$$\mathrm{Re}(y_{11}) = \frac{\omega^2 R_i C_{gs}^2}{|D_1|^2} + \frac{\omega^2 R_{gd} C_{gd}^2}{|D_2|^2} \quad \text{(A.3a)}$$

$$\mathrm{Im}(y_{11}) = \omega\left(\frac{C_{gs}}{|D_1|^2} + \frac{C_{gd}}{|D_2|^2}\right) \quad \text{(A.3b)}$$

$$\mathrm{Re}(y_{12}) = -\frac{\omega^2 R_{gd} C_{gd}^2}{|D_2|^2} \quad \text{(A.3c)}$$

$$\mathrm{Im}(y_{12}) = -\omega \frac{C_{gd}}{|D_2|^2} \tag{A.3d}$$

$$\mathrm{Re}(y_{22}) = g_{ds} + \frac{\omega^2 R_{gd} C_{gd}^2}{|D_2|^2} \tag{A.3e}$$

$$\mathrm{Im}(y_{22}) = \omega \left(C_{ds} + \frac{C_{gd}}{|D_2|^2} \right) \tag{A.3f}$$

where

$$D_1 = 1 + j\omega R_i C_{gs}$$

$$D_2 = 1 + j\omega R_{gd} C_{gd}$$

Adding equation (A.3b) to equation (A.3d) reveals the following:

$$\mathrm{Im}(y_{11}) + \mathrm{Im}(y_{12}) = \frac{\omega C_{gs}}{|D_1|^2} \tag{A.4}$$

On the other hand, adding equation (A.3a) to equation (A.3c) leads to the following:

$$\mathrm{Re}(y_{11}) + \mathrm{Re}(y_{12}) = \frac{\omega^2 R_i C_{gs}^2}{|D_1|^2} \tag{A.5}$$

Dividing equation (A.5) by equation (A.4) eliminates D_1:

$$\omega R_i C_{gs} = \frac{\mathrm{Re}(y_{11}) + \mathrm{Re}(y_{12})}{\mathrm{Im}(y_{11}) + \mathrm{Im}(y_{12})} \tag{A.6}$$

The right hand side of equation (A.6) can be assumed to be equal to a variable d_1; thus equation (A.6) can be rewritten as:

$$\omega R_i C_{gs} = d_1 \tag{A.7}$$

where

$$d_1 = \frac{Re(y_{11}) + Re(y_{12})}{Im(y_{11}) + Im(y_{12})} \tag{A.8}$$

Also, D_1 can be written in terms of d_1:

$$D_1 = 1 + jd_1 \tag{A.9}$$

Substituting D_1 from equation (A.9) into equation (A.4), C_{gs} can be evaluated:

$$C_{gs} = \frac{\left(1 + d_1^2\right)}{\omega}\left(Im(y_{11}) + Im(y_{12})\right) \tag{A.10}$$

C_{gs} can be substituted in equation (A.7) to get R_i:

$$R_i = \frac{d_1}{\left(1 + d_1^2\right)\left(Im(y_{11}) + Im(y_{12})\right)} \tag{A.11}$$

C_{gd} and R_{gd} can be calculated in a similar manner. Divide equation (A.3c) by equation (A.3d) to remove D_2:

$$\omega R_{gd} C_{gd} = d_2 \tag{A.12}$$

where

$$d_2 = \frac{Re(y_{12})}{Im(y_{12})} \tag{A.13}$$

D_2 can be expressed in terms of d_2 as:

$$D_2 = 1 + jd_2 \tag{A.14}$$

Substitute D_2 into equation (A.3d) to estimate C_{gd}:

$$C_{gd} = -\frac{\mathrm{Im}(y_{12})}{\omega}\left(1 + d_2^2\right) \tag{A.15}$$

Substitute C_{gd} into equation (A.12) and rearrange to get R_{gd}:

$$R_{gd} = -\frac{d_2}{\left(1 + d_2^2\right)\mathrm{Im}(y_{12})} \tag{A.16}$$

The complex transconductance $G = g_m e^{-j\omega\tau}$ can be evaluated from the complex parameters y_{21} and y_{12}. The second term of y_{21} in equation (A.2b) can be removed by subtracting equation (A.2c) from (A.2b):

$$y_{21} - y_{12} = \frac{G}{1 + jd_1} \tag{A.17}$$

G can be extracted from equation (A.17):

$$G = (y_{21} - y_{12})(1 + jd_1) \tag{A.18}$$

The magnitude and phase of G represent g_m and $(-\omega\tau)$, respectively:

$$g_m = |G| = |(y_{21} - y_{12})|(1 + d_1^2) \tag{A.19}$$

$$\tau = -\frac{1}{\omega}\angle(G) \tag{A.20}$$

The last two parameters g_{ds} and C_{ds} can be calculated using equations (A.3c) through (A.3f). Adding equation (A.3c) to equation (A.3e) results in g_{ds}, while adding equation (A3.d) to equation (A.3f) and rearranging results in C_{ds}:

$$g_{ds} = \mathrm{Re}(y_{22}) + \mathrm{Re}(y_{12}) \tag{A.21}$$

$$C_{ds} = \frac{\mathrm{Im}(y_{22}) + \mathrm{Im}(y_{12})}{\omega} \tag{A.22}$$

In summary, equations (A.10), (A.11), (A.15), (A.16), (A.19), (A.20), (A.21), and (A.22) constitute the solution set of the intrinsic parameters at single-frequency measurements.

Appendix B
Impedance (Admittance) Curve Fitting

The curve fitting has been used in many places throughout our dissertation to fit an impedance (or admittance) branch to its data. We used frequency-weighted curve fitting in Lin's method as well as our novel technique. We also used linear curve fitting to extract some extrinsic parasitic elements from cold measurements. This appendix analyzes the different curve fitting procedures.

B.1 Curve Fitting of a Series RLC Impedance:

A series RLC impedance branch has to fit the measured impedance data. The error value at each frequency point 'i' is the discrepancy between the measured and the analytical impedance:

$$\varepsilon_i = W_i \left[Z_i - \left(R + j\left[\omega_i L - \frac{1}{\omega_i C} \right] \right) \right] \quad \text{(B.1)}$$

where W_i is a frequency dependent weighting factor and Z_i is the measured impedance. W_i is chosen in order to enhance the high frequency data, which is less noisy, and to make the curve fitting analysis much easier by converting the error function into a polynomial of ω_i. The weighting factor can be proposed as:

$$W_i = \omega_i C \quad \text{(B.2)}$$

Substituting W_i from (B.2) into (B.1) leads to the following:

$$\varepsilon_i = \left[\omega_i Z_i C - \omega_i RC - j\left(\omega_i^2 LC - 1 \right) \right] \quad \text{(B.3)}$$

The angular frequency ω_i and the impedance Z_i can be normalized to bring all values to the same order of magnitudes, which in turn avoids ill-conditioned matrix to be solved later on. The normalizing factor of ω_i is ω_o while that of Z_i is the characteristic impedance Z_o. The normalized quantities are:

$$\omega_i^{'} = \frac{\omega_i}{\omega_o} \quad \text{(B.4a)}$$

$$z_i = \frac{Z_i}{Z_o} = z_i^r + jz_i^i \quad \text{(B.4b)}$$

The normalizing factor ω_o is usually equal to the maximum angular frequency ω_{max}. Z_o is usually equal to 50Ω for most commercial measuring systems. Substitute the normalized quantities of (B.4) into (B.3) and rearrange the equation to reveal the following:

$$\varepsilon_i = \left(\omega_i^{'} z_i^r x_1 - \omega_i^{'} x_2\right) + j\left(\omega_i^{'} z_i^i x_1 - \omega_i^{'2} x_3 + 1\right) \quad \text{(B.5)}$$

where x_1, x_2, and x_3 are new variables which replace the old variables R, L and C according to the relationships:

$$x_1 = \omega_o Z_o C \quad \text{(B.6a)}$$

$$x_2 = \omega_o RC \quad \text{(B.6b)}$$

$$x_3 = \omega_o^2 LC \quad \text{(B.6c)}$$

The l_2-norm of the error function at all frequency points can be estimated as the sum of square absolute values of equation (B.5):

$$e = \sum_{i=1}^{N} \left|\varepsilon_i\right|^2 = \sum_{i=1}^{N} \left[\left(\omega_i^{'} z_i^r x_1 - \omega_i^{'} x_2\right)^2 + \left(\omega_i^{'} z_i^i x_1 - \omega_i^{'2} x_3 + 1\right)^2\right] \quad \text{(B.7)}$$

where N is the number of frequency points. In order to calculate the minimizer of the error function of (B.7), the function must be differentiated with respect to each variable x_1, x_2, and x_3; the differentiated equations are equated with zero; and then this set of equations is solved for the minimizer.

$$\frac{\partial e}{\partial x_1} = 0 \Rightarrow \sum_{i=1}^{N}\left[\left(\left(\omega_i' z_i^r\right)^2 + \left(\omega_i' z_i^i\right)^2\right)x_1 - \omega_i'^2 z_i^r x_2 - \omega_i'^3 z_i^i x_3 + \omega_i' z_i^i\right] = 0 \tag{B.8a}$$

$$\frac{\partial e}{\partial x_2} = 0 \Rightarrow \sum_{i=1}^{N}\left[\omega_i'^2 z_i^r x_1 - \omega_i'^2 x_2\right] = 0 \tag{B.8b}$$

$$\frac{\partial e}{\partial x_3} = 0 \Rightarrow \sum_{i=1}^{N}\left[\omega_i'^3 z_i^i x_1 - \omega_i'^4 x_3 + \omega_i'^2\right] = 0 \tag{B.8c}$$

The linear equations (B.8a) through (B.8c) can be written in the following matrix form:

$$\begin{bmatrix} \sum_{i=1}^{N}\left(\omega_i'^2 \left|z_i\right|^2\right) & -\sum_{i=1}^{N}\left(\omega_i'^2 z_i^r\right) & -\sum_{i=1}^{N}\left(\omega_i'^3 z_i^i\right) \\ \sum_{i=1}^{N}\left(\omega_i'^2 z_i^r\right) & -\sum_{i=1}^{N}\omega_i'^2 & 0 \\ \sum_{i=1}^{N}\left(\omega_i'^3 z_i^i\right) & 0 & -\sum_{i=1}^{N}\omega_i'^4 \end{bmatrix} \begin{bmatrix} x_1 \\ x_2 \\ x_3 \end{bmatrix} = \begin{bmatrix} -\sum_{i=1}^{N}\left(\omega_i' z_i^i\right) \\ 0 \\ -\sum_{i=1}^{N}\omega_i'^2 \end{bmatrix} \tag{B.9}$$

The linear set of equations in (B.9) can be easily solved for x_1, x_2, and x_3 at which the minimum value of the error function occurs. Knowing the values of x_1, x_2, and x_3, the impedance branch elements can be calculated from (B.6):

$$R = \frac{x_2}{x_1} Z_o \tag{B.10a}$$

$$L = \frac{x_3}{x_1}\frac{Z_o}{\omega_o} \tag{B.10b}$$

$$C = \frac{x_1}{\omega_o Z_o} \tag{B.10c}$$

B.2 Curve Fitting of a Series RC Admittance:

A series RC branch admittance, such as R_i and C_{gs} in the MESFET model, should fit the measured data. This fit procedure is used in our novel technique to estimate R_i. The procedure is very similar to the fit procedure aforementioned in the previous section. Again, we start with the error function at a frequency point 'i':

$$\varepsilon_i = W_i \left(y_i - \frac{1}{R + \frac{1}{j\omega_i C}} \right) \quad \text{(B.11)}$$

where $y_i = y_i^r + jy_i^i$ is the measured admittance. The weighting factor is equal to the branch impedance:

$$W_i = R + \frac{1}{j\omega_i C} \quad \text{(B.12)}$$

Substituting W_i from equation (B.12) into equation (B.11) and rearranging the equation for the real and imaginary parts results in the following equation:

$$\varepsilon_i = \left(Ry_i^r + \frac{y_i^i}{\omega_i C} - 1 \right) + j\left(Ry_i^i - \frac{y_i^r}{\omega_i C} \right) \quad \text{(B.13)}$$

The total error function can be written as:

$$e = \sum_{i=1}^{N} |\varepsilon_i|^2 = \sum_{i=1}^{N} \left(\left(Ry_i^r + \frac{y_i^i}{\omega_i} x - 1 \right)^2 + \left(Ry_i^i - \frac{y_i^r}{\omega_i} x \right)^2 \right) \quad \text{(B.14)}$$

where

$$x = \frac{1}{C} \tag{B.15}$$

The two variables of the error function are R and x. Differentiating the error function with respect to R and equating the differential function with zero leads to the value of R:

$$R = \frac{\sum_{i=1}^{N} y_i^r}{\sum_{i=1}^{N} |y_i|^2} \tag{B.16}$$

On the other hand, Differentiating the error function with respect to x and equating the differential function with zero leads to the value of x. Then, C is just the reciprocal of x:

$$C = \frac{\sum_{i=1}^{N} \left(\frac{|y_i|^2}{\omega_i^2} \right)}{\sum_{i=1}^{N} \left(\frac{y_i^i}{\omega_i} \right)} \tag{B.17}$$

B.3 Curve Fitting of a Parallel GC Impedance:

A parallel GC branch impedance should fit the measured data. The explained procedure is used to estimate g_{ds} in our proposed technique. The error function at frequency 'i' is:

$$\varepsilon_i = W_i \left(Z_i - \frac{1}{G + j\omega_i C} \right) \tag{B.18}$$

where

$$W_i = G + j\omega_i C \tag{B.19}$$

Similar to the previous sections, the error function can be calculated as:

$$e = \sum_{i=1}^{N} |\varepsilon_i|^2 = \sum_{i=1}^{N} \left(\left(Z_i^r G - \omega_i Z_i^i C - 1 \right)^2 + \left(Z_i^i G + \omega_i Z_i^r C \right)^2 \right) \quad \text{(B.20)}$$

where

$$Z_i = Z_i^r + jZ_i^i$$

G and C can be evaluated from the differentiation of the error function with respect to G and C, respectively:

$$G = \frac{\sum_{i=1}^{N} Z_i^r}{\sum_{i=1}^{N} |Z_i|^2} \quad \text{(B.21)}$$

$$C = -\frac{\sum_{i=1}^{N} \left(\omega_i Z_i^i \right)}{\sum_{i=1}^{N} \left(\omega_i^2 |Z_i|^2 \right)} \quad \text{(B.22)}$$

B.4 Curve Fitting of the Complex Transconductance:

The discussion of curve fitting of the complex transconductance is intended for the calculation of the transit time τ. The transconductance can be calculated in terms of the measured Y-parameters as shown in equation (A.18) and rewritten here for convenience:

$$G = g_m e^{-j\omega\tau} = (y_{21} - y_{12})(1 + jd_1) \quad \text{(B.23)}$$

where

$$d_1 = \frac{\mathrm{Re}(y_{11}) + \mathrm{Re}(y_{12})}{\mathrm{Im}(y_{11}) + \mathrm{Im}(y_{12})} \quad \text{(B.24)}$$

Since the magnitude of G is independent on its phase, the error function for the phase, at frequency ‘i’, can be stated as:

$$\varepsilon_{\tau i} = W_i\left(\angle\left((y_{21} - y_{12})(1 + jd_1)\right) + \omega_i \tau\right) \tag{B.25}$$

W_i can be any factor. However, our study showed that the best factor, which is documented by Lin et al. [28], leading to the closest value of τ is:

$$W_i = \frac{1}{\sqrt{\omega_i}} \tag{B.26}$$

The total error function can be written as:

$$e = \sum_{i=1}^{N} \left|\varepsilon_{\tau i}\right|^2 = \sum_{i=1}^{N} \left(\frac{1}{\omega_i} \left(\angle\left((y_{21} - y_{12})(1 + jd_1)\right) + \omega_i \tau\right)^2 \right) \tag{B.27}$$

Differentiating equation (B.27) with respect to τ and equating the differential function with zero reveals the value of τ:

$$\tau = -\frac{\sum_{i=1}^{N} \angle\left((y_{21} - y_{12})(1 + jd_1)\right)}{\sum_{i=1}^{N} \omega_i} \tag{B.28}$$

B.5 Linear Curve Fitting of an Inductive Impedance:

The estimation of the L_s and L_d from cold measurements requires linear curve fitting of the impedance of an inductance L to the measured data. The measured data here is the imaginary part of the impedance. The error function at frequency 'i' is:

$$\varepsilon_i = Z_i^i - \omega_i L \tag{B.29}$$

The total error function can be expressed as:

$$e = \sum_{i=1}^{N} |\varepsilon_i|^2 = \sum_{i=1}^{N} \left(Z_i^i - \omega_i L\right)^2 \qquad \text{(B.30)}$$

Solving for the root of the differential error function with respect to L results in the following value of L:

$$L = \frac{\sum_{i=1}^{N} \left(Z_i^i \omega_i\right)}{\sum_{i=1}^{N} \omega_i^2} \qquad \text{(B.31)}$$

Appendix C

Z-Parameters of the Transmission Line Under the Gate

The Intrinsic model of MESFET devices for cold measurements is modeled as a distributed uniform RC transmission line, which is shown in Figure 3.6. The Z-parameters of this transmission line has been used in equation (3.30). This appendix is concerned with the derivation of these Z-parameters. The short-cut of this derivation is to relate Z-parameters of a transmission line with the conventional excitement to a transmission line with the typical MESFET excitement. The Z-parameters of a conventional excited transmission line can be computed easily. Figure C.1 shows the RC transmission line under two excitement modes: conventional excitement and typical MESFET excitement.

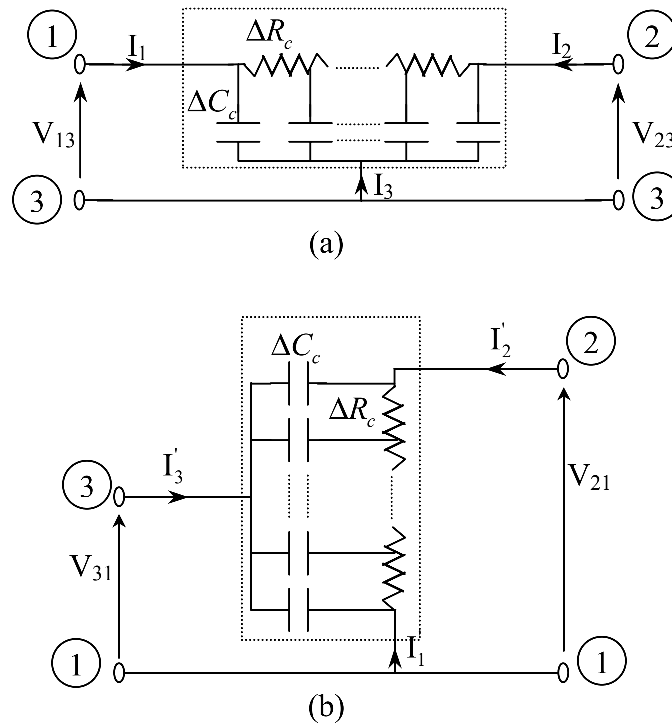

Figure C.1 The RC transmission line under different excitation topologies: (a) conventional excitation (b) typical excitation in a MESFET model.

The transmission line, enclosed by the dotted rectangle, can be regarded as a 2-port network. There are three terminals, labeled with circles, for the 2-port network in which one of them is common. The applied terminal voltages are assumed to be the same so that the terminal currents are equal,

$$I_1^{'} = I_1 \tag{C.1a}$$

$$I_2^{'} = I_2 \tag{C.1b}$$

$$I_3^{'} = I_3 \tag{C.1c}$$

The 2-port network equations can be written in terms of Z-parameters for Figure C.1(a) as follows:

$$V_{13} = Z_{11}I_1 + Z_{12}I_2 \tag{C.2a}$$

$$V_{23} = Z_{21}I_1 + Z_{22}I_2 \tag{C.2b}$$

On the other hand, the Z-parameters of the 2-port network of Figure C.1(b) can be written as:

$$V_{31} = Z_{11}^{'}I_3^{'} + Z_{12}^{'}I_2^{'} \tag{C.3a}$$

$$V_{21} = Z_{21}^{'}I_3^{'} + Z_{22}^{'}I_2^{'} \tag{C.3b}$$

where the 'prime' superscript is added to the Z-parameters to distinguish them from the Z-parameters of equations (C.2). The $Z^{'}$-parameters can be expressed in terms of Z-parameters. The $Z_{11}^{'}$ can be calculated from equation (C.3a), using equations (C.1b) and (C.1c), as:

$$Z_{11}^{'} = \left.\frac{V_{31}}{I_3^{'}}\right|_{I_2^{'}=0} = \left.\frac{-V_{13}}{I_3}\right|_{I_2=0} \tag{C.4}$$

I_3 is correlated to I_1 and I_2 as inferred from Figure C.1(a):

$$I_3 = -(I_1 + I_2) \tag{C.5}$$

Substituting I_3 from equation (C.5) into equation (C.4) while I_2=0, reveals the following:

$$Z'_{11} = \left.\frac{V_{13}}{I_1}\right|_{I_2=0} \tag{C.6}$$

Equation (C.6) defines the same value of Z_{11} as can be readily noticed from equation (C.2a);

$$Z'_{11} = Z_{11} \tag{C.7}$$

In the same way, all other Z'-parameters can be computed:

$$Z'_{12} = \left.\frac{V_{31}}{I'_2}\right|_{I'_3=0} = \left.\frac{-V_{13}}{I_2}\right|_{I_3=0} = \left.\frac{-V_{13}}{I_2}\right|_{I_1+I_2=0} \tag{C.8}$$

Substituting for V_{13} from equation (C.2a) into (C.8), results in the following:

$$Z'_{12} = \left.\frac{-Z_{11}I_1 - Z_{12}I_2}{I_2}\right|_{I_2=-I_1} = Z_{11} - Z_{12} \tag{C.9}$$

Z'_{21} can be calculated in the same way:

$$Z'_{21} = \left.\frac{V_{21}}{I'_3}\right|_{I'_2=0} = \left.\frac{V_{23} - V_{13}}{I_3}\right|_{I_2=0} = \frac{Z_{21}I_1 - Z_{11}I_1}{-I_1} = Z_{11} - Z_{21} \tag{C.10}$$

and so Z'_{22},

$$Z'_{22} = \left.\frac{V_{21}}{I'_2}\right|_{I'_3=0} = \left.\frac{V_{23} - V_{13}}{I_2}\right|_{I_2=-I_1} = \left.\frac{(Z_{21} - Z_{11})I_1 + (Z_{22} - Z_{12})I_2}{I_2}\right|_{I_2=-I_1} = Z_{11} - Z_{12} - Z_{21} + Z_{22} \tag{C.11}$$

Moreover, Z-parameters of a transmission line can be easily calculated. Figure C.2 illustrates a simplified representation of a uniform transmission line with characteristic impedance Z_o and propagation constant γ. The terminal voltages and currents are also shown.

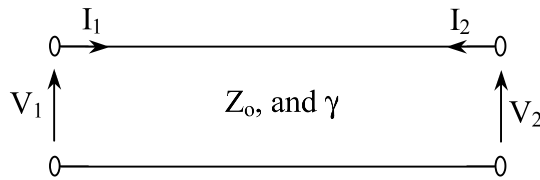

Figure C.2 A simplified representation of a uniform transmission line.

Z_{11} is simply equal to the input impedance seen at port1,

$$Z_{11} = \left.\frac{V_1}{I_1}\right|_{I_2=0} = Z_o \frac{Z_L + Z_o \tanh(\gamma L)}{Z_L \tanh(\gamma L) + Z_o} \tag{C.12}$$

where Z_L is the load impedance which is equal to infinity if I_2=0; thus equation (C.12) reduces to:

$$Z_{11} = \frac{Z_o}{\tanh(\gamma L)} \tag{C.13}$$

Z_{21} can also be computed easily,

$$Z_{21} = \left.\frac{V_2}{I_1}\right|_{I_2=0} \tag{C.14}$$

The voltage and current can be expressed as functions of the position for a transmission line as:

$$V(x) = V(0)(e^{-\gamma x} + \Gamma e^{\gamma x}) \tag{C.15}$$

$$I(x) = \frac{V(0)}{Z_o}(e^{-\gamma x} - \Gamma e^{\gamma x}) \tag{C.16}$$

where x is the length from the left terminal of the transmission line and Γ is the reflection coefficient at x=0. Γ can be calculated from the boundary condition at x=L where I(L)=0:

$$\frac{V(0)}{Z_o}(e^{-\gamma x} - \Gamma e^{\gamma x}) = 0 \tag{C.17}$$

Equation (C.17) implies that the term between the brackets must be equal to zero, consequently Γ can be estimated as:

$$\Gamma = e^{-2\gamma L} \tag{C.18}$$

Substituting into equation (C.14) with the voltage and the current from equations (C.15) and (C.16) knowing the value of Γ, computes the following value for Z_{21}:

$$Z_{21} = \left.\frac{V(L)}{I(0)}\right|_{I_2=0} = \frac{2Z_o e^{-\gamma L}}{1 - e^{-2\gamma L}} = \frac{Z_o}{\sinh(\gamma L)} \tag{C.19}$$

Since the transmission line is reciprocal and symmetric, the other Z-parameters must be interrelated as:

$$Z_{22} = Z_{11} = \frac{Z_o}{\tanh(\gamma L)} \tag{C.20}$$

$$Z_{12} = Z_{21} = \frac{Z_o}{\sinh(\gamma L)} \tag{C.21}$$

The Z'-parameters of the RC transmission line under the gate can then be estimated from equations (C.7), (C.9), (C.10), and (C.11) using the values of Z-parameters from equations (C.13), (C.19), (C.20), and (C.21). The characteristic impedance of the RC transmission line reads:

$$Z_o = \sqrt{\frac{R_c / L}{j\omega C_c / L}} = \frac{\sqrt{j\omega R_c C_c}}{j\omega C_c} = \frac{\gamma L}{j\omega C_c} \tag{C.22}$$

The Z'-parameters can be concluded as:

$$Z'_{11} = \frac{\gamma L}{j\omega C_c \tanh(\gamma L)} \tag{C.23a}$$

$$Z'_{12} = \frac{Z_o}{\tanh(\gamma L)} - \frac{Z_o}{\sinh(\gamma L)} = \frac{\gamma L(\cosh(\gamma L) - 1)}{j\omega C_c \sinh(\gamma L)} \tag{C.23b}$$

$$Z'_{21} = Z'_{12} = \frac{\gamma L(\cosh(\gamma L) - 1)}{j\omega C_c \sinh(\gamma L)} \tag{C.23c}$$

$$Z'_{22} = 2\frac{\gamma L(\cosh(\gamma L) - 1)}{j\omega C_c \sinh(\gamma L)} \tag{C.23d}$$

References

[1] S.A. Mass, Nonlinear Microwave Circuits, Norword, MA: Artech House, 1988.

[2] J. M. Golio, Microwave MESFETs & HEMTs, Norwood, MA: Artech House, 1991.

[3] S.M. Sze, Semiconductor Devices Physics and Technology, New York: John Wiley & Sons, 1985.

[4] Robert Soares, GaAs MESFET Circuit Design, Norword, MA: Artech House, 1988.

[5] James V. Dilorenzo and Deen D. Khandelwal, GaAs FET Principles and Technology, Dedham, Massachusetts: Artech House, Inc., 1982.

[6] G. Dambrine et al., “A New Method for Determining the FET Small-Signal Equivalent Circuit,” IEEE Transactions on Microwave Theory and Techniques, Vol. 36, No. 7, pp. 1151-1159, July 1988.

[7] M. Berroth and R. Bosch, “High-Frequency Equivalent Circuit of GaAs FET’s for Large-Signal Applications,” IEEE Transactions on Microwave Theory and Techniques, Vol. 39, No. 2, pp. 224-229, Feb. 1991.

[8] Hiroshi Kondoh, “An Accurate FET Modelling from Measured S-Parameters,” IEEE MTT-S International Microwave Symposium Digest, pp. 377-380, June 1986.

[9] R.A. Minasian, “Simplified GaAs M.E.S.F.E.T. Model to 10 GHz,” Electronics Letters, Vol. 13, No. 18, pp. 549-551, 1st September 1977.

[10] H. Fukui, “Determination of the Basic Device Parameters of a GaAs MESFET,” The Bell System Technical Journal, Vol. 58, No. 3, pp. 771-795, March 1979.

[11] T. Chen and M. Kumar, “Novel GaAs FET Modeling Technique for MMICs,” IEEE GaAs IC Symposium Digest, pp. 49-52, 1988.

[12] Kang W. Lee et al., “Source, Drain, and Gate Series Resistances and Electron Saturation Velocity in Ion-Implanted GaAs FET’s,” IEEE Transactions on Electron Devices, Vol. ED-32, No. 5, pp. 987-992, May 1985.

[13] Long Yang and Stephen I. Long, “New Method to Measure the Source and Drain Resistance of the GaAs MESFET,” IEEE Electron Device Letters, Vol. EDL-7, No. 2, pp. 75-77, February 1986.

[14] Kurt Lehovec, “Determination of Impurity and Mobility Distributions in Epitaxial Semiconducting Films on Insulating Substrate by C-V and Q-V Analysis,” Applied Physics Letters, Vol. 25, No. 5, pp. 279- 281, September 1974.

[15] F. Diamond and M. Laviron, “Measurements of the Extrinsic Series Elements of Microwave MESFET under Zero Current Conditions,” 12th European Microwave Conference Proceedings, pp. 451-456, September 1982.

[16] W. R. Curtice and R. L. Camisa, “Self-Consistent GaAs FET Models for Amplifier Design and Device Diagnostics,” IEEE Transactions on Microwave Theory and Techniques, Vol. MTT-32, No. 12, pp. 1573-1578, Dec. 1984.

[17] Rimantas L. Vaitkus, “Uncertainty in the Values of GaAs MESFET Equivalent Circuit Elements Extracted from Measured Two-Port Scattering Parameters,” IEEE Conference Proceedings on High Speed Semiconductor Devices Circuits, Cornell Univ., Ithaca, NY, pp. 301-308, 1983.

[18] Andrew D. Patterson et al., “A Systematic Optimization Strategy For Microwave Device Modelling,” IEEE Transactions on Microwave Theory and Techniques, Vol. 41, No. 3, pp. 395-405, March 1993.

[19] C. Van Niekerk and P. Meyer, “A New Approach for the Extraction of an FET Equivalent Circuit from Measured S Parameters,” Microwave and Optical Technology Letters, Vol. 11, No. 5, pp. 281-284, April 5, 1996.

[20] Cornell van Niekerk and Petrie Meyer, “Performance and Limitations of Decomposition-Based Parameter-Extraction Procedures for FET Small-Signal Models,” IEEE Transactions on Microwave Theory and Techniques, Vol. 46, No. 11, pp. 1620-1627, Nov. 1998.

[21] M. S. Leong et al., “A Hybrid Gauss-Newton-Simulated Annealing Optimizer for Extraction of MESFET Equivalent Circuit Elements,” Microwave and Optical Technology Letters, Vol. 6, No. 8, pp. 461-466, June 20, 1993.

[22] Man-Kuan Vai et al., “Modeling of Microwave Semiconductor Devices Using Simulated Annealing Optimiuzation,” IEEE Transactions on Electron Devices, Vol. 36, No. 4, pp. 761-762, April 1989.

[23] Hardy Sledzik and Ingo Wolff, “A New Approach to Nonlinear Modelling and Simulation of MESFETs and MODFETs,” 20th European Microwave Conference Proceedings, Budapist, Hungary, pp. 784-789, September 1990.

[24] G. Kompa and M. Schlechtweg, “Generalized Modeling of GaAs MESFETS and MODFETS Based on Highly Accurate Broadband Measurements,” 19th European Microwave Conference Proceedings, pp. 179-186, September 1989.

[25] G. Kompa and F. Lin, “New Algorithm Approach for Consistent Model Parameter Extraction of GaAs MESFET Equivalent Circuits,” Proceedings of 5th Conference on Microwave and Optronics (MIOP ’90), pp. 257-262, 1990.

[26] G. Kompa and F. Lin, "FET Modelling Using an Analytical Extraction Method Based on Broadband S-parameter Measurement," 20th European Microwave Conference Proceedings, Budapist, Hungary, pp. 778-783, September 1990.

[27] G. Kompa and M. Novotny, "Highly Consistent FET Model Parameter Extraction Based on Broadband S-Parameter Measurements," IEEE MTT-S International Microwave Symposium Digest, (CH3141), pp. 293-296, 1992.

[28] Fujiang Lin and Günter Kompa, "FET Model Parameter Extarction Based on Optimization With Multiplane Data-Fitting and Bidirectional Search-A new concept," IEEE Transactions on Microwave Theory and Techniques, Vol. 42, No. 7, pp. 1114-1121, July 1994.

[29] K. Shirakawa et al., "An Approach to Determining an Equivalent Circuit for HEMT's," IEEE Transactions on Microwave Theory and Techniques, Vol. 43, No. 3, pp. 499-503, March 1995.

[30] B. Ooi et al., "A Novel Approach for Determining the GaAs MESFET Small-Signal Equivalent-Circuit Elements," IEEE Transactions on Microwave Theory and Techniques, Vol. 45, No. 12, pp. 2084-2088, Dec. 1997.

[31] Alberto Di Martino et al., "A New Algorithm to Extract the Nonlinear Model of MESFETs and HEMTs," Microwave and Optical Technology Letters, Vol. 20, No. 5, pp. 297- 302, March 5, 1999.

[32] D.M. Pozar, Microwave Engineering, USA: Addison-Wesley Publishing Company, 1990.

[33] W. R. Curtice and M. Ettenberg, "A Nonlinear GaAs FET Model for Use in the Design of Output Circuits for Power Amplifiers," IEEE Transactions on Microwave Theory and Techniques, Vol. MTT-33, No. 12, pp. 1383-1393, Dec. 1985.

[34] L.E. Scales, Introduction to Non-Linear Optimization, New York: Springer-Verlag New York Inc., 1985.

[35] HP8510C Network Analyzer, On-Site Service Manual, Santa Rosa, CA: Hewlett-Packard Company, 1991.

[36] Vahid Sotoudeh and Mark Roose, "Statistical Analysis of Simulated Automatic Network Analyzer Measurements," IEEE MTT-S International Microwave Symposium Digest, Vol. 1, pp. 269-272, June 1987.

[37] Andrew Grace, Optimization Toolbox User's Guide for Use with MATLAB, Natick, Mass: The Math Works, Inc., December 1992.

[38] R. Anholt, Electrical and Thermal Characterization of MESFETs, HEMTs, and HBTs, Norwood, MA: Artech House, 1995.

VITA

Yaser A. Khalaf

Yaser A. Khalaf was born in Cairo, Egypt on March 3rd, 1968. He received his B.Sc. in Electrical Engineering from Cairo University in July 1991. In 1992-1993, He worked as a teaching assistant in Mathematics and Physics Department, Faculty of Engineering, Cairo University. He received his M.Sc. in Electrical Engineering from Cairo University in July 1995. In 1993-1996, he worked as a teaching assistant in Electrical Engineering Department, Faculty of Engineering, Zagazig University. In 1996, he was awarded an Egyptian Governmental scholarship for doctorate studies. Since August 1996, he has been working towards his Ph.D. degree in Electrical Engineering at Virginia Tech. During his Ph.D. program at Virginia Tech, he was awarded some teaching and research assistantship assignments.